University of California
Los Angeles

Vortex Models for Data Assimilation

A dissertation submitted in partial satisfaction
of the requirement for the degree
Doctor of Philosophy in Mechanical Engineering

by

Darwin Darakananda

2017

Abstract of the Dissertation

Vortex Models for Data Assimilation

by

Darwin Darakananda
Doctor of Philosophy in Mechanical Engineering
University of California, Los Angeles, 2017
Professor Jeff D. Eldredge, Chair

Inviscid vortex models have been used for decades to investigate unsteady aerodynamics. However, real-time use of these models has been hindered by the tradeoff between increasing a model's dynamical capability and reducing its dimensionality. In this work, we present two different solutions to this problem. First, we develop a hybrid model where vortex sheets represent shear layers that separate from the wing and point vortices represent the rolled-up cores of these shear layers and the other coherent vortices in the wake. Instead of rolling up, each vortex sheet feeds its circulation into a point vortex using a circulation transfer procedure we developed. This procedure eliminates the spurious force that manifests when transferring circulation between vortex elements. By tuning the rate at which the vortex sheets are siphoned into the point vortices, we can adjust the balance between the model's dimensionality and dynamical richness. This hybrid model can capture the development and subsequent shedding of the starting vortices in real time, and remain low-dimensional enough to simulate long time horizon events such as periodic bluff-body shedding. Our second solution augments a vortex

blob model with surface pressure measurements using the ensemble Kalman filter (EnKF). We adapt our circulation transfer procedure to aggressively aggregate the vortex blobs in order to prevent the dimension of the system from increasing indefinitely. The reduced number of blobs, along with the parallel nature of the EnKF, allow this solution to also run in real time. We find that not only does the data assimilation process compensate for the severe reduction in dimension, it also seems to fill in some missing physics from our inviscid model.

The disseration of Darwin Darakananda is approved.

Chris R. Anderson

Jason L. Speyer

Xiaolin Zhong

Jeff D. Eldredge, Committee Chair

University of California, Los Angeles

2017

Table of Contents

List of Figures

Acknowledgements

There are many people without whom this work would have been impossible. First and foremost, I would like to thank my advisor, Professor Jeff Eldredge. Without doubt, my decision to dive into the world of fluid dynamics was born from the two classes I took from you as an undergraduate. It was with your support that I was able to join SOFIA lab, and your guidance that helped me navigate the event horizon around the black hole of curiosity. I would also like to thank my committee members, Professor Xiaolin Zhong, Professor Chris Anderson, and Professor Jason Speyer for their time and valuable insights.

I cannot overstate the impact that my friends have made on my last five years. I would like to thank Kwitae Chong and Ethan Young for their kindness and openness. Our lunch-time discussions made the entire journey more enjoyable. I have to thank David Weisbart, who introduced me to the wonders and intricacies of mathematics and Megan Weisbart for always being such a gracious host and letting me camp out at their house whenever I called on David for technical support. These visits were such wonderful retreats for me during my most stressful times.

Of course, I must thank my family for their continued encouragement and love. Thank you all for being so understanding even as I worked through the holidays. I especially want to thank my grandparents. You encouraged and developed my childhood curiosity at the cost of many broken walls and furniture.

Last but not least, I must thank my best friend and fiancé, Angel Zhang. Your loving companionship and sharp intellect over the last four wonderful years gave me the support I needed to complete this endeavour. Without you, I could very well be pursuing a career as a sushi chef.

Vita

2012	B.S. in Mechanical Engineering, University of California, Los Angeles
2012	B.S. in Atmospheric and Oceanic Sciences, University of California, Los Angeles
2012	Teaching Assistant, Department of Mechanical and Aerospace Engineering, University of California, Los Angeles
2017	M.S. in Mechanical Engineering, University of California, Los Angeles
2012-2017	Graduate Student Researcher, Department of Mechanical and Aerospace Engineering, University of California, Los Angeles

Chapter 1

Introduction

Experiments in aerodynamics have demonstrated that there exists a whole host of unsteady and nonlinear phenomena that we can use to improve the agility and maneuverability of our aircraft. Dickinson and Götz [12] measured the forces on a two-dimensional model wing and found that the initial production of a leading edge vortex (LEV) can increase the lift by 80% over the steady-state value. The subsequent shedding of the LEV then results in a decrease in lift production. More recently, Taira et al. [55] performed high-fidelity simulations of a three-dimensional flat plate at a variety of aspect ratios. While the transport of spanwise vorticity affected the separation time of the LEV, they found that the time at which maximum lift occurs is relatively constant over different aspect ratios and angles of attack. These transient lift-enhancement mechanisms are instinctively used by insects. By producing and manipulating LEVs, insects are able to sustain lift at angles of attack that exceed the static stall angle. In fact, Ellington [15] demonstrated that the insects' ability to hover can *only* be explained by unsteady aerodynamic theory, since without the effects of added mass and vortex generation, earlier estimates of insect lift production by Weis-Fogh [60] and Jensen [25] were unable to offset the insects' weight.

A better understanding of unsteady aerodynamics is not only useful for enhancing flight systems with flapping wings, but can also lead to improved performance of fixed-wing aircraft. Amitay and Glezer [3] first showed that the lift of a fully stalled airfoil can be temporarily enhanced by applying a pulse of actuation at the leading edge. Williams et al. [62] then explored the effect of applying multiple pulses and modeled the response of

these pulses as a convolution of shifted, single-pulse responses. Controllers based on this model perform well for low-frequency pulse trains, but Kerstens et al. [29] found that when the frequency of the pulses is on the order of the inverse convective time, the accuracy of the predicted lift responses drops. Unfortunately, the frequency that results in the most lift-enhancement and gust-suppression often lies in the latter range of pulse frequencies. The decreased accuracy in this range is due to the nonlinear interaction between the pulse responses, since the linear model requires that changes to the flow field be advected far enough downstream so as to have their effect decorrelated with the effect of the next pulse.

While we are able to recreate many of these flight enhancing effects in high-fidelity numerical simulations, we still need a better understanding of their key governing mechanisms before we can effectively control them. We need models of the full flow physics that are simple enough for us to understand, low-dimensional enough to be used for real-time flow control, yet dynamically rich enough to be useful. Vortex-based models were one of the first attempts at addressing this need. Unfortunately, these vortex models had to choose between dynamical richness and low-dimensionality, which limited their use in flow control applications. In this thesis, we introduce a new class of vortex models where the balance between dynamical richness and model dimension is adjustable. We also demonstrate how empirical surface pressure can be assimilated into these reduced-order vortex models to produce force responses with higher accuracy.

1.1 Reduced-Order Models

This work focuses on vortex-based models, which will be discussed in detail in Chapter 2, but to provide context, we first discuss reduced-order models in general. A reduced-order model can be characterized by what it considers to be a coherent structure, a spatial structure that persists in time. Modal analysis is a common framework for identifying coherent structures. Using techniques from linear algebra, the flow field or the operator that

evolves the flow field is linearly decomposed into separate *modes*. Then, a reduced-order model is constructed by using a subset of the modes.

One of the most commonly used decompositions is the Proper Orthogonal Decomposition (POD) [37]. When applied to data of the velocity field, POD produces the minimum number of orthogonal modes necessary to capture the distribution of kinetic energy in the flow field. An important property of POD is that the modes are ordered in decreasing energy levels given by their coefficients. We can reduce the dimensionality of the data by truncating the low energy modes while still retaining the highest energy structures in the flow. Unfortunately, Aubry et al. [6] found that low energy modes can often trigger large scale dynamics, so truncating them can lead to loss of important flow physics. This is related to the concept of controllability and observability in control theory. A highly controllable mode means a small change in the flow field has a large impact on the mode's coefficient. On the other hand, a highly observable mode means that a change to its coefficient leads to large changes in the flow field. In the case of POD, changes in the flow field are essentially absorbed by the higher energy modes, making the lower energy modes less controllable. However, since low energy modes can have large impacts on the overall flow field, they can be highly observable.

To address this weakness, Rowley [49] introduced the Balanced POD (BPOD) method. BPOD uses the impulse responses of the system and its adjoint system (which requires running the system backwards in time) to determine the controllability and observability of the system. Then, using a standard control systems technique called balanced truncation, BPOD finds the modes of the flow data where the most controllable modes are also the most observable modes. As these modes are ordered in decreasing levels of observability/controllability, we can safely truncate higher order modes without missing the most excitable flow structures. Since BPOD requires the impulse response of the adjoint system, it cannot process experimental data. This issue was resolved when Ma, Ahuja, and Rowley [38] introduced the Eigensystem Realization Algorithm (ERA), which produces the same

reduced-order model as BPOD without requiring the adjoint impulse response. POD and its variants are only a small part in a much larger space of modal analysis techniques. We refer the reader to a recent review by Taira et al. [54] for a more complete overview of modal analysis techniques.

As these modal analysis techniques arise from linear systems theory, the reduced-order models they generate are immediately compatible with a variety of tools from linear control theory. Of course, this also means that these models may have a difficult time capturing heavily nonlinear features of the flow. For example, Ahuja and Rowley [1] used BPOD to derive a reduced-order model of flow past a flat plate at high angles of attack. They were then able to use a linear quadratic (Kalman) filter in conjunction with the reduced-order model to estimate the velocity field from sensor measurements, which was then fed into a linear quadratic regulator (LQR) that controls an actuator at the trailing edge of the plate. Although such a flow usually undergoes periodic vortex shedding, there exists an unstable steady state. By linearizing the model about this unstable steady state, they were able to avoid the nonlinearity of vortex shedding. The LQR was then able to suppress vortex shedding indefinitely. However, this also means that the model is not adequate for investigating flows with strong vortex dynamics, such as those in the development of a LEV. So while the linearity of the model gave it direct access to the Kalman filter and the LQR, linearity is also what limits the model's applicability. There is active interest in extending modal analysis to nonlinear systems [24], but we will take an alternative route and explore vortex models.

Vortex models are another class of reduced-order models that define, unsurprisingly, the vortex as the coherent structure of interest. Instead of *identifying* important coherent structures, vortex models start off with the idea that vorticity is the "sinews and muscles of fluid motion" [32]. Vortex models reduce the dimensionality of the fluid dynamics by omitting certain physical processes, such as viscous diffusion, and representing regions of vorticity with simple computational elements, such as point vortices. Unlike models

derived from modal decomposition, vortex models retain the nonlinear nature of the flow physics. This makes them a natural choice for modeling highly separated, vortex dominated flows.

1.2 Data-Driven Vortex Models

Unlike models derived from modal decomposition, vortex models are not formulated in a way that is directly compatible with data assimilation techniques from control theory. Therefore, researchers have to either limit the dynamical richness of their vortex models, or develop new data assimilation procedures. In this section, we explore how three different types of data sources are incorporated into vortex models.

The most common type of data is Eulerian measurements, where field quantities over an entire spatial region is measured over time. An example of the fusion of Eulerian data with vortex models can be found in a recent work by Pitt Ford and Babinsky [45]. The authors investigated the development of the LEV and its effect on lift using snapshots of experimental flow field data. They introduced a new method that represented these snapshots as distributions of point vortices whose particle count, instantaneous positions, and strengths are attained from the experimental velocity field. The bound circulation of the airfoil is then adjusted to minimize the difference between the velocity field predicted by the model and that observed empirically. This makes it possible for them to decompose the vorticity field into contributions from the LEV, trailing edge vortex (TEV), and the bound circulation around the airfoil, and evaluate the influence each component has on the lift.

Another source of data is tracer particle trajectories, also known as Lagrangian data. An early method for assimilating this type of data into vortex models was explored by Kuznetsov, Ide, and Jones [33]. They used an extended Kalman filter (EKF) to estimate the positions of point vortices given the trajectories of tracer particles. In order to make

the model compatible with the EKF, the number of point vortices must be restricted to some constant and given to the filter. The measurements are generated from the same point vortex model with added white noise. They obtained promising results for moderate levels of noise and initial tracer particle positions that are far away from transport barriers in the flow.

For the purposes of aerodynamic flow control, the only practical source of data is measurements on the airfoil. Hemati, Eldredge, and Speyer [22] used force measurements to augment a vortex model developed by Wang and Eldredge [59], where the LEV and TEV are represented as point vortices with time-varying strength. The ability to change the strength of the point vortices allows the model to simulate the effects of releasing new vorticity from the wing (i.e. vorticity flux) without creating new vortex particles. Using optimal control theory, Hemati, Eldredge, and Speyer then determined the sequence of leading and trailing edge vorticity flux that would minimize the difference between the model-predicted and empirically-measured force. However, the Wang and Eldredge model did not have a built-in mechanism for modeling the formation of new vortex structures in the wake, which limited its use to short time intervals. In this work, we will build on both the Wang and Eldredge vortex model as well as the data assimilation procedure developed by Hemati, Eldredge, and Speyer.

1.3 Overview of this work

The primary contributions of this thesis are as follows:

- developed a procedure to transfer circulation between vortex elements in aerodynamic flows that preserves the instantaneous force response
- enhanced the model optimization procedure originally developed by Hemati, Eldredge, and Speyer to work with a real-time data source

- integrated an ensemble Kalman filter with a vortex blob model to form a real-time flow estimator

We start by reviewing the basic theories behind vortex modeling in Chapter 2. Then in Chapter 3, we develop the impulse-matching circulation transfer procedure and demonstrate it by integrating vortex sheets with point vortices of time-varying strength into a method that is able to capture the formation of coherent vortex structures while remaining computationally tractable for real-time control purposes. We show that by tuning the rate at which circulation is transferred from the vortex sheets to the point vortices, we can adjust the balance between the model's dimensionality and dynamical richness. In Chapter 4, we introduce two new methods of assimilating empirical data into vortex models. We start with an extension to the model optimization procedure developed by Hemati, Eldredge, and Speyer, enabling it to incrementally optimize a vortex model as new data arrives. Then, we show how we can use an ensemble Kalman filter to improve a vortex blob model using surface pressure data. Finally, in Chapter 5, we present our concluding remarks and outline future directions for research.

Chapter 2

Vortex Modeling of Aerodynamics

We are interested in the flow around a wing as it moves through a fluid. For the flow regimes in which we are interested, the wing can be treated as a two dimensional rigid body that is moving with velocity $\boldsymbol{u}_b$ through an incompressible fluid with uniform density ρ and kinematic viscosity ν. We will assume that the wing is the only solid body of relevance so that the fluid domain, $\mathcal{R}_f$, starts from the body surface, $\mathcal{S}_b$, and extends infinitely far. Under these conditions, the velocity of the fluid, $\boldsymbol{u}$, is related to its pressure, p, through the incompressible Navier-Stokes equations:

$$\frac{\partial \boldsymbol{u}}{\partial t} + \boldsymbol{u} \cdot \nabla \boldsymbol{u} = -\frac{1}{\rho} \nabla p + \nu \nabla^2 \boldsymbol{u}, \tag{2.1}$$

with a continuity constraint on the velocity field

$$\nabla \cdot \boldsymbol{u} = 0, \tag{2.2}$$

and the no-slip boundary condition on the surface of the body

$$\boldsymbol{u}(\boldsymbol{x}) = \boldsymbol{u}_b(\boldsymbol{x}) \quad : \quad \boldsymbol{x} \in \mathcal{S}_b. \tag{2.3}$$

While the continuity equation, Equation (2.2), is stated as a divergence-free condition on the velocity field, it is actually responsible for the tight coupling of the velocity and pressure fields. This tight coupling can be seen by taking the divergence of Equation (2.1) and

substituting in Equation (2.2), which gives us

$$\nabla^2 p = -\nabla \cdot (\boldsymbol{u} \cdot \nabla \boldsymbol{u}). \tag{2.4}$$

This pressure Poisson equation and the Navier-Stokes equations give us a way to co-evolve the velocity and pressure fields forward in time. However, this velocity-pressure formulation of the governing equations makes it difficult to decompose the flow field for model reduction. Local changes in the velocity field have a wide reaching effect due to the divergence-free condition, and local values of pressure require information about the entire velocity field. This means that even if we are only interested in *local* changes to the fluid velocities (e.g. to compute local changes to shear stresses on the body), we would have to first solve for the changes to the *global* flow field. Fortunately, the vorticity formulation of the Navier-Stokes equations provides a natural decomposition of the flow field. All vortex models stem from this vorticity-based decomposition of the flow field. In this chapter, we first review the role of vorticity and its dynamics. Then, we show how the vorticity transport equation and its viscous-splitting interpretation provide a systematic framework for constructing new vortex models. Finally, we review existing vortex models of aerodynamics and see how they fit into this framework.

2.1 Vorticity Formulation of Navier-Stokes

We start by defining vorticity,

$$\boldsymbol{\omega} := \nabla \times \boldsymbol{u}. \tag{2.5}$$

and its integral counterpart, circulation

$$\Gamma := \oint_{\mathcal{C}} \boldsymbol{u} \cdot \, \mathrm{d}\boldsymbol{l} = \int_{\mathcal{S}} \boldsymbol{\omega} \cdot \hat{\boldsymbol{n}} \, \mathrm{d}S. \tag{2.6}$$

We can recover the velocity field from the vorticity field by inverting Equation (2.5). For now, let us temporarily relax the no-slip boundary condition, so that the fluid velocity can be different from the solid velocity at their interface. This discontinuous jump in velocity across the solid-fluid interface can be represented as an infinitesimally thin sheet of vorticity called a *vortex sheet*, with the strength of the sheet at any point given by

$$\boldsymbol{\gamma} := \boldsymbol{u}(\boldsymbol{x}) - \boldsymbol{u}_b(\boldsymbol{x}) \quad : \quad \boldsymbol{x} \in \mathcal{S}_b. \tag{2.7}$$

Then the fluid velocity can be written in terms of the vorticity with

$$\begin{aligned}\boldsymbol{u}(\boldsymbol{\xi}) = &\frac{1}{2\pi}\int_{\mathcal{R}_f} \boldsymbol{\omega} \times \frac{\boldsymbol{\xi}-\boldsymbol{x}}{|\boldsymbol{\xi}-\boldsymbol{x}|^2}\,\mathrm{d}R + \frac{1}{2\pi}\int_{\mathcal{S}_b} \boldsymbol{\gamma} \times \frac{\boldsymbol{\xi}-\boldsymbol{x}}{|\boldsymbol{\xi}-\boldsymbol{x}|^2}\,\mathrm{d}S \\ &+ \frac{1}{2\pi}\int_{\mathcal{S}_b} (\hat{\boldsymbol{n}} \times \boldsymbol{u}_b) \times \frac{\boldsymbol{\xi}-\boldsymbol{x}}{|\boldsymbol{\xi}-\boldsymbol{x}|^2}\,\mathrm{d}S - \frac{1}{2\pi}\int_{\mathcal{S}_b} (\hat{\boldsymbol{n}} \cdot \boldsymbol{u}_b)\frac{\boldsymbol{\xi}-\boldsymbol{x}}{|\boldsymbol{\xi}-\boldsymbol{x}|^2}\,\mathrm{d}S.\end{aligned} \tag{2.8}$$

The first integral in Equation (2.8) is the standard Biot-Savart integral. It represents the relationship between the velocity field and the vorticity field in the absence of internal boundaries in the fluid. The last three integrals capture the displacement of the fluid that is caused by the translation and rotation of the body. Note that if the no-slip condition (Equation (2.3)) is enforced, then $\boldsymbol{\gamma}$ is zero.

We obtain the transport for vorticity by simply taking the curl of the Navier-Stokes equations, Equation (2.1), to find

$$\underbrace{\frac{\partial \boldsymbol{\omega}}{\partial t} + \boldsymbol{u}\cdot\nabla\boldsymbol{\omega}}_{\text{advection}} = \underbrace{\nu\nabla^2\boldsymbol{\omega}}_{\text{diffusion}}. \tag{2.9}$$

Note in the equation above that if a fluid initially has no vorticity, it is impossible to generate new vorticity in the fluid. This suggests that vorticity can only enter into the fluid through its boundaries, i.e. through the fluid-solid interface. Moreover, advection and viscous diffusion both affect vorticity at a finite rate. In fact, in an incompressible flow, vor-

ticity is the *only* fluid property that does not propagate instantaneously [36]. This means that vorticity is always a finite distance away from the solid body. This compact nature of vorticity naturally allows us to decompose the flow field into regions with vorticity and regions without vorticity.

The advection and diffusion terms in the vorticity transport equation can be thought of as two separate processes that occur in quick succession. This two-step *viscous-splitting* can be written as

1. inviscid convection step

$$\frac{\partial \boldsymbol{\omega}}{\partial t} + \boldsymbol{u} \cdot \nabla \boldsymbol{\omega} = 0 \tag{2.10}$$

   when vorticity moves with the fluid

2. diffusion step

$$\frac{\partial \boldsymbol{\omega}}{\partial t} = \nu \nabla^2 \boldsymbol{\omega} \tag{2.11}$$

   when vorticity simply diffuses.

As the time-step between these two processes go to zero, it can be shown that this alternating process converges to the original vorticity transport equation [39]. Now let us consider how the the two viscous-splitting steps interact with solid boundaries. In the first step, since we assume the flow to be inviscid, we cannot enforce the no-slip condition. However, even inviscid fluids cannot flow through solid boundaries, so at least the no-flow-through condition must be satisfied. Looking back at Equation (2.8), we see that since vorticity is constrained to move with the fluid through Equation (2.10), and the body motion is prescribed, the only term that is free to adjust is the vortex sheet on the body surface. So during the inviscid advection stage, γ is responsible for taking on whatever value it must to enforce no-flow-through. In the diffusion step, however, viscosity returns so we now have to enforce the no-slip condition. If instead of interpreting the vortex sheet simply as a velocity difference at the fluid-solid interface, we think of it as an infinitely thin

layer of vorticity in the fluid, then by diffusing the sheet into the fluid, we automatically leave behind a solid surface with the no-slip condition enforced. A more involved and detailed description of this process can be found in [11], but the key idea is that vorticity dynamics near a surface can be divided into four steps:

1. advect vorticity with inviscid dynamics
2. create bound vortex sheets to enforce no-flow-through
3. inject vorticity from the bound vortex sheet into the fluid
4. and diffuse the ambient vorticity.

While there are viscous vortex methods that deal with the last step, most vortex models in aerodynamics are concerned with how to model the first three. In this work, we will focus on inviscid models where the wing is represented as an infinitely thin, rigid plate. The properties of the bound vortex sheet around the thin plate are well understood, so the modeling choices revolve mainly around the inviscid advection step and vorticity injection step. The key variations among the different vortex models stem from how they address these two steps. This allows us to characterize most vortex models by how they answer the following questions:

- How should regions of vorticity be represented and moved?
- How should new vorticity be injected into the flow?

2.2 Modeling Regions of Vorticity

The most simple representation of vorticity is a point vortex. The velocity induced by a point vortex is given by

$$\boldsymbol{u}_{\text{pv}}(\boldsymbol{\xi}) = \frac{\boldsymbol{\Gamma}_{\text{pv}}}{2\pi} \times \frac{\boldsymbol{\xi} - \boldsymbol{x}_{\text{pv}}}{\left|\boldsymbol{\xi} - \boldsymbol{x}_{\text{pv}}\right|^2}. \tag{2.12}$$

The singular behavior as $\boldsymbol{\xi} \to \boldsymbol{x}_{\text{pv}}$ can lead to very large velocities in clouds of point vortices. It also means that we cannot represent a continuous distribution of vorticity by increasing the number of point vortices used [35]. There have been many schemes for handling the singularity numerically. For instance, in an early vortex model by Sarpkaya [50], when two point vortices come within a threshold distance of each other, they are merged into a single vortex. A more popular approach regularizes the induced velocity by using a smoothed blob kernel

$$\boldsymbol{u}_{\text{pv},\epsilon}(\boldsymbol{x}) = \frac{\boldsymbol{\Gamma}_{\text{pv}}}{2\pi} \times \frac{\boldsymbol{x} - \boldsymbol{x}_{\text{pv}}}{\left|\boldsymbol{x} - \boldsymbol{x}_{\text{pv}}\right|^2 + \epsilon^2}. \tag{2.13}$$

We will refer to these regularized point vortices as vortex blobs.

The vortex sheet is another commonly used vortex element. It represents a discontinuity in the velocity field where the tangential velocities on either side of the sheet are allowed to be different, while the velocities normal to the sheet are required to be equal. The strength of the sheet, $\boldsymbol{\gamma}$, is determined by the difference in the tangential velocities along the sheet. The velocity induced by a vortex sheet along the contour $\mathcal{C}$ is given by

$$\boldsymbol{u}_{\text{vs}}(\boldsymbol{\xi}) = -\frac{1}{2\pi} \int_{\mathcal{C}} \boldsymbol{\gamma}_{\text{vs}} \times \frac{\boldsymbol{\xi} - \boldsymbol{x}_{\text{vs}}(\lambda)}{\left|\boldsymbol{\xi} - \boldsymbol{x}_{\text{vs}}(\lambda)\right|^2} \, \mathrm{d}\lambda. \tag{2.14}$$

Unlike a point vortex, a vortex sheet induces a velocity on itself. The governing equation for self-induced evolution of a vortex sheet is given by the Birckhoff-Rott equation. Unfortunately, Moore [42] showed that the evolution of the vortex sheet is unstable. Without viscosity to dampen short-wavelength disturbances, the growth of Kelvin-Helmhotz instabilities eventually results in parts of the sheet having infinite curvature. Practically, this means that even the round-off error from numerical simulations will cause the vortex sheet to become unstable [30].

Instead of using point vortex approximations of the vortex sheet, vortex blobs are used

to artificially damp out small scale disturbances [31]

$$\boldsymbol{u}_{\mathrm{vs},\epsilon}(\boldsymbol{\xi}) = -\frac{1}{2\pi}\int_{\mathcal{C}} \boldsymbol{\gamma}_{\mathrm{vs}} \times \frac{\boldsymbol{\xi} - \boldsymbol{x}_{\mathrm{vs}}(\lambda)}{|\boldsymbol{\xi} - \boldsymbol{x}_{\mathrm{vs}}(\lambda)|^2 + \epsilon^2}\,\mathrm{d}\lambda. \tag{2.15}$$

Hald and Del Prete [21] has shown that the vortex blob method converges to the solution for Euler's equation. More recently, Nitsche, Taylor, and Krasny [44] compared the results from a high-fidelity viscous simulation against results from a vortex sheet simulation using a blob kernel. They found that while the detailed properties do not converge, the vortex sheet was able to capture much of the large scale behaviors of the flow.

2.3 Vorticity Generation

Since the diffusion of vorticity into the fluid is a viscous phenomenon, we need to a way to model it in an inviscid setting. We will focus our discussion on the vorticity generation from an infinitely thin, flat plate.

An interesting characteristic of the infinitely thin plate is that it cannot support flow around its edges. The fluid velocity at the edges of the plate is either tangent to the plate, or infinite and normal to the plate. If the velocity is infinite at an edge, we also have an infinite negative pressure at that edge. The infinite pressure, integrated across a vanishingly thin area, gives rise to finite suction forces.

The most common criterion for determining vorticity flux from a flat plate, the Kutta condition, requires that new vortex elements be released with strengths that eliminate this singular behavior. The Kutta condition was originally used at the trailing edge of the plate, as the angles of attack in the earlier models were low enough that there was no vorticity flux from the leading edge. Although the Kutta condition has also been used at the leading edge [5, 26, 59], it has mostly been restricted to flows at high angles of attack. Since enforcing the Kutta condition requires the fluid velocity at the plate edges to be

tangent to the plate, applying it to the leading edge at low angles of attack means that flow has to move in the opposite direction as the freestream. This behavior is not only physically not justifiable, it is also difficult to handle numerically.

Recently, Ramesh and Gopalarathnam [47] introduced a leading edge vortex shedding criterion based on the observation that real airfoils can support a critical amount of suction before flow separation occurs. Correspondingly, Ramesh and Gopalarathnam defined a leading edge suction parameter (LESP) that measures the suction at the leading edge caused by the singular velocity. In their model, vortex elements are only released at the leading edge if the LESP exceeds a critical value. The newly released vortex elements are then responsible for bringing the suction parameter back down to the critical value. For the low angle of attack flows considered in this thesis, we will be using this critical LESP vortex shedding criterion.

2.4 Overview of Existing Models

2.4.1 Fixed-Wake Models

We first consider the flow around an airfoil at a low angle of attack that starts translating from rest. The requirement for low angle of attack allows us to assume that the flow is attached at the leading edge of the airfoil, and that vortex shedding comes mainly from the trailing edge. The bulk of this vorticity comes from the bound vortex sheet necessary to enforce no-flow-through and the Kutta condition during the impulsive start of the airfoil's motion. Once the bound vortex sheet has been built up and the initial trailing edge wake has advected far from the body, only slight changes to the sheet's strength is enough to maintain the boundary conditions. The coarsest model for this system can be made by assuming that the airfoil has achieved its final velocity and has been translating steadily

for a long time, and that the bulk of the shed vorticity is far from the airfoil. The system can be modeled as a single point vortex at infinity, with no additional injection of vorticity into the wake. This assumption results in the Kutta-Joukowski lift theorem

$$L_\infty = \rho U_\infty \Gamma. \tag{2.16}$$

Furthermore, since we assume that the Kutta condition is always maintained, the strength of the starting vortex must be

$$\Gamma = U_\infty L \sin\alpha. \tag{2.17}$$

The steady state lift is then

$$L_\infty = \rho U_\infty^2 L \sin\alpha \approx \rho U_\infty^2 L\alpha \tag{2.18}$$

We can add another layer of sophistication to the Kutta-Joukowski model for transient flows. Instead of a single point vortex at infinity, the airfoil continuously deposits vorticity from its trailing edge as it moves. At every instant, the vorticity shed from the plate has the appropriate strength to enforce the Kutta condition. In order to make the problem more approachable by analytical methods, the trailing edge wake was assumed to be stationary, and changes in angle of attack are assumed to be small. This model was the first vortex model for unsteady aerodynamics, also known as the Wagner model [58]. Wagner computed the response of the force and circulation around the airfoil to a step change in angle of attack. The response to arbitrary (but small) motion could be found by convolving appropriately scaled step responses. This process is shown in Figure 2.1. The top row begins the impulsive translation of the airfoil (equivalent to a step change in angle of attack from 0°). When the airfoil reaches the position indicated in the middle row, it reverses its angle of attack while continuing its motion forward. The resulting distribution of vorticity along the wake, indicated by the color, can be computed by convolving the appropriate

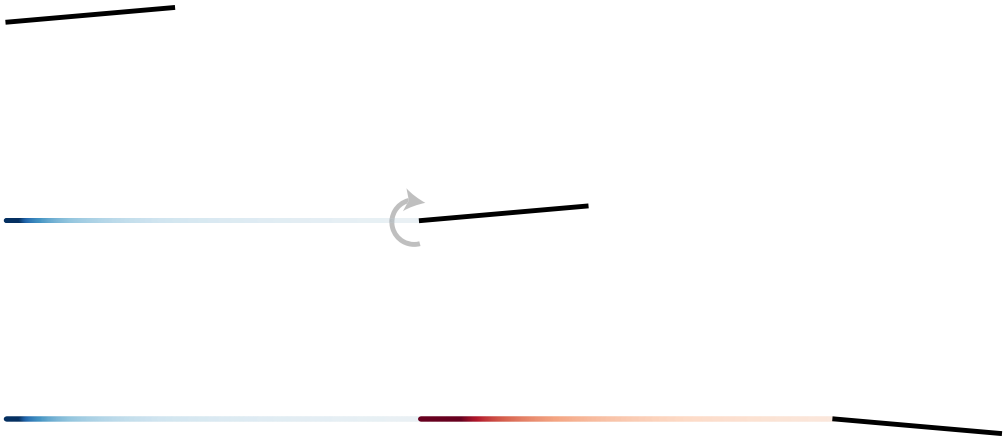

Figure 2.1: Flat-wake model of the vorticity distribution along the trailing edge wake as the airfoil performs an impulsive pitch.(Top) Beginning of impulsive translation. (Middle) Impulsive reversal of angle of attack. (Bottom) Continued translation at new angle of attack.

step responses. While Wagner formulated the model in the time-domain, Theodorsen approached the same problem through a frequency-domain method, with Garrick showing that the two approaches are equivalent [57, 27, 19].

2.4.2 Dynamic-Wake Models

At higher angles of attack, there is flow separation from the leading edge, and the interaction between the leading edge vortices and trailing edge vortices often lead to nonlinear behavior that the linear models cannot capture. For these problems, the assumption of a linear, stationary wake is insufficient. To model vortex shedding from both edges, researchers released vortex elements from both edges of the plate [50, 28, 5, 26]. In Figure 2.2, we compare the computed distribution of vorticity around a plate translating at 60° angle of attack. The top row shows results from a high-fidelity simulation of viscous flow at Reynolds number of 1000. The second row shows the result when we use point vortices as our vortex elements. This is similar to the work by Sarpkaya [50], except point vortices are not merged together. The third row shows the results when we use vortex

sheets instead, as in the work by Jones [26].

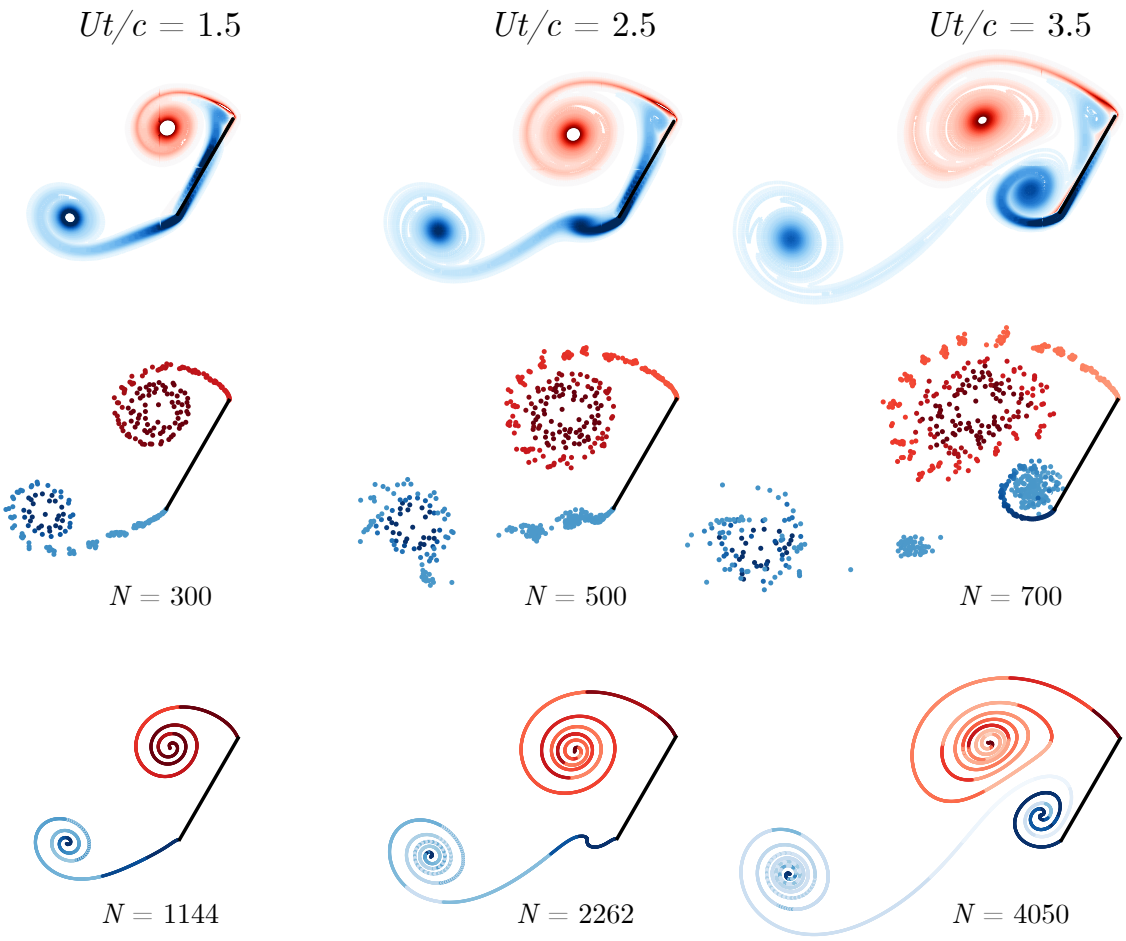

Figure 2.2: Comparison of the predicted large scale structures around the plate using high fidelity CFD at $\mathrm{Re} = 1000$ (top row), a point vortex model (middle), and a vortex sheet model (bottom row). The CFD results show the vorticity contours. The vortex models show the strength and positions of the vortex sheets and point vortices, as well as the number of control points used to model the vorticity field.

From the figures, it is clear that both the point vortex model and the vortex sheet model can capture the dominant vortical structures in the flow field. In the second column, where the shear layer connecting the plate to the trailing edge vortex starts to roll up, we see that the smoothed coherent structure provided by the vortex sheet method makes it much easier to identify the shear layer instability than the point vortex method. This extra layer of detail comes at the expense of computational cost. In order to maintain smooth connec-

tivity along the sheet, points are routinely inserted into parts of the sheet where curvature is high. While the number of computational elements used for the point vortex model increased linearly with time, the number of vortex sheet elements grew almost quadratically. Even if fast $O(n)$ particle methods are used to speed up the pairwise velocity computations, the continuous increase in particles mean that these methods cannot be used for real-time applications [20, 13].

2.4.3 Variable-Strength Vortex Models

While the methods described in the previous section captured the flux of vorticity into the flow by releasing new vortex elements, there is another class of methods that model vorticity flux by using point vortices with time-varying strength [7, 56, 59, 41]. In these models, the dominant leading edge and trailing edge vortices are each modeled with a single point vortex. The roll-up of the shear layers into large scale structures is modeled by increasing the magnitude of the point vortices' circulation. Brown and Michael [7] showed that changing the strength of the point vortices introduced a pressure discontinuity in the fluid, creating a fictitious force. While there is no way of removing the pressure discontinuity, the velocities of the variable-strength point vortices can be modified so that an additional force cancels out the effect of the pressure jump. More recently, Wang and Eldredge [59] developed an alternate model where instead of canceling out the pressure jump in the fluid, the point vortices are moved in a way so that the instantaneous force on the immersed body is unaffected by discontinuous flux of vorticity into the fluid.

While the low number of computational elements make this class of methods much more suitable for real-time applications, it also results in the models missing crucial flow physics. Without a way to model the shear layers between the plate and the large coherent vortices, these variable-strength vortex models cannot capture the transformation of a shear-layer instability into a new coherent vortex.

2.5 Aerodynamic Force

The force on a solid body moving through a fluid is typically calculated by either integrating the surface traction forces or by determining the change in momentum of the fluid. Since our fluid domain is only internally bounded, the time derivative of the total fluid momentum will require us to determine the momentum of the fluid all the way out to infinity. However, since the velocity field decays as r^{-2} in two dimensions and r^{-3} in three dimensions, the momentum velocity integral over the entire fluid domain is not absolutely convergent [63]. While we can determine the pressure and shear stress from the velocity field, it will be more helpful to determine force in terms of just velocity and vorticity.

The force on an immersed body, $\boldsymbol{F}$, can be written in terms of the linear impulse of the fluid, P as [14, 63]

$$\boldsymbol{F} = -\rho \frac{\mathrm{d}\boldsymbol{P}}{\mathrm{d}t}, \tag{2.19}$$

which can be expressed in terms of vorticity and velocity

$$\boldsymbol{F} = -\rho \frac{\mathrm{d}}{\mathrm{d}t} \left\{ \int_{R_f} \boldsymbol{x} \times \boldsymbol{\omega} \, \mathrm{d}R + \oint_{S_b} \boldsymbol{x} \times \boldsymbol{\gamma} \, \mathrm{d}S + \oint_{S_b} \boldsymbol{x} \times (\hat{\boldsymbol{n}}_{bf} \times \boldsymbol{u}_b) \, \mathrm{d}S \right\} \tag{2.20}$$

The first integral represents the impulse of the ambient fluid, the second integral represents that impulse of the vortex sheet at the fluid-solid interface, and the last term is the effect of added mass on the solid.

Chapter 3

A Hybrid Vortex Sheet/Point Vortex Model

We want a model that is dynamically rich enough to capture the detailed vortex dynamics near the wing. One possible choice is to use a vortex sheet model. By monitoring the dynamics of the sheets, we can detect the growth of new coherent vortices in the fluid. However, as each vortex sheet is represented discretely by a large collection of vortex particles, the use of spiraling sheets to model growing coherent vortices is computationally expensive. In an attempt to minimize computational time, we follow the examples of the low-order models and represent each coherent vortex with a single point vortex. The growth of these large-scale vortices can then be modeled by transferring vorticity from the tips of the vortex sheets into the point vortices. Though this hybrid representation has been used to a limited degree in some previous studies [46, 26], the approach we follow here is unique in that it is able to ensure that the force exerted on the plate is not spuriously affected by this transfer of circulation. This makes use of an extended version of the impulse-matching principle that was developed by Wang and Eldredge [59]. By using both vortex sheets and point vortices, we show that we can limit the number of vortex particles in our model without losing the ability to naturally create new vortex structures.

3.1 Model Formulation

We model the ambient vorticity with three types of vortex elements:

- a vortex sheet rooted at each edge of the wing to represent the shear layers

- an *active* point vortex with time-varying strength associated with each vortex sheet to represent its rolled-up core
- a collection of *inactive*, constant strength, point vortices to represent large-scale vortex structures in the wake

The vortex sheets themselves are constructed as an ordered collection of vortex blobs. As noted by Moore [42] and Krasny [30], these sheets are inherently unstable and will amplify errors from numerical round-off. To suppress these small-scale instabilities, we apply Fourier filtering along the lengths of the vortex sheets at every time-step.

The wing is modeled as an infinitely thin, flat plate undergoing rigid body motion. At every time-step, we enforce the Kutta condition at both edges of the plate by adding new segments of circulation to the plate-end of the vortex sheets. At the same time, we trim the number of vortex elements in our system by transferring circulation from the wake-end of the sheets into the active point vortices.

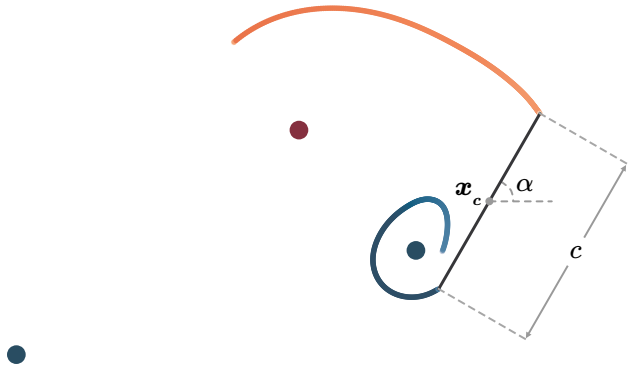

Figure 3.1: $\boldsymbol{x}_c$, α, and c denote the centroid, angle of attack, and chord length of the plate. Each vortex sheet has an associated point vortex that it feeds circulation into.

3.2 Aggregating Vortex Elements

While previous works [10, 9, 48] also aggregated vortex elements to reduce computational cost, they focused on *identifying* elements that can be merged without adversely

affecting the vorticity field. These merging schemes tend to restrict the circulation and distances between the mergeable vortex elements. In contrast, we typically do *not* want the tips of our vortex sheets to be near their associated point vortex in order to avoid simulating the details of vortex sheet roll-up. As shown in Figure 3.1, we want to transfer circulation from the vortex sheets directly to the point vortex representing its core. Since we are ultimately interested in the force exerted by the fluid on the plate, we will instead construct the transfer process to preserve the model's force response.

3.2.1 Effect of Circulation Transfer on Force

Let $\boldsymbol{F}$ be the force exerted on a body as it moves through a fluid with density ρ. If $\boldsymbol{P}$ is the linear impulse of the fluid, then

$$\boldsymbol{F} = -\rho \frac{\mathrm{d}\boldsymbol{P}}{\mathrm{d}t}. \tag{3.1}$$

In two dimensions, the fluid impulse takes the form:

$$\boldsymbol{P} = \int \boldsymbol{x} \times \boldsymbol{\omega} \, \mathrm{d}A + \oint \boldsymbol{x} \times \boldsymbol{\gamma} \, \mathrm{d}l + \oint \boldsymbol{x} \times (\hat{\boldsymbol{n}} \times \boldsymbol{u}_B) \, \mathrm{d}l, \tag{3.2}$$

where

- $\boldsymbol{\omega}$ is the vorticity in the fluid
- γ is the strength of the bound vortex sheet on the body
- $\hat{\boldsymbol{n}}$ is normal vector on the body surface
- and $\boldsymbol{u}_B$ is the velocity at the body surface.

Since our wing is modeled as a plate with infinitesimal thickness, the last integral in Equation (3.2) is zero, leaving us only the impulse from ambient vorticity and the bound vortex sheet. The bound vortex sheet is necessary to maintain the no-flow-through condition on

the body surface. If we decompose the ambient vorticity field into N_v discrete vortex elements, then we can interpret the bound vortex sheet as a superposition of $N_v + 1$ sheets, that is

$$\boldsymbol{\gamma} = \sum_{i=1}^{N_v} \boldsymbol{\gamma}_i + \boldsymbol{\gamma}_B, \tag{3.3}$$

where each $\boldsymbol{\gamma}_i$ cancels out the body normal velocity induced by the i-th vortex element, and $\boldsymbol{\gamma}_B$ cancels out the normal velocity due to the body's motion. We take advantage of this interpretation and decompose the fluid impulse into two components $\boldsymbol{P}_A$ and $\boldsymbol{P}_B$, where

$$\boldsymbol{P} = \boldsymbol{P}_A + \boldsymbol{P}_B \tag{3.4}$$

with

$$\boldsymbol{P}_A = \sum_{i=1}^{N_v} \boldsymbol{x}^i \times \boldsymbol{\Gamma}_A^i + \oint \boldsymbol{x} \times \boldsymbol{\gamma}^i \, \mathrm{d}l \tag{3.5}$$

and

$$\boldsymbol{P}_B = \oint \boldsymbol{x} \times \boldsymbol{\gamma}_B \, \mathrm{d}l \tag{3.6}$$

The component $\boldsymbol{P}_A$ depends only on the ambient vorticity, and $\boldsymbol{P}_B$ depends only on the motion of the body. The force exerted on the body can then be expressed as

$$\boldsymbol{F} = -\rho \left(\frac{\mathrm{d}\boldsymbol{P}_A}{\mathrm{d}t} + \frac{\mathrm{d}\boldsymbol{P}_B}{\mathrm{d}t} \right). \tag{3.7}$$

Since $\boldsymbol{P}_B$ is independent of the vortex dynamics, the process of transferring circulation between vortex elements will only influence $\mathrm{d}\boldsymbol{P}_a/\,\mathrm{d}t$. Denote by $\boldsymbol{p}(\boldsymbol{x}, \Gamma)$ the function that takes as inputs the position $\boldsymbol{x}$ and circulation Γ of a vortex element and returns the impulse of that element and its associated bound vortex sheet, i.e.

$$\boldsymbol{P}_A = \sum_{i=1}^{N_v} \boldsymbol{p}(\boldsymbol{x}_i, \Gamma_i). \tag{3.8}$$

Then we have

$$\frac{\mathrm{d}\boldsymbol{P}_A}{\mathrm{d}t} = \sum_{i=1}^{N_v} \left(\left.\frac{\mathrm{d}\boldsymbol{p}}{\mathrm{d}\boldsymbol{x}}\right|_{\boldsymbol{x}_i,\Gamma_i} \dot{\boldsymbol{x}}_i \right) + \left(\left.\frac{\mathrm{d}\boldsymbol{p}}{\mathrm{d}\Gamma}\right|_{\boldsymbol{x}_i,\Gamma_i} \dot{\Gamma}_i \right). \tag{3.9}$$

For real flows, Kelvin's circulation theorem requires circulation to be a material quantity, with $\dot{\Gamma}_i$ equal to zero. If we violate this restriction, we will introduce a spurious force that is proportional to $\dot{\Gamma}_i$.

3.2.2 Impulse-Matching Velocity Correction

As we are intent on transferring circulation, we will mitigate the unwanted change to the force by modifying the velocity of a vortex element. Let us denote the vortex elements we are transferring circulation between with subscripts s and t (for source and target). To conserve total circulation, we feed circulation into the target element at the same rate that we draw it from the source element, that is

$$\dot{\Gamma} = \dot{\Gamma}_t = -\dot{\Gamma}_s.$$

We now modify the velocity of the target element such that

$$-\frac{1}{\rho}\Delta\boldsymbol{F} = \left(\left.\frac{\mathrm{d}\boldsymbol{p}}{\mathrm{d}\boldsymbol{x}}\right|_{\boldsymbol{x}_t,\Gamma_t} \Delta\dot{\boldsymbol{x}}_t \right) + \dot{\Gamma} \left(\left.\frac{\mathrm{d}\boldsymbol{p}}{\mathrm{d}\Gamma}\right|_{\boldsymbol{x}_t,\Gamma_t} - \left.\frac{\mathrm{d}\boldsymbol{p}}{\mathrm{d}\Gamma}\right|_{\boldsymbol{x}_s,\Gamma_s} \right) = 0, \tag{3.10}$$

leaving the force on the plate unaffected by the circulation transfer procedure. In our model, we will be transferring circulation from a vortex sheet to a point vortex. We defer the derivation of the velocity correction to Appendix B and simply present the result below. To streamline the presentation, we will use complex coordinates where $z = x + \mathrm{i}y$ is the complex coordinates of the point vortex in inertial space, z_c is the complex position of the plate centroid, and $\tilde{z}$ is the position of the point vortex in a plate-centered frame of

reference

$$\tilde{z} := \frac{2\mathrm{e}^{-\mathrm{i}\alpha}}{c}(z - z_c).$$

The velocity correction, in inertial coordinates, can then be written as

$$\Delta \dot{z}_t = \mathrm{i}\mathrm{e}^{\mathrm{i}\alpha}\frac{c}{2}\left(\frac{(\hat{p}_s - \hat{p}_t)(\beta^\star + 1) - (\hat{p}_s^\star - \hat{p}_t^\star)(\beta^\star - 1)}{\beta + \beta^\star}\right)\frac{\dot{\Gamma}}{\Gamma_t} \tag{3.11}$$

where * denotes complex conjugation,

$$\hat{p}_i := \mathrm{Im}\left\{\tilde{z}_i\right\} - \mathrm{i}\mathrm{Re}\left\{\sqrt{\tilde{z}_i - 1}\sqrt{\tilde{z}_i + 1}\right\}$$

and

$$\beta := \frac{\tilde{z}_t}{\sqrt{\tilde{z}_t - 1}\sqrt{\tilde{z}_t + 1}}.$$

3.2.3 Circulation Transfer Rate

This circulation transfer process can be thought of as a real-time model order reduction process in which the circulation transfer rate, $\dot{\Gamma}$, is at the discretion of the user. A small $\dot{\Gamma}$ magnitude may not be able to remove circulation from the sheet as fast as new circulation is introduced into it from the edge. However, a large $\dot{\Gamma}$ might change the vorticity distribution so drastically that the new reduced-order model might no longer observe the same dynamics as the original system. Consider a circulation transfer that takes place over the time interval $[t_0,\, t_0 + \Delta t]$. The velocity correction can only guarantee that the force predicted by the reduced model is equal to the force predicted by the original model at time t_0. Since circulation transfer is not a lossless reduction of order, the small differences between the two models means that, in general, the forces that they predict at time $t_0 + \Delta t$ will be different. We can pick $\dot{\Gamma}$ to bound the difference between the predicted forces over Δt to be below an error threshold, denoted as ϵ_F.

In practice, our vortex sheets are represented as ordered collections of regularized point vortices and our model is evolved forward in time with discrete time-marching. The strength of each of these vortex elements of the sheet is proportional to the time-step size, since each such element is formed from the circulation flux from the plate's edge over some previous time-step. The transfer of circulation from the sheet into the target point vortex over time-step Δt comprises an elimination of some finite number of sheet elements from the edge of the sheet. So at every time-step, we first compute the force that the model will predict if no circulation transfer occurs. We transfer circulation from as many of the regularized point vortices as we can (thereby eliminating these vortices from the sheet) into the active point vortex, stopping only when the accumulated error in predicted force exceeds ϵ_F.

There are instances where even transferring circulation from a single point vortex from the sheet results in large errors in the predicted force. We treat this as an indication that the tip of the vortex sheet and the active point vortex are becoming dynamically distinct, suggesting the possibility of a new vortex core. At this point, we can freeze the strength of the active point vortex, and convert the tip of the vortex sheet into the new active point vortex. A large number of new active point vortices may be released in quick succession when small instabilities form near the tip of the vortex sheet. In order to make the method more robust to these instabilities, we require a minimum time interval between the release of new active point vortices, which we will refer to as Δt_{min}.

The selection of ϵ_F and Δt_{min} leads to the complete taxonomy of inviscid vortex models. Suppose we set $\epsilon_F = 0$ and $\Delta t_{\text{min}} = 0$. This means that no circulation transfer occurs due to the zero tolerance for error, and the sheet's last vortex element is converted into a distinct point vortex at every time-step. This leads to a traditional discrete vortex element model [50, 28, 64]. Alternatively, if we set $\epsilon_F = 0$ and $\Delta t_{\text{min}} = \infty$, then we will never transfer circulation to the active point vortex, but no new point vortices will ever be created, leaving us essentially with a vortex sheet model [26, 51, 2]. If we instead make $\epsilon_F = \infty$, then any

circulation shed from the plate to the sheet through the Kutta condition is immediately absorbed by the active point vortex, giving us a version of the Wang and Eldredge model. Alternatively, if we substitute the modified velocity of this vortex derived here for the Brown-Michael equation [7], we would obtain the variable-strength vortex models based on that equation [41].

Once we have picked values of ϵ_F and Δt_{min}, then we perform the following procedure at every time-step:

1. For every point vortex comprising the vortex sheet, we determine the velocity correction it will contribute to the active point vortex if we transfer all of its circulation to that vortex.

2. Advect all vortex elements forward in time and compute their individual impulse.

3. Starting from the wake end of each vortex sheet, we attempt to transfer circulation. Suppose we have already transferred circulation from n_v number of point vortices from the vortex sheet, and we are attempting to transfer the $(n_v + 1)$-th one. Then:

   (a) We compute the impulse of the active point vortex with the accumulated circulation and velocity correction from the $n_v + 1$ point vortices .

   (b) If the difference between this impulse and that accumulated from the $(n_v + 1)$ point vortices is less than $\Delta t \cdot \epsilon_F$, then we transfer the circulation of this vortex (and eliminate the vortex from the sheet), and return to step 3a and proceed to the next vortex in the sheet.

4. If $n_v > 0$, or the time since we last created a new point vortex is less than Δt_{min}, then we continue to step 5. Otherwise, we turn the current active point vortex into an inactive one, and the tip of the vortex sheet into the new active point vortex.

5. Apply Fourier filtering to the vortex sheet to redistribute the point vortices evenly along the sheet and remove small-scale instabilities.

6. Add new vortex sheet segment at the root of each sheet to enforce the Kutta condition.

3.3 Results

In this section, we use the proposed method to model the impulsive translation of a plate at high angles of attack, as well as pitch-up maneuvers. During the pitching motion, which starts at t_1 and ends at t_2, the leading edge of the plate translates horizontally at a constant velocity, U, while the angle of attack goes from 0° to $\alpha_f = 90^\circ$ as a smoothed linear ramp given by

$$\alpha(t) = \frac{K}{a_s} G(t) \tag{3.12}$$

where $K := \alpha_f/(t_2 - t_1)c/(2U)$ is the non-dimensional pitch rate, a_s is a smoothing parameter, and

$$G(t) = \log\left[\frac{\cosh(a_s U(t - t_1)/c)}{\cosh(a_s U(t - t_2)/c)}\right] + a_s U(t_1 - t_2)/c \tag{3.13}$$

is a smooth ramp function.

3.3.1 Impulsive Translation at Fixed Angles of Attack

We start by considering the case with 45° angle of attack. In Figure 3.2, we compare the vorticity distribution predicted by the hybrid model, a vortex sheet model, and a $\mathrm{Re} = 500$ high-fidelity Navier-Stokes simulation after one and three convective times. The high-fidelity CFD simulations are performed with the immersed boundary projection method developed by Taira and Colonius [53]. The hybrid model results presented in the figure uses a minimum vortex release interval of $\Delta t_{\text{min}} = 0.2c/U$, and an error threshold of $\epsilon_F = 0.001\rho U^2 c$. We see that the hybrid model captures the same large-scale vortex structures as

the vortex sheet model while using an order of magnitude fewer computational elements. In Figure 3.4, where we compare the lift and drag coefficients predicted by the hybrid model, the Wang and Eldredge model (i.e. only two variable-strength point vortices and no sheets), and CFD results, we see that it is important that we do not completely eliminate the vortex sheets. The sheets enable the model to naturally capture the formation of new coherent vortices, which then triggers large-scale vortex shedding. This mechanism allows the hybrid model to give a more accurate force prediction than existing variable-strength point vortex models.

We show the effects of changing the minimum vortex release interval in Figure 3.5. We see that a small Δt_{min} gives results that are more similar to those from discrete vortex models. As we increase Δt_{min}, more circulation is fed into each active point vortex, so we *decrease* the total number of vortex particles in the model. However, very large values of Δt_{min} tend to result in longer vortex sheets, which significantly *increase* the number of computational elements. Since we would rather represent large-scale vortex structures using a handful of point vortices than as tightly spiraled vortex sheets, Δt_{min} should be around the expected vortex shedding period. In Figure 3.3, we show how different values of Δt_{min} affect the number of vortex particles used in the model over time. While the sharp increase in particle count corresponds to the lengthening and growth for the vortex sheets, the sharp drops correspond to the growth of active point vortices as they consume the sheets. As long as Δt_{min} is small enough to prevent the vortex sheet from growing faster than its active point vortex can absorb it, we can keep the particle count low enough to simulate flows over extended periods in real-time.

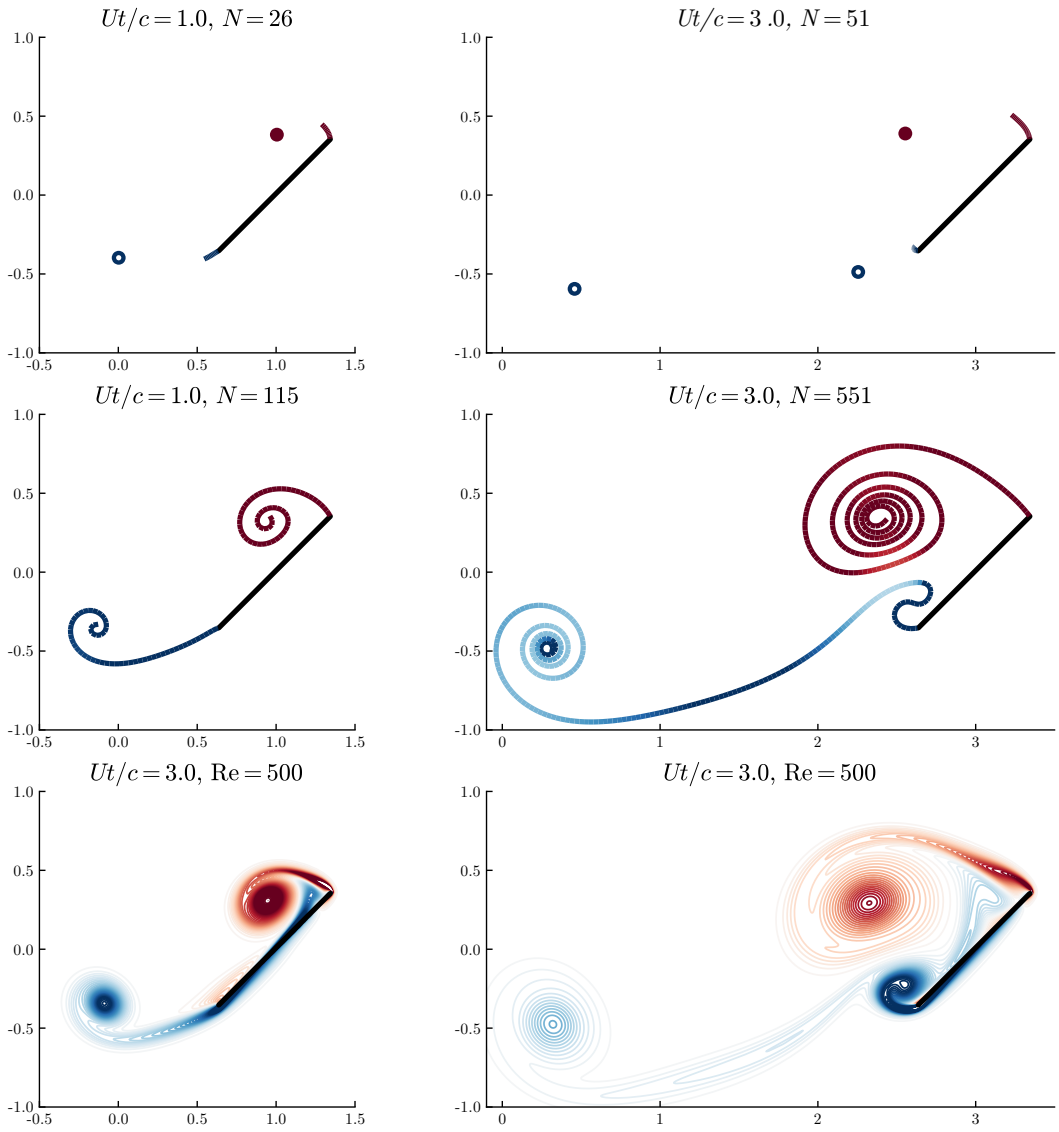

Figure 3.2: Comparison of the vorticity distribution predicted at one convective time **(left)**, and three convective times **(right)** between the proposed hybrid model **(top)**, a vortex sheet model **(middle)**, and high-fidelity CFD at $\mathrm{Re} = 500$ **(bottom)**. The positions of the positive and negative strength point vortices are shown with filled and unfilled circles, respectively, and N denotes the total number of computational elements.

A concern with using a minimum vortex release interval is that it will introduce a $1/\Delta t_{\text{min}}$ frequency component to the system and cause vortex shedding to lock-on to that frequency. We can see that this is not the case in Figure 3.6, as $U\Delta t_{\text{min}}/c = 0.1, 0.2, 0.25$ all predict essentially the same force response.

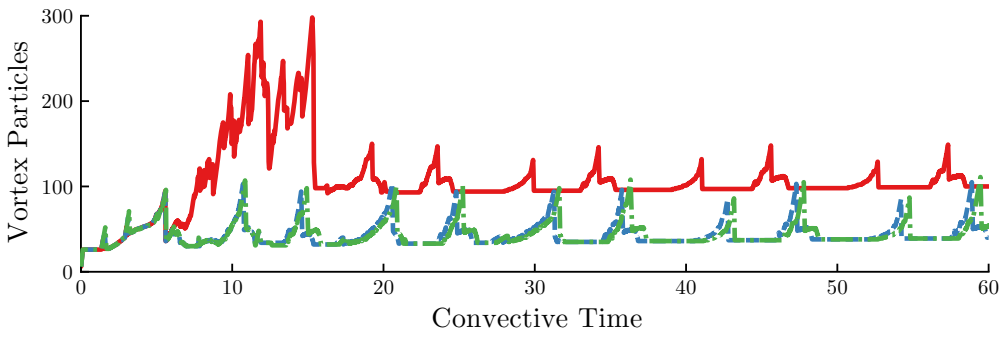

Figure 3.3: Comparison of the number of vortex particles used over time to simulate impulsive translation at $45°$ using different values of minimum vortex release time interval: : $U\Delta t_{\text{min}}/c = 0.1$ **(—)**, $U\Delta t_{\text{min}}/c = 0.2$ **(– –)**, $U\Delta t_{\text{min}}/c = 0.25$ **(–·–)**.

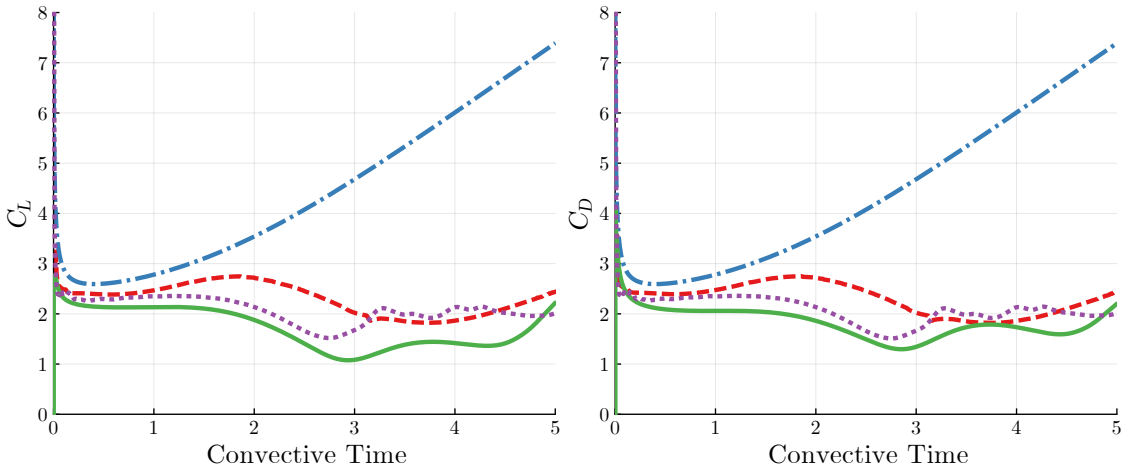

Figure 3.4: Early-time lift **(left)** and drag **(right)** coefficients for impulsive translation at $\alpha = 45°$ predicted by the hybrid model with $U\Delta t_{\text{min}}/c = 0.2$ **(– –)**, the vortex sheet model **(····)**, the Wang and Eldredge model **(–·–)**, and CFD results as $\text{Re} = 500$ **(—)**.

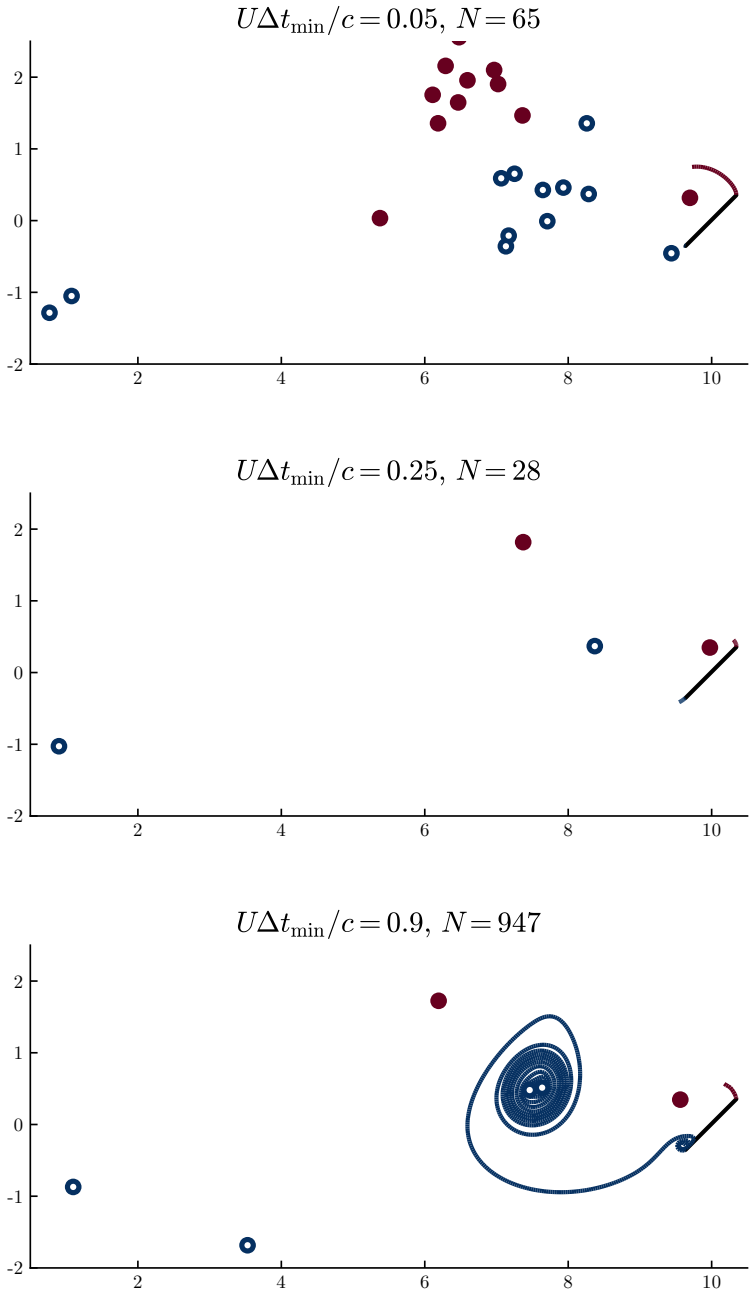

Figure 3.5: Comparison of the circulation distribution around an impulsively translated plate with fixed $\alpha = 45°$ at ten convective times between $U\Delta t_{\min}/c = 0.05$ **(top)**, $U\Delta t_{\min}/c = 0.25$ **(middle)**, $U\Delta t_{\min}/c = 0.9$ **(bottom)**.

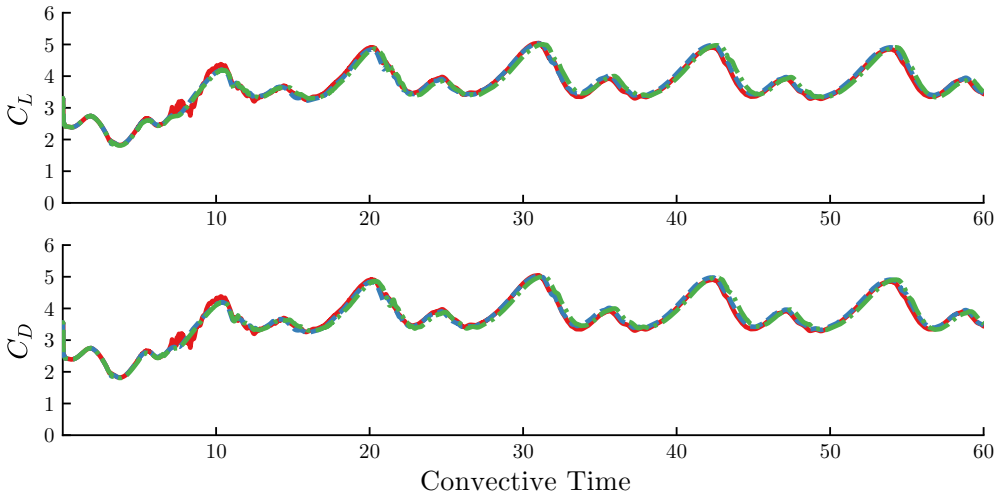

Figure 3.6: Lift and drag coefficients for impulsive translation at $\alpha = 45°$ predicted by the hybrid model with $U\Delta t_{\text{min}}/c = 0.1$**(—)**, $U\Delta t_{\text{min}}/c = 0.2$ **(-·-·)**, and $U\Delta t_{\text{min}}/c = 0.25$ **(- -)**

The results for the $\alpha = 60°$ case are mostly similar to the $\alpha = 45°$ case. Figure 3.7 shows the early time vorticity distribution predicted by the model, and Figures 3.8 and 3.9 show the predicted force response. We see that the initial development of the leading and trailing edge vortices predicted by the hybrid model is very similar to the CFD results. As in the $45°$ case, the ability to model large-scale vortex shedding allows the model to give a more accurate force response than the Wang and Eldredge model.

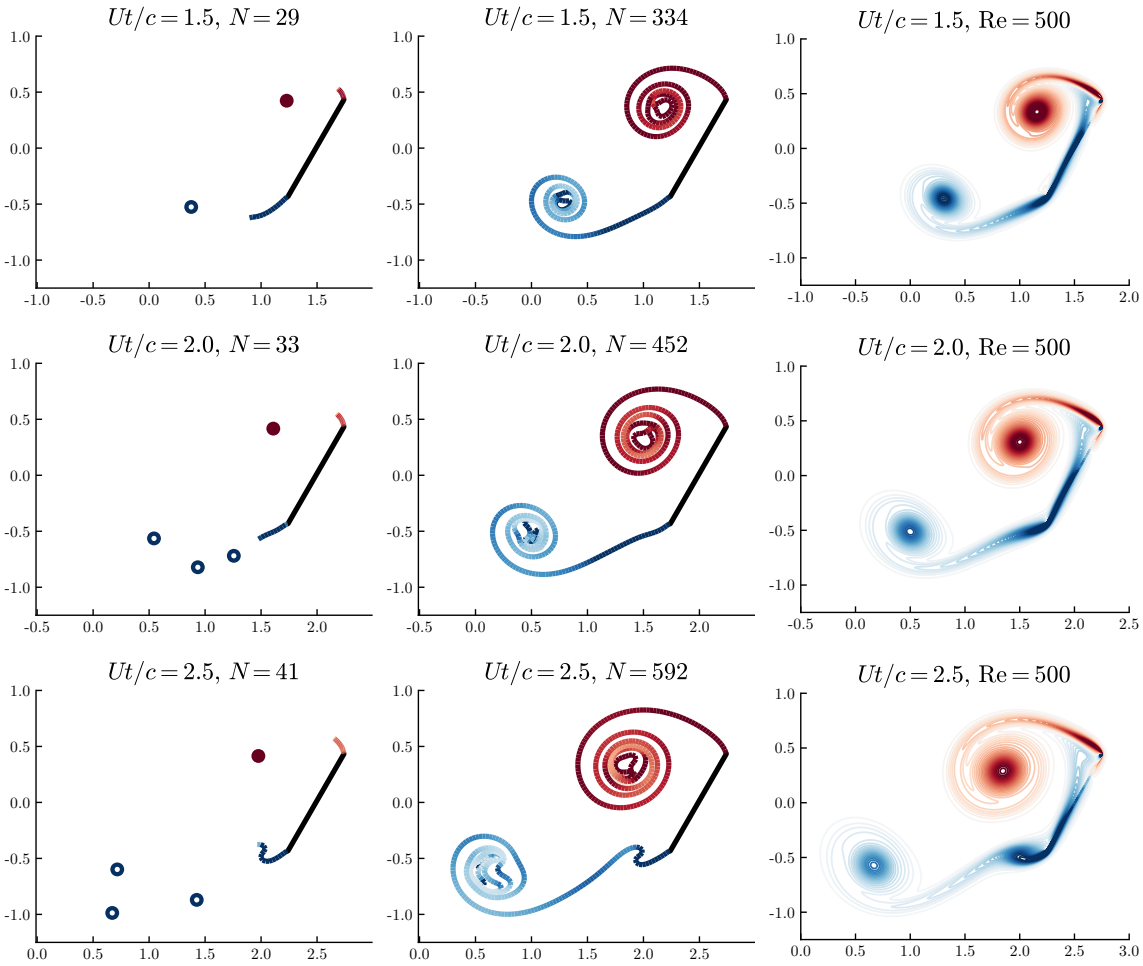

Figure 3.7: Vorticity distribution predicted at different convective times by the proposed hybrid model **(left)**, a vortex sheet model **(center)**, and high fidelity CFD at $\mathrm{Re} = 500$ **(right)**. The positions of the positive and negative strength point vortices are shown with filled and unfilled circles, respectively, and N denotes the total number of computational elements.

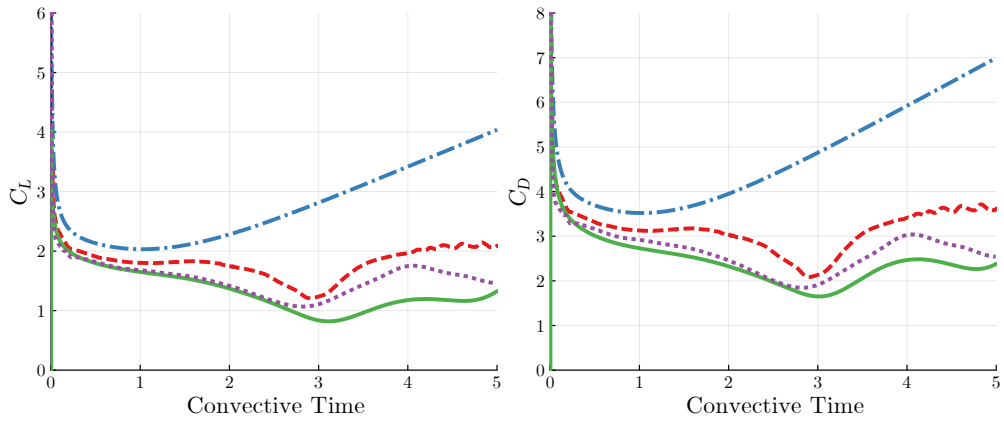

Figure 3.8: Early-time lift **(left)** and drag **(right)** coefficients for impulsive translation at $\alpha = 60°$ predicted by the hybrid model with $U\Delta t_{\text{min}}/c = 0.2$ **(– –)**, the vortex sheet model **(····)**, the Wang and Eldredge model **(–·–)**, and CFD results as $\text{Re} = 500$ **(—)**.

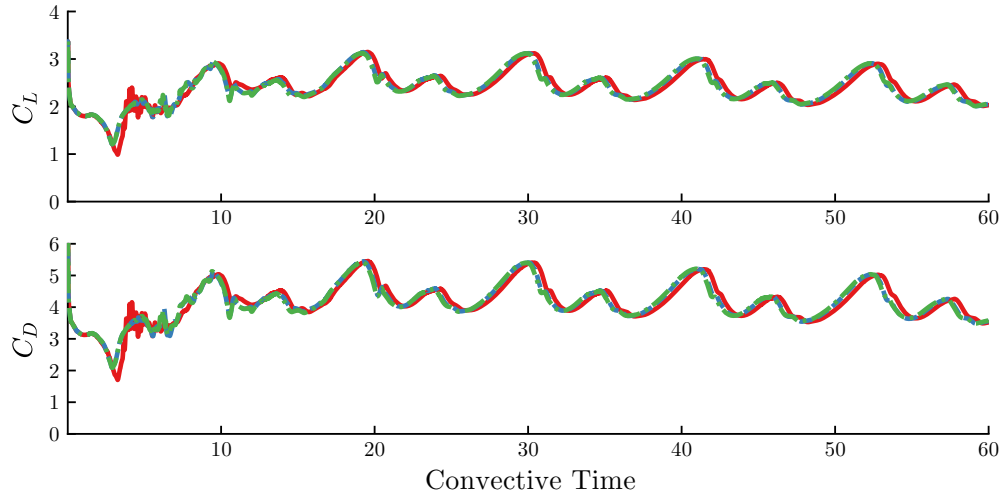

Figure 3.9: Lift and drag coefficients for impulsive translation at $\alpha = 60°$ predicted by the hybrid model with $U\Delta t_{\text{min}}/c = 0.1$**(—)**, $U\Delta t_{\text{min}}/c = 0.2$ **(–·–)**, and $U\Delta t_{\text{min}}/c = 0.25$ **(– –)**

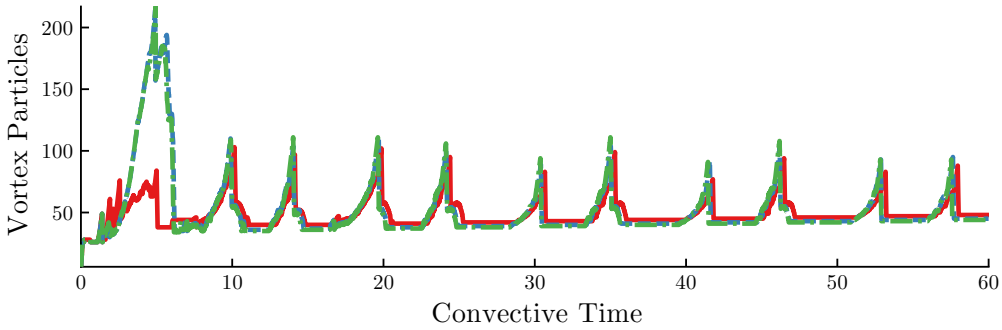

Figure 3.10: Comparison of the number of vortex particles used over time to simulate impulsive translation at 60° using different values of minimum vortex release time interval: : $U\Delta t_{\text{min}}/c = 0.1$ **(—)**, $U\Delta t_{\text{min}}/c = 0.2$ **(– –)**, $U\Delta t_{\text{min}}/c = 0.25$ **(–·–)**.

3.3.2 Pitch up while translating

We now consider pitch up maneuvers, starting with $K = 0.7$. Unlike the high angle of attack cases described previously, the extended amount of time that the plate spends at low angles of attack makes it challenging to release vortex sheets from the leading edge. If we apply the Kutta condition, then it requires the vortex sheet to leave the plate tangent to the plate, in a direction nearly opposite the relative free stream. Instead, we will use the leading edge suction criteria proposed by Ramesh and Gopalarathnam [47]. However, by relaxing the Kutta condition, the singular velocity at the leading edge will introduce large amounts of instability into the vortex sheet. Additionally, at very low angles of attack, the circulation released at the leading edge is so weak that new vortex particles tend to remain near the plate's surface instead of rolling into a sheet. Having these point vortices so close to the plate introduces large fluctuations in the force response due to the large tangential motions generated by the no-flow-through condition. In this case, moving circulation from the sheet to the active point vortex not only absorbs the small-scale instabilities in the sheet, but also tends to move vortex elements away from the plate surface, thus reducing the noise in the force response. Figure 3.12 shows a comparison of the lift and drag coef-

ficients during the pitch up motion. In vortex models with only variable strength point vortices, such as the Wang and Eldredge model, the vorticity flux from the leading edge goes directly into the active leading edge vortex. The fast growth of such a point vortex means that these models tend to over-predict the lift on the plate. In the proposed model, the leading edge circulation is distributed between the active point vortex and the vortex sheet, which gives a more accurate force response. Figure 3.13 shows the lift and drag coefficients as the flow settles down to periodic bluff-body shedding past a plate at normal incidence.

For the $K = 0.2$ pitching case, the plate spends even longer in low angle of attack configurations. From both the vorticity distribution in Figure 3.14 and the predicted force response in Figure 3.15, we see more noise than in the $K = 0.7$ case. In these results, the circulation transfer rate is just high enough to keep the vortex sheets short and stable until the plate reaches a high angle of attack. As with the $K = 0.7$ case, we see in Figure 3.16 that the hybrid model also predicts periodic bluff-body shedding for the $K = 0.2$ case. Figure 3.15 shows a comparison of the lift and drag coefficients as the plate is pitching up.

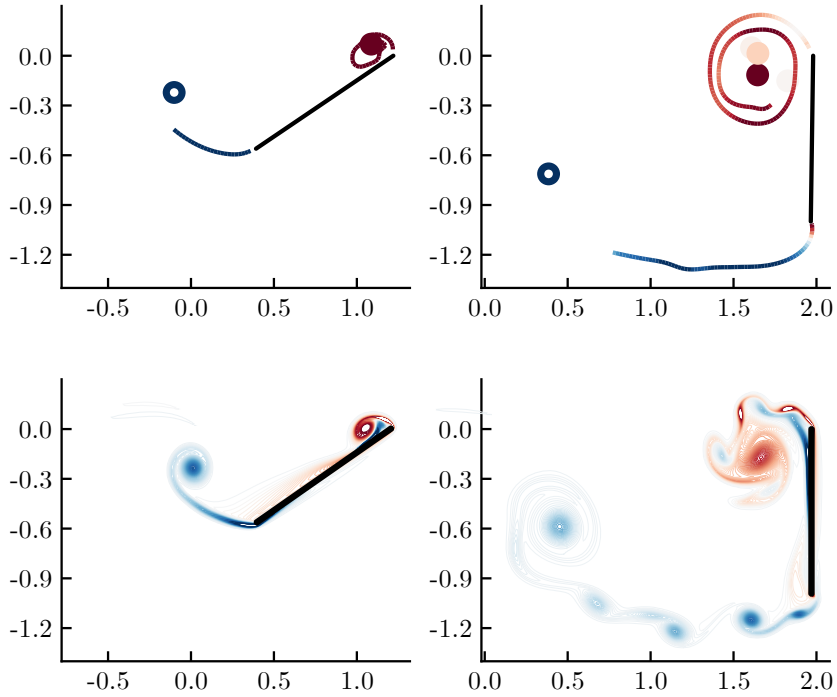

Figure 3.11: Circulation distribution predicted by **(top)** the hybrid model with $\Delta t_{\text{max}} = 0.1c/U$ and **(bottom)** a vortex sheet model for a pitching plate with $K = 0.7$ at $\alpha = 33°$ **(left)**, $\alpha = 90°$ **(right)**.

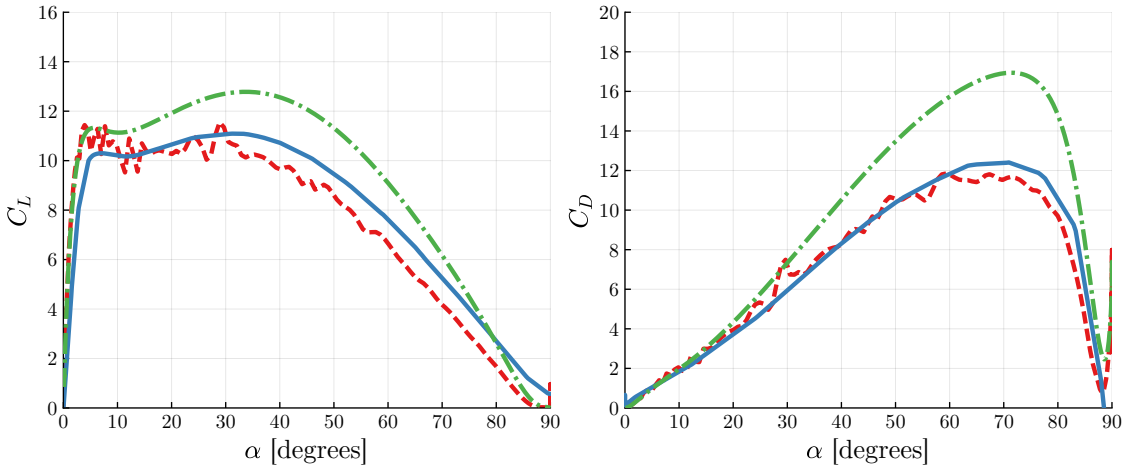

Figure 3.12: Lift and drag coefficients for a pitch-up maneuver at $K = 0.7$. Early-time lift **(left)** and drag **(right)** coefficients for a pitch-up maneuver at $K = 0.7$ predicted by the hybrid model with $U\Delta t_{\text{min}}/c = 0.1$ **(– –)**, the Wang and Eldredge model **(–·–)**, and CFD results as $\text{Re} = 500$ **(——)**.

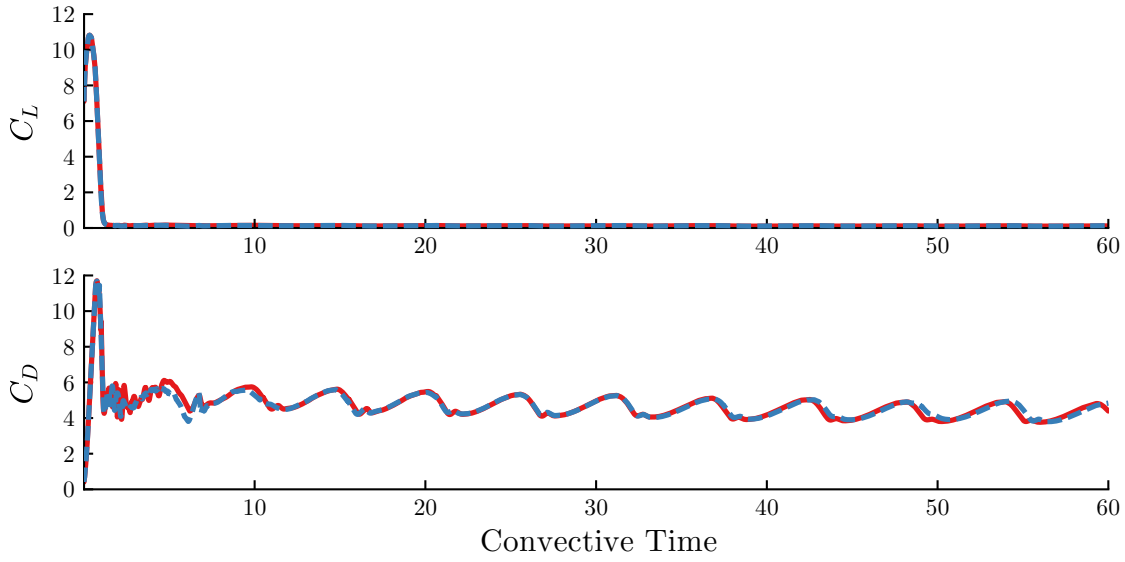

Figure 3.13: Comparison of the long term lift and drag coefficients for a pitch-up maneuver at $K = 0.7$ predicted with $U\Delta t_{\text{min}}/c = 0.1$ **(—)** $U\Delta t_{\text{min}}/c = 0.2$ **(- -)**

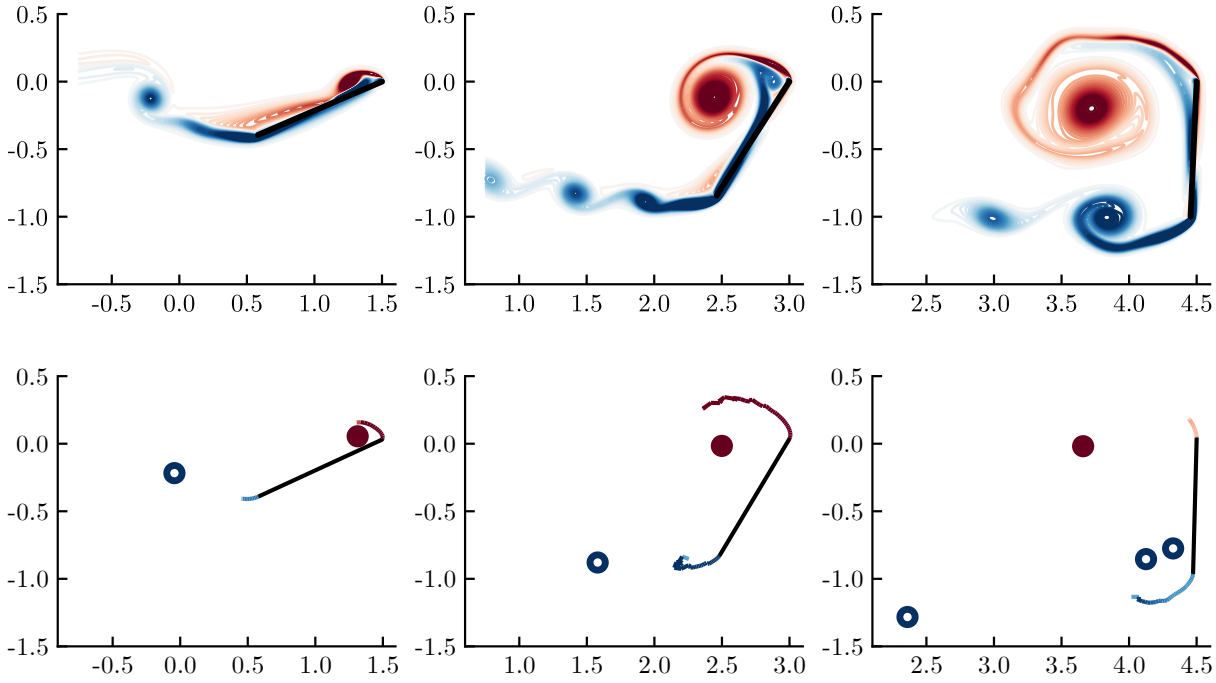

Figure 3.14: Circulation distribution predicted by the hybrid model with $\Delta t_{\text{max}} = 0.2c/U$ for a pitching plate with $K = 0.2$ at $\alpha = 23°$ **(left)**, $\alpha = 57°$ **(center)**, $\alpha = 87°$ **(right)**.

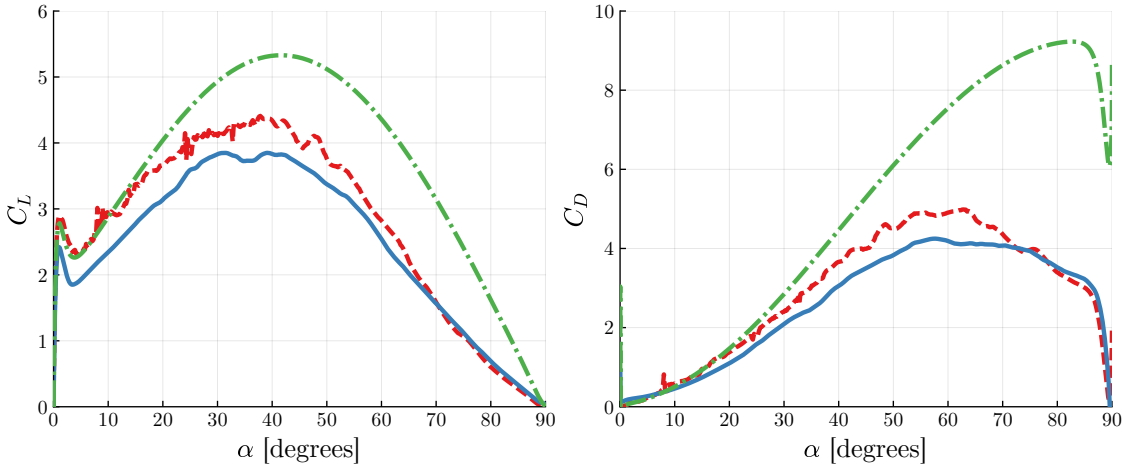

Figure 3.15: Lift and drag coefficients for a pitch-up maneuver at $K = 0.2$. Early-time lift **(left)** and drag **(right)** coefficients for a pitch-up maneuver at $K = 0.2$ predicted by the hybrid model with $U\Delta t_{\text{min}}/c = 0.2$ **(- -)**, the Wang and Eldredge model **(-·-·-)**, and CFD results as $\text{Re} = 500$ **(——)**.

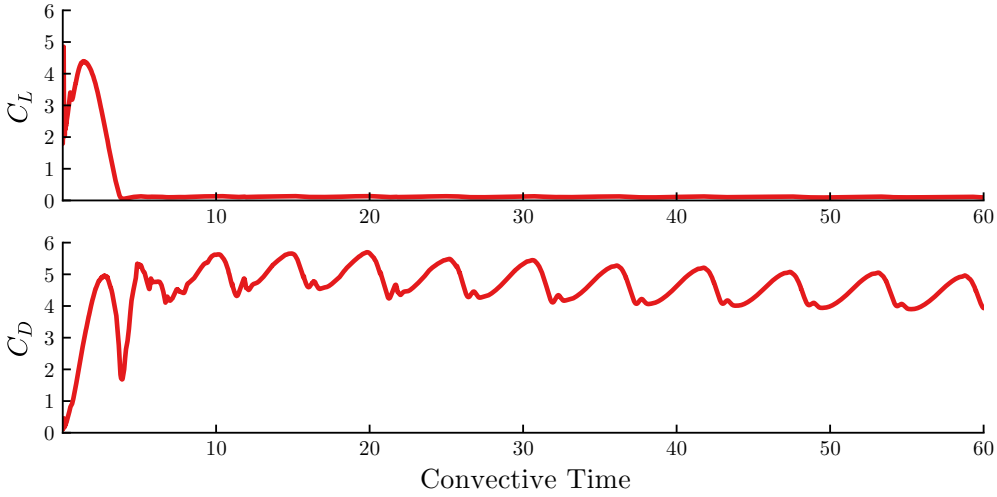

Figure 3.16: Long term lift and drag coefficients for a pitch-up maneuver at $K = 0.2$ predicted by the hybrid model with $\Delta t_{\text{max}} = 0.2c/U$.

Chapter 4

Data Assimilation

A key open problem in vortex modeling is determining how much vorticity to release from the leading edge. While it is generally accepted that the Kutta condition is a valid vortex shedding criterion to use at the trailing edge, its use at the leading edge in numerous vortex models [5, 26, 59, 7] is mainly due to the lack of better criteria. This has driven the exploration of data-assisted leading edge shedding criteria. In a discrete vortex model developed by Katz [28], leading edge shedding was tuned with a handful of parameters. Some parameters, such as the position of the leading edge separation point, were chosen based on experimental data, while others were adjusted to bring the predicted force closer to the measured force. In more recent work, Ramesh and Gopalarathnam [47] introduced a shedding criterion based on the observation that real airfoils can support a critical level of suction around the leading edge before flow separation is triggered. Correspondingly, the authors suggested the use of the leading edge suction parameter (LESP), a measure of the leading edge suction peak, to govern vortex shedding. In their model, when the LESP is below a critical value, which we will denote as LESP_c, no vorticity is released. However, when the instantaneous LESP exceeds LESP_c, vortex particles will be released with the appropriate amount of strength to bring the LESP down to LESP_c. By tuning their discrete vortex model with an empirically determined LESP_c, the authors were able to predict lift responses that were in good agreement with experimental results. However, since the model was statically tuned, it had some difficulty handling real-time perturbations to the flow, such as gusts or freestream disturbances.

Hemati, Eldredge, and Speyer [22] took another approach and explored the problem from an optimal control perspective. The leading and trailing edge vorticity fluxes were interpreted as inputs to a nonlinear dynamical system. They then used variational methods to find the time history of the leading and trailing edge vorticity fluxes that would minimize the squared error between the empirically measured and model-predicted forces. While this optimization technique produces good results, it requires the measurements to be available over the entire optimization window. So while it is a useful post-processing tool, it is also not directly applicable for real-time estimation.

In this chapter we adapt both the work of Hemati, Eldredge, and Speyer and Ramesh and Gopalarathnam so that they can better assimilate data in real time. In Section 4.1, we build upon the work of Hemati, Eldredge, and Speyer by presenting a "bootstrapping" procedure, wherein previously optimized results are used to predict the vorticity fluxes in a short, appended window. The new vorticity flux trajectory is then optimized to match the empirical force over the appended window. This predictor-corrector cycle can be pushed forward in time as force data becomes available. In Section 4.2, we first augment the discrete vortex model introduced by Ramesh and Gopalarathnam with the impulse-matching circulation transfer method presented in the previous chapter. This prevents the dimensionality of the model from increasing continuously, which then allows us to further enhance the model using the ensemble Kalman filter.

4.1 Bootstrapped Optimization Framework

As our current work builds from the model optimization framework by Hemati, Eldredge, and Speyer, we will briefly summarize the procedure here. Let us define the system state $\boldsymbol{z}$ as the vector containing the positions $\boldsymbol{x}$ and strengths $\boldsymbol{\Gamma}$ of the point vortices

$$\boldsymbol{z} \equiv \begin{pmatrix} \boldsymbol{x} \\ \boldsymbol{\Gamma} \end{pmatrix}. \tag{4.1}$$

For example, in a two-vortex model, $\boldsymbol{z} \in \mathbb{R}^6$. Given a sequence of the rate of change of the vortex strengths $\dot{\boldsymbol{\Gamma}}(t)$ and an initial state $\boldsymbol{z_0}$, the vortex model predicts the history of the force applied on the plate, $\boldsymbol{F}[\boldsymbol{z}(t), \dot{\boldsymbol{\Gamma}}(t), t]$. This force history, in general, will differ from the force measured empirically, $\boldsymbol{F}^{\text{emp}}(t)$. We seek an optimal $\dot{\boldsymbol{\Gamma}}(t)$ trajectory within a time interval $[t_0, t_f]$ that minimizes the cost function

$$J = \int_{t_0}^{t_f} \left\| \boldsymbol{F}[\boldsymbol{z}(t), \dot{\boldsymbol{\Gamma}}(t), t] - \boldsymbol{F}^{\text{emp}}(t) \right\|^2 \mathrm{d}t \tag{4.2}$$

with the constraint that the vortices follow an evolution equation

$$\dot{\boldsymbol{z}} = \boldsymbol{f}(\boldsymbol{z}, \dot{\boldsymbol{\Gamma}}, t). \tag{4.3}$$

This constrained minimization problem can be solved by defining, then minimizing the Hamiltonian $\mathcal{H}$

$$\mathcal{H} = g(\boldsymbol{z}, \dot{\boldsymbol{\Gamma}}, t) + \boldsymbol{p}(\boldsymbol{z}, \dot{\boldsymbol{\Gamma}}, t)^\top \boldsymbol{f}(\boldsymbol{z}, \dot{\boldsymbol{\Gamma}}, t) \tag{4.4}$$

where

$$g(\boldsymbol{z}, \dot{\boldsymbol{\Gamma}}, t) \equiv \left\| \boldsymbol{F}[\boldsymbol{z}(t), \dot{\boldsymbol{\Gamma}}(t), t] - \boldsymbol{F}^{\text{emp}}(t) \right\|^2 \tag{4.5}$$

and $\boldsymbol{p}$ is the costate of the system, essentially Lagrange multipliers that are used to enforce the constraint of the evolution equation.

Starting from an initial guess of $\dot{\boldsymbol{\Gamma}}^0(t)$, each iteration of the optimization goes through the following steps:

1. Integrate vortex positions and strengths forward in time

$$\boldsymbol{z}(t) = \boldsymbol{z}_0 + \int_{t_0}^{t} \boldsymbol{f}(\boldsymbol{z}, \dot{\boldsymbol{\Gamma}}, t)\mathrm{d}t$$

2. Integrate the costate backward in time

$$\begin{aligned}\boldsymbol{p}(t) &= \int_{t_f}^{t} \dot{\boldsymbol{p}} \mathrm{d}t \\ &= \int_{t_f}^{t} \left[-\frac{\partial g}{\partial \boldsymbol{z}} - \frac{\partial \boldsymbol{f}}{\partial \boldsymbol{z}}^{\top} \boldsymbol{p} \right] \mathrm{d}t\end{aligned}$$

3. Compute the gradient of the Hamiltonian

$$\frac{\partial \mathcal{H}}{\partial \dot{\boldsymbol{\Gamma}}} = \frac{\partial g}{\partial \dot{\boldsymbol{\Gamma}}} + \frac{\partial \boldsymbol{f}}{\partial \dot{\boldsymbol{\Gamma}}}^{\top} \boldsymbol{p}$$

4. Update $\dot{\boldsymbol{\Gamma}}(t)$

$$\dot{\boldsymbol{\Gamma}}^{k+1} = \dot{\boldsymbol{\Gamma}}^{k} - \alpha \frac{\partial \mathcal{H}}{\partial \dot{\boldsymbol{\Gamma}}}$$

   where α is found using a method such as the non-linear conjugate gradient method.

These four steps are repeated until the norm of the gradient is smaller than the desired tolerance.

In Figure 4.1 we show some results of applying this optimization procedure on the Wang and Eldredge variable-strength point vortex model for a pitch-up maneuver. The unoptimized force response predicted by the Wang and Eldredge model are shown with dashed blue lines, the results from a high-fidelity viscous simulation are shown with solid red lines, while the optimized results are shown with dot-dashed green lines. The top row of Figure 4.1 shows the progress of the optimization after 30 iterations, while the bottom row shows the progress after 1000 iterations. While the optimized results are visually indistinguishable from the high-fidelity simulation results, they rely on existing force or velocity field data for prescribed maneuvers, which may not always be available. In the next section, we present a "bootstrapping" procedure that can be used to adapt the optimization framework for real-time uses.

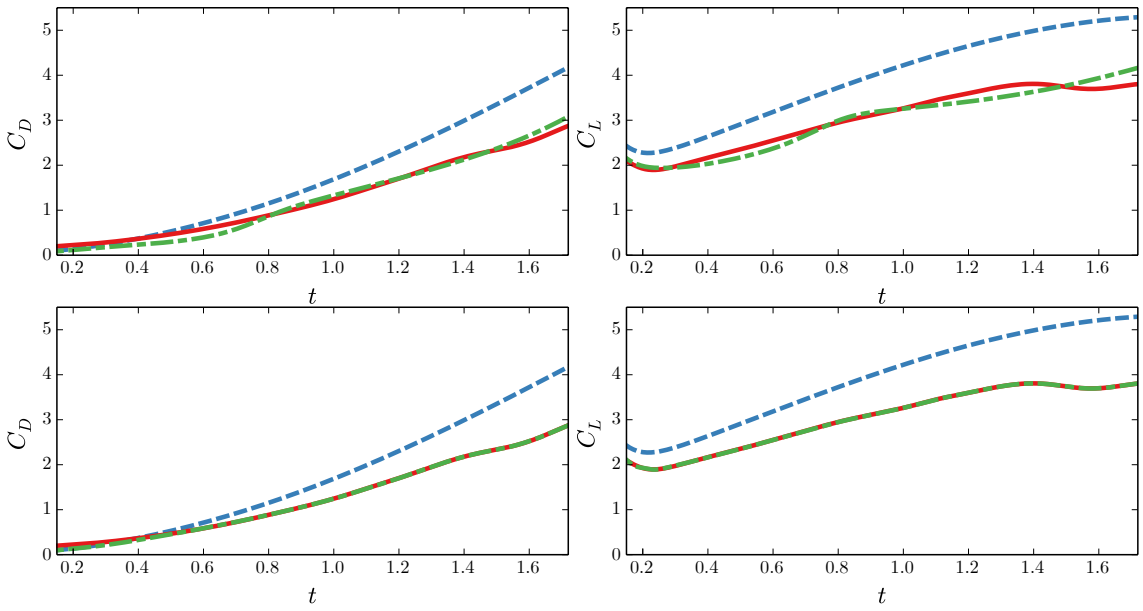

Figure 4.1: Comparison of model predicted forces (Wang and Eldredge [59] – – , Hemati, Eldredge, and Speyer [22] –·–·–) and forces predicted by high-fidelity simulations **(——)** for a pitch-up maneuver. (Left) Coefficient of drag. (Right) Coefficient of lift. (Top) 30 optimization iterations. (Bottom) 1000 optimization iterations.

4.1.1 Model Formulation

Suppose we know the *optimal* amount of vorticity to transfer from the plate into the fluid, $\dot{\boldsymbol{\Gamma}}^{\text{opt}}$, within a starting time window $[t_-, t_f]$, i.e. $\dot{\boldsymbol{\Gamma}}$ minimizes the difference between the predicted and measured force. We would like to use the information in $[t_-, t_f]$ to predict an appropriate vorticity flux for $t > t_f$. Since the kinematics of the plate can be arbitrary, and $\dot{\boldsymbol{\Gamma}}$ is nonlinearly dependent on them, a simple linear extrapolation of the optimized $\dot{\boldsymbol{\Gamma}}^{\text{opt}}$ will not yield an accurate prediction. In order to utilize the convenience and speed of a linear operation but still retain nonlinear dependencies, we can represent the relationship between the vortex strengths and plate kinematics as a linear combination of nonlinear basis functions. Though these basis functions can likely be determined by a more sophisticated identification procedure, here we present a simple approach based on an extension

of the Kutta condition.

The Kutta condition can be stated as an implicit relationship between vortex position, vortex strength, and the kinematics of the plate

$$\boldsymbol{k}(\boldsymbol{x}, \boldsymbol{\Gamma}, t) = 0.$$

In order to use it in an evolution equation, it is more convenient to express it in its time derivative form

$$\frac{\partial \boldsymbol{k}}{\partial \boldsymbol{x}} \cdot \dot{\boldsymbol{x}} + \frac{\partial \boldsymbol{k}}{\partial \boldsymbol{\Gamma}} \cdot \dot{\boldsymbol{\Gamma}} + \frac{\partial \boldsymbol{k}}{\partial t} = \boldsymbol{0}. \tag{4.6}$$

Note that because the number of variable-strength vortices is equal to the number of salient edges, $\dim(\boldsymbol{k}) = \dim(\boldsymbol{\Gamma})$, so the matrix $\partial \boldsymbol{k}/\partial \boldsymbol{\Gamma}$ is square; it is also generally invertible. If we define

$$\begin{aligned}
\boldsymbol{Y} &\equiv \frac{\partial \boldsymbol{k}}{\partial \boldsymbol{\Gamma}} \cdot \dot{\boldsymbol{\Gamma}} \\
\boldsymbol{X} &\equiv \frac{\partial \boldsymbol{k}}{\partial \boldsymbol{x}} \cdot \dot{\boldsymbol{x}} \\
\boldsymbol{U} &\equiv \frac{\partial \boldsymbol{k}}{\partial t}
\end{aligned}$$

then we can write the previous system Equation (4.6) as

$$\boldsymbol{Y} = -\begin{pmatrix} \boldsymbol{I_X} & \boldsymbol{I_U} \end{pmatrix} \begin{pmatrix} \boldsymbol{X} \\ \boldsymbol{U} \end{pmatrix} \tag{4.7}$$

where $\boldsymbol{I_X}$ and $\boldsymbol{I_U}$ are identity matrices, both of size 2×2 for a two-dimensional plate with two salient edges.

The Kutta condition is not enforced in the optimized model. However, the Kutta condition embodies important nonlinear relationships that can be used as the basis for a pre-

dictor model for $\dot{\mathbf{\Gamma}}$. Let us therefore generalize Equation (4.7) in the form

$$\boldsymbol{Y} = -\begin{pmatrix} \boldsymbol{A} & \boldsymbol{B} \end{pmatrix} \begin{pmatrix} \boldsymbol{X} \\ \boldsymbol{U} \end{pmatrix}.$$

The matrices $\boldsymbol{A}$ and $\boldsymbol{B}$ are of the same size as the identity matrices in Equation (4.7), but contain unknown coefficients here. We can determine these coefficients from the following:

$$\begin{pmatrix} \boldsymbol{A} & \boldsymbol{B} \end{pmatrix} \equiv \begin{pmatrix} \boldsymbol{Y_1} & \boldsymbol{Y_2} & \cdots & \boldsymbol{Y_k} \end{pmatrix} \begin{pmatrix} \boldsymbol{X_1} & \boldsymbol{X_2} & \cdots & \boldsymbol{X_k} \\ \boldsymbol{U_1} & \boldsymbol{U_2} & \cdots & \boldsymbol{U_k} \end{pmatrix}^{\dagger} \tag{4.8}$$

where † denotes the Moore-Penrose pseudo-inverse, and the subscripts $1, 2, \cdots, k$ denote sequential time-steps up to some length k. This definition gives us a least squares approximation of the relationship between $\boldsymbol{X}$, $\boldsymbol{U}$, and $\boldsymbol{Y}$. That is, $\begin{pmatrix} \boldsymbol{A} & \boldsymbol{B} \end{pmatrix}$ determined from Equation (4.8) minimizes

$$\left\| \begin{pmatrix} \boldsymbol{Y_1} & \boldsymbol{Y_2} & \cdots & \boldsymbol{Y_k} \end{pmatrix} - \begin{pmatrix} \boldsymbol{A} & \boldsymbol{B} \end{pmatrix} \begin{pmatrix} \boldsymbol{X_1} & \boldsymbol{X_2} & \cdots & \boldsymbol{X_k} \\ \boldsymbol{U_1} & \boldsymbol{U_2} & \cdots & \boldsymbol{U_k} \end{pmatrix} \right\|^2$$

Thus, we obtain an explicit equation for the rates of change of vortex strengths

$$\dot{\mathbf{\Gamma}} = \left(\frac{\partial \boldsymbol{k}}{\partial \mathbf{\Gamma}} \right)^{-1} \left(\boldsymbol{A} \frac{\partial \boldsymbol{k}}{\partial \boldsymbol{x}} \dot{\boldsymbol{x}} + \boldsymbol{B} \frac{\partial \boldsymbol{k}}{\partial t} \right). \tag{4.9}$$

As a linear approximation, Equation (4.9) may only be accurate for a small window extending beyond the range $[t_1, t_k]$. However, this allows us to generate plausible values of $\dot{\mathbf{\Gamma}}$ beyond the original optimization window using the following procedure:

1. Use the optimization procedure described in Hemati et al. to obtain an initial trajectory of optimized $\dot{\mathbf{\Gamma}}(t)$ in some time interval $[t_0, t_f]$. Set this initial window as the *current optimization window*.

2. Pick a time interval near the end of the current optimization window $[t^-, t_f]$, $t^- > t_0$ (colored in gray in any of the plots of Figures 4.2 and 4.3)

3. Compute $\begin{pmatrix} \boldsymbol{A} & \boldsymbol{B} \end{pmatrix}$ using optimized results in the interval $[t^-, t_f]$.

4. *Prediction:* Generate a new sequence $\dot{\boldsymbol{\Gamma}}(t)$ using equation for an appended time window $[t_f, t^+]$, $t^+ > t_f$.

5. *Correction:* Apply the optimization procedure over the current optimization window.

6. Set the appended time interval as the current optimization window, $[t_0, t_f] = [t_f, t^+]$, with an associated interval $[t^-, t_f]$, $t^- > t_0$, and return to step 3.

4.1.2 Results

We apply this bootstrapping process to the case of a rapid pitch-up maneuver of a two-dimensional plate with chord length c in a free stream U_∞. The motion starts at 0° angle of attack and continues to 45° at a dimensionless pitch rate of $K = 0.2$. The high-fidelity simulation data used to drive the optimization procedure assumes a viscous fluid with a Reynolds number of $\mathrm{Re} = U_\infty c/\nu = 1000$ and a plate thickness of $0.023c$. For the model, we used the Wang and Eldredge variable-strength point vortex model.

Figure 4.2 and Figure 4.3 demonstrate the procedure in two example time windows, labeled as (i) and (ii), respectively. The top row of Figure shows the result of an initial optimization over the interval $t \in [0.1, 0.87]$ using the original model optimization method of Hemati et al. We computed $(\boldsymbol{A}\ \boldsymbol{B})$ using the optimized results in the interval $t \in [0.77, 0.87]$ (shaded in gray), and predicted the rates of change of vortex strengths in $t \in [0.87, 1.0]$, leading to the associated force components depicted in cyan in the middle row. The slight difference between the empirical force and the predicted force was corrected by performing only 5 iterations of optimization over the small prediction window.

The optimized results in the appended region are shown in the bottom row of Figure 4.2.

Figure 4.3 shows the same bootstrapping process applied in a later window, $t \in [1.30, 1.50]$. It is clear that within this time window the force is nonlinearly dependent on time. However, the prediction was able to qualitatively capture the nonlinearity with constant values for $(\boldsymbol{A}\ \boldsymbol{B})$.

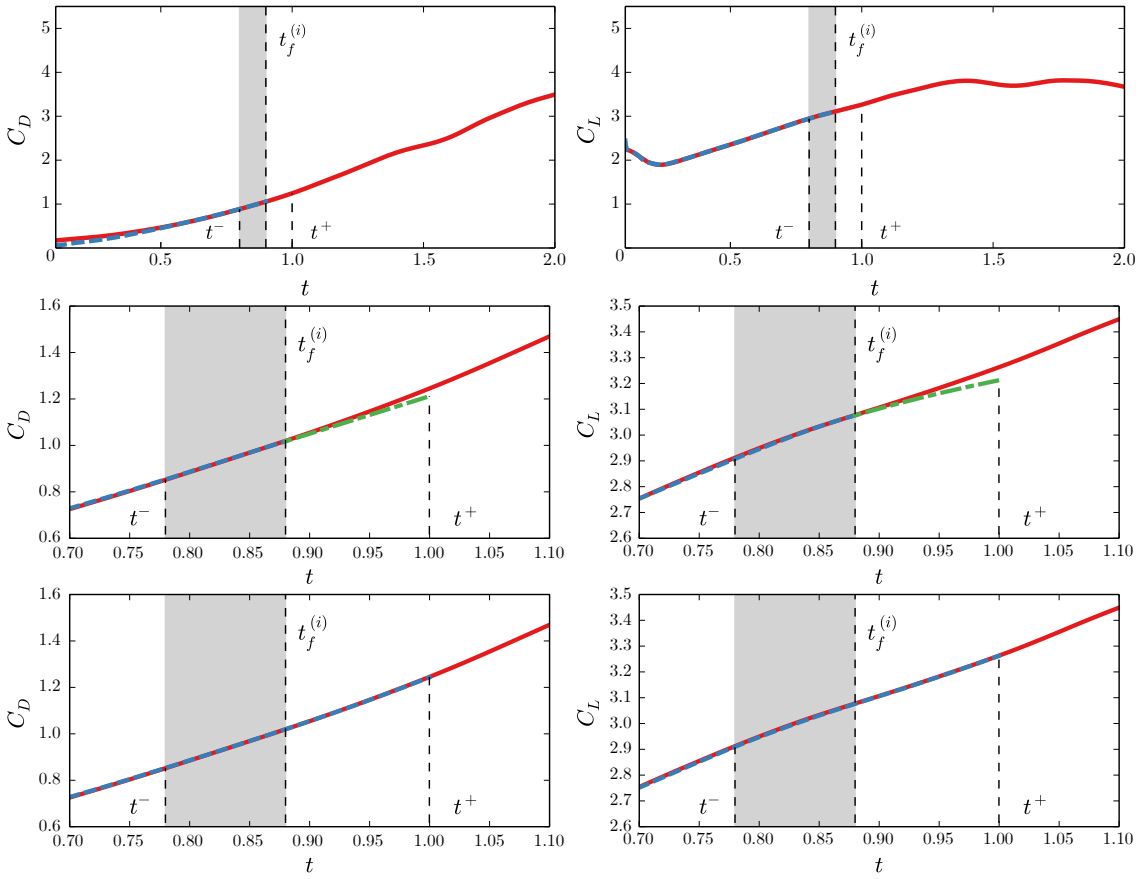

Figure 4.2: Applying the bootstrapping procedure around $t_f^{(i)} = 0.87$. The gray portions bounded by the dashed lines t^- and $t_f^{(i)}$ are used to generate predictions for the time interval $[t_f^{(i)}, t^+]$ (Top) Comparison between force predicted high-fidelity simulation **(—)**, and optimization up to time $t_f^{(i)}$ **(– –)** (Middle) Predicted force **(–·–)** using previously optimized results in the shaded interval. (Bottom) Corrected force in the appended region after 5 iterations of optimization

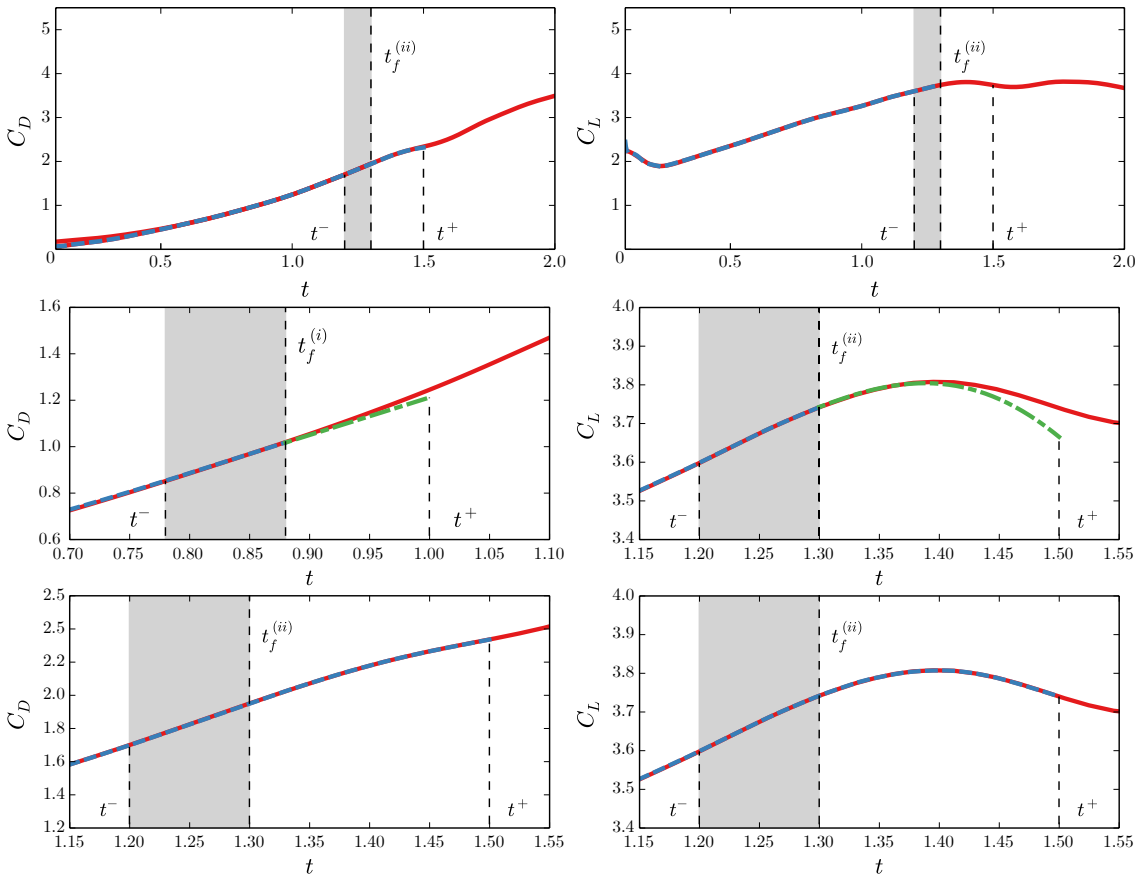

Figure 4.3: Applying the bootstrapping procedure around $t_f^{(ii)} = 1.30$. The gray portions bounded by the dashed lines t^- and $t_f^{(i)}$ are used to generate predictions for the time interval $[t_f^{(i)}, t^+]$ (Top) Comparison between force predicted high-fidelity simulation **(—)**, and optimization up to time $t_f^{(i)}$ **(– –)** (Middle) Predicted force **(-·-·-)** using previously optimized results in the shaded interval. (Bottom) Corrected force in the appended region after 5 iterations of optimization

4.2 Ensemble Kalman Filter Approach

In this section, we present our enhancement to the discrete vortex model introduced by Ramesh and Gopalarathnam [47]. First, let us consider some motivating examples. In Figure 4.4, we show the vorticity distributions predicted by a LESP-based vortex blob model of a plate that is impulsively translated at 20°. In the top plot, $\text{LESP}_c = 3.0$. This

means that in order for the model to release any leading edge vorticity, we must have a large leading edge suction. Or equivalently, the model assumes that the plate can support a large amount of suction around the leading edge. In the middle plot, $\text{LESP}_c = 0.3$. Here, we see that the model predicts the formation of a coherent LEV. Finally, in the lower plot of Figure 4.4, where $\text{LESP}_c = 0.8$, we see a weak LEV.

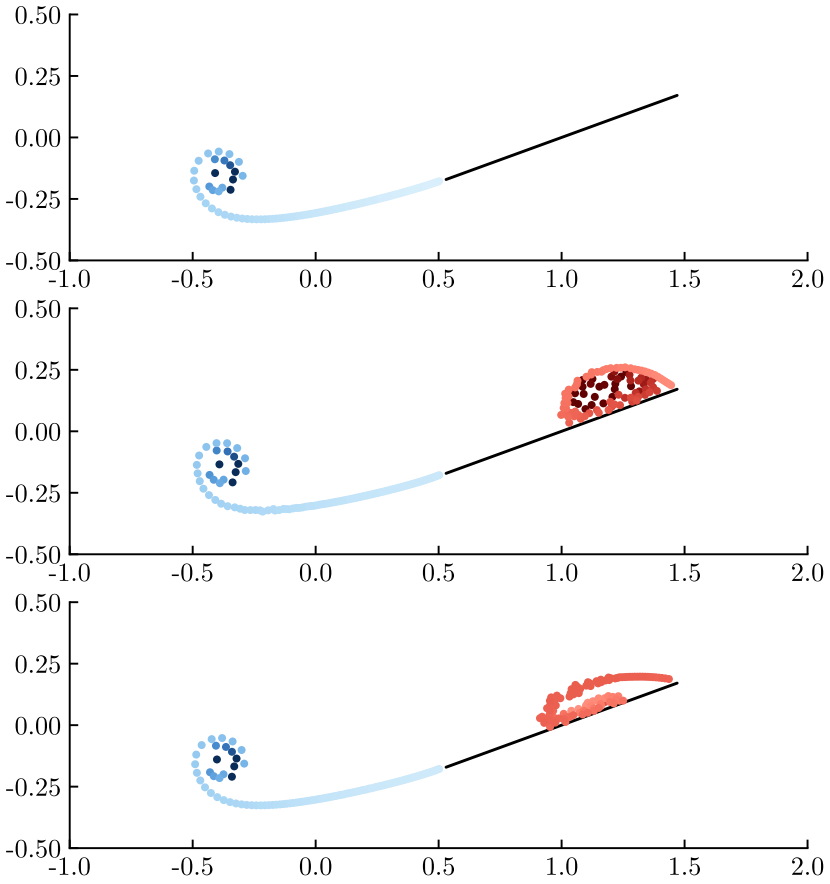

Figure 4.4: Comparison of vorticity distributions predicted by a vortex blob model after one convective time with $\text{LESP}_c = 3.0$ **(top)**, $\text{LESP}_c = 0.3$ **(middle)**, and $\text{LESP}_c = 0.8$ **(bottom)**.

In Figure 4.5, we show the corresponding pressure distributions, where the top of each plot corresponds to the leading edge, the bottom corresponds to the trailing edge, and time increases in the x-direction. In the middle plot, we can clearly see the growth of a negative pressure region as it propagates down the chord. This corresponds to the development of

a strong LEV. In contrast, we see from the top plot that there is no clear LEV, and the low pressure at the leading edge comes simply from the high LESP value.

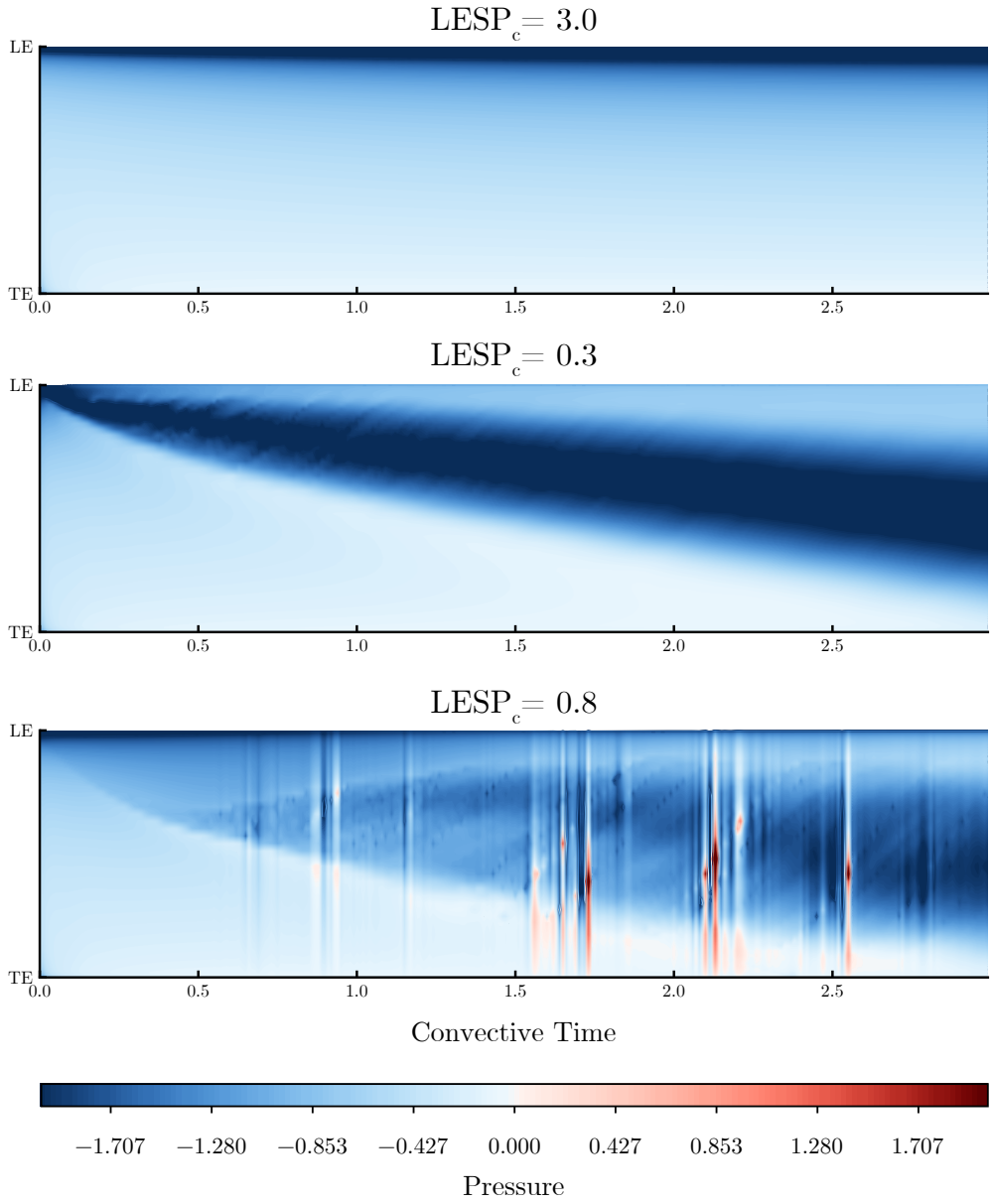

Figure 4.5: Comparison of pressure distributions across the plate predicted by a vortex blob model with LESP$_c = 3.0$ **(top)**, LESP$_c = 0.3$ **(middle)**, and LESP$_c = 0.8$ **(bottom)**.

The relationship between the critical LESP value and the pressure distribution suggests that there may be a way we can estimate LESP$_c$ if we are given the surface pressure information. Even more importantly, we see that surface pressure measurements may be

used to directly augment missing parameters in our model.

4.2.1 Data Assimilation through Kalman Filters

We will use the Ensemble Kalman filter (EnKF) to assimilate pressure data into the vortex model. The EnKF was originally introduced to handle the high-dimensional nonlinear dynamics found in meteorology [17]. Before describing how we can use it to augment a vortex model, we first give an overview of the standard Kalman filter.

4.2.2 Review of The Kalman Filter

In systems with noise, we usually do not know our state exactly so we have to treat the *true* state $\boldsymbol{x}$ as being drawn from a multivariate random variable $\mathbf{X}$. From the distribution of $\mathbf{X}$, we can come up with a "best guess" for the true state, which we will denote by $\hat{\boldsymbol{x}}$. Let us consider a discrete-time linear system where the state transition matrix at the k-th time step is denoted as $\boldsymbol{\Phi}_k$. We will assume that our measurements, $\boldsymbol{z}_k$, are linear combinations of the state and are determined using the linear operator $\boldsymbol{H}_k$. To account for random disturbances and modeling errors, we further assume that at every time-step, both our system and our measurements are corrupted by additive noise. So, the governing equations for our *true* state and measurements are

$$\boldsymbol{x}_k = \boldsymbol{\Phi}_k \boldsymbol{x}_{k-1} + \boldsymbol{w}_k \tag{4.10}$$

and

$$\boldsymbol{z}_k = \boldsymbol{H}_k \boldsymbol{x}_k + \boldsymbol{v}_k \tag{4.11}$$

where $\boldsymbol{w}_k$ and $\boldsymbol{v}_k$ are the the unknown perturbations to the state and measurements at time step k, respectively. However, as we do not ever know what the true state is, our *model* should be given by the following set of stochastic difference equations

$$\mathbf{X}_k = \mathbf{\Phi}_k \mathbf{X}_{k-1} + \mathbf{W}_k \tag{4.12}$$

and

$$\mathbf{Z}_k = \boldsymbol{H}_k \boldsymbol{x}_k + \mathbf{V}_k, \tag{4.13}$$

where the change in font indicates that $\mathbf{X}_k$, $\mathbf{Z}_k$, $\mathbf{W}_k$, and $\mathbf{V}_k$ are multivariate random variables. Writing the equations in terms of random variables emphasizes the fact that our estimate for the new state is corrupted by both noise and the fact that we not have full information about the previous state. This is in contrast to our measurements, which *always* measure the true state and are only corrupted by noise[1]. To further simplify the problem, we assume that the distributions of the initial state, $\mathbf{X}_0$, the state disturbances, $\mathbf{W}_k$, and the measurement noise, $\mathbf{V}_k$ are all normally distributed

$$\mathbf{X}_0 = \mathcal{N}\left(\hat{\boldsymbol{x}}_0,\, \boldsymbol{P}_0\right) \tag{4.14}$$

$$\mathbf{W}_k = \mathcal{N}\left(0,\, \boldsymbol{W}_k\right) \tag{4.15}$$

$$\mathbf{V}_k = \mathcal{N}\left(0,\, \boldsymbol{V}_k\right) \tag{4.16}$$

where we use the $\mathcal{N}\left(\mu,\, C\right)$ to denote a Gaussian distribution with mean μ and variance C, and $\boldsymbol{P}_0$, $\boldsymbol{W}_k$, and $\boldsymbol{V}_k$ are the covariance matrices for the state, state disturbance, and measurement noise, respectively. In addition, $\mathbf{X}_0$, $\mathbf{W}_1, \cdots, \mathbf{W}_k$, and $\mathbf{V}_1, \cdots, \mathbf{V}_k$ are independent for all k. Under this myriad of assumptions[2], it can be shown that the Kalman filter

[1] This may seem like a superfluous point with unnecessary extra notation, but this subtle distinction was what the author struggled with when first learning the Kalman filter

[2] In the original derivation by Kalman, the Gaussian assumption for the state disturbance and measurement noise is relaxed, and they are only restricted to be zero-mean and delta-correlated random processes[52].

recursively combines knowledge about the underlying system with new measurements to give a prediction that minimizes the uncertainty, maximizes the likelihood, minimizes the least square difference between the expect measurement and actual measurement, and is optimal with "virtually any reasonable [definition of] 'optimal' "[40]. We will outline its basic workings below.

At the first time step, our best estimate of the state is simply $\hat{\boldsymbol{x}}_0$ with uncertainty $\boldsymbol{P}_0$. Since this initial state is a Gaussian random variable, and our system (Equation (4.12)) is linear with additive Gaussian noise (which makes it a Gauss-Markov process), we know that $\mathbf{X}_k$ is Gaussian for all k. Now suppose the optimal estimate at time step $k-1$ is given by mean $\hat{\boldsymbol{x}}_{k-1}$ and covariance $\boldsymbol{P}_{k-1}$. Before we obtain any measurements, the optimal estimate of the state of our system at time step k is computed using our knowledge of the system dynamics $\boldsymbol{\Phi}_k$ and $\boldsymbol{W}_k$. Since the state equation, Equation (4.10), is an affine linear equation, we can propagate the mean and covariance of our estimate through

$$\hat{\boldsymbol{x}}_k^- = \boldsymbol{\Phi}_k \hat{\boldsymbol{x}}_{k-1} \tag{4.17}$$

and

$$\boldsymbol{P}_k^- = \boldsymbol{\Phi}_k \boldsymbol{P}_{k-1} \boldsymbol{\Phi}_k^T + \boldsymbol{W}_k, \tag{4.18}$$

where the superscript "$-$" indicates that these estimates are made without the help of measurements. Moreover, since the mean and covariance completely specify a Gaussian distribution, the new state distribution is given by

$$\mathbf{X}_k^- = \mathcal{N}\left(\hat{\boldsymbol{x}}_k^-,\, \boldsymbol{P}_k^-\right). \tag{4.19}$$

As we have no other information at this point, $\hat{\boldsymbol{x}}_k^-$ is also the optimal estimate with uncertainty $\boldsymbol{P}_k^-$, i.e. $\mathbf{X}_k = \mathbf{X}_k^-$.

Now suppose we obtain a measurement of the true state through $\boldsymbol{z}_k$. This new infor-

mation allows us to form a better estimate for the distribution of the state by conditioning on even that the measurement drawn from $\mathbf{Z}_k = \mathcal{N}(\boldsymbol{H}_k \boldsymbol{x}_k, \boldsymbol{V}_k)$ took on the value $\boldsymbol{z}_k$. We denote this conditioned random variable as

$$\mathbf{X}_k^+ := \mathbf{X}_k^- \,|\, (\mathbf{Z}_k = \boldsymbol{z}_k)\,, \tag{4.20}$$

where the superscript "+" indicates that a measurement has been assimilated. This conditional random variable can be shown to be Gaussian, with mean and covariance given by

$$E\left[\mathbf{X}_k^+\right] = \hat{\boldsymbol{x}}_k^- + \underbrace{\boldsymbol{P}_k^- \boldsymbol{H}_k^T \left(\boldsymbol{V}_k + \boldsymbol{H}_k \boldsymbol{P}_k^- \boldsymbol{H}_k^T\right)^{-1}}_{\boldsymbol{K}_k} \underbrace{\left(\boldsymbol{z}_k - \boldsymbol{H}_k \hat{\boldsymbol{x}}_k^-\right)}_{\boldsymbol{y}_k} \tag{4.21}$$

and

$$\operatorname{cov}\left(\mathbf{X}_k^+\right) = \boldsymbol{P}_k^- - \boldsymbol{K}_k \left(\boldsymbol{V}_k + \boldsymbol{H}_k \boldsymbol{P}_k^- \boldsymbol{H}_k^T\right) \boldsymbol{K}_k^T \tag{4.22}$$

where $\boldsymbol{K}$ is called the Kalman gain, and $\boldsymbol{y}$, the difference between the actual measurement and expected measurement, is called the innovation. If we take this conditional mean and variance as our newest "best estimate" and its uncertainty, i.e.

$$\begin{aligned} \hat{\boldsymbol{x}}_k &:= E\left[\mathbf{X}_k^+\right] \\ \boldsymbol{P}_k &:= \operatorname{cov}\left(\mathbf{X}_k^+\right), \end{aligned}$$

then we can fulfill all the optimality conditions mentioned above. Now we can compute optimal estimates of our state for all time.

The provable optimality of the Kalman filter, as well as its ease of implementation (specified completely by Equations (4.17), (4.18), (4.21) and (4.22)), has made it widely adopted across many field and industries. However, as we have mentioned in all preceding chapters, we are interested in capturing the *nonlinear* effects of unsteady aerodynamics. Fortunately, there are several extensions to the Kalman filter for nonlinear systems, in

which the true state and measurements are evolved according to

$$\boldsymbol{x}_k = \boldsymbol{f}_k(\boldsymbol{x}_{k-1}) + \boldsymbol{w}_k, \tag{4.23}$$

and

$$\boldsymbol{z}_k = \boldsymbol{h}_k(\boldsymbol{x}_k) + \boldsymbol{v}_k, \tag{4.24}$$

where $\boldsymbol{f}_k$ and $\boldsymbol{h}_k$ are a nonlinear functions. The most common extension to handle such systems is the extended Kalman filter (EKF). The EKF uses a first-order Taylor expansion of $\boldsymbol{f}_k$ and $\boldsymbol{h}_k$ to propagate the estimate covariance and compute the Kalman gain. This means that it requires explicit expressions for the Jacobians $\frac{\partial \boldsymbol{f}_k}{\partial \boldsymbol{x}}$ and $\frac{\partial \boldsymbol{h}_k}{\partial \boldsymbol{x}}$, which may not be readily available. Moreover, the linearization can lead to unstable growth of the error covariance. While this can be solved by using higher-order derivatives, the number of terms in the higher-order Taylor expansion grows exponentially, which can make the computation prohibitively expensive for real-time applications. Another popular variant of the Kalman filter is the unscented Kalman filter (UKF). During the prediction step, the UKF first places a number of sample points around the current estimate of the mean state. These points, called sigma points, are placed so that their sample mean and covariance are exactly equal to the current state mean and covariance. These sigma points are then propagated forward in time through the nonlinear state equation. The sample mean and covariance of these propagated sigma points are then used as the mean and covariance in the Kalman update step. Unlike the EKF, the UKF does not require explicitly computing the Jacobians of the state equation, making it more preferable for highly nonlinear systems. However, the number of sigma points should be equal to $2d + 1$, where d is the dimension of the state vector, which makes the UKF not ideal for high dimensional systems.

For our work, we will be using the ensemble Kalman filter (EnKF). The EnKF was introduced by Evensen [17] explicitly to address two key short-comings in the EKF: the need for explicit Jacobians, and large computational cost for high-dimensional systems.

We will describe it in more detail in the following section.

4.2.3 The Ensemble Kalman Filter

The EnKF is essentially a Monte Carlo version of the Kalman filter. Instead of describing the distribution of the system state using a mean and a covariance, we approximate the distribution using an ensemble of size N, where the state of the i-th member at time-step k is denoted by $\tilde{\boldsymbol{x}}_{i,k}$. Suppose we know the ensemble states at time-step $k-1$, we can propagate each member of the ensemble forward in time

$$\tilde{\boldsymbol{x}}_{i,k}^{-} = \boldsymbol{f}\left(\tilde{\boldsymbol{x}}_{i,k-1}\right) \quad \text{for } i = 1, 2, \cdots, N, \tag{4.25}$$

where the superscript "$-$" again indicates that no measurements have been incorporated yet. Note that there is no additive noise term as it is assumed that the randomness is naturally introduced by having an ensemble. We now approximate the pre-measurement mean and covariance of the state with their sample values

$$\hat{\boldsymbol{x}}_{k}^{-} := \frac{1}{N}\sum_{i=1}^{N} \tilde{\boldsymbol{x}}_{i,k}^{-} \tag{4.26}$$

and

$$\boldsymbol{P}_{k}^{-} := \frac{1}{N-1}\sum_{i=1}^{N} \left(\tilde{\boldsymbol{x}}_{i,k}^{-} - \hat{\boldsymbol{x}}_{k}^{-}\right)\left(\tilde{\boldsymbol{x}}_{i,k}^{-} - \hat{\boldsymbol{x}}_{k}^{-}\right)^{T}. \tag{4.27}$$

We can then substitute the sample covariance into the standard definition of the Kalman gain without further modification

$$\boldsymbol{K}_{k} = \boldsymbol{P}_{k}^{-}\boldsymbol{H}_{k}^{T}\left(\boldsymbol{V}_{k} + \boldsymbol{H}_{k}\boldsymbol{P}_{k}^{-}\boldsymbol{H}_{k}^{T}\right)^{-1}. \tag{4.28}$$

While all members of the ensemble share the same Kalman gain, they each have their own innovation. Recall that the original Kalman filter defined the innovation as

$$\boldsymbol{y}_k := \boldsymbol{z}_k - \boldsymbol{H}_k \hat{\boldsymbol{x}}_k^-. \tag{4.29}$$

In defining the innovation for each ensemble member, we can replace $\hat{\boldsymbol{x}}_k^-$ with $\tilde{\boldsymbol{x}}_{i,k}^-$. However, we cannot use the same measurement $\boldsymbol{z}_k$ for all ensemble members, as Burgers, Jan van Leeuwen, and Evensen [8] found that doing so in an ensemble no longer reflects the fact that $\boldsymbol{z}_k$ is drawn from a random variable $\mathbf{Z}_k$ and will introduce spurious correlations in the ensemble covariance. Instead, we must artificially introduce noise into the innovation of each member of the ensemble

$$\boldsymbol{y}_{i,k} := \boldsymbol{z}_k + \boldsymbol{\epsilon}_i - \boldsymbol{H}_k \tilde{\boldsymbol{x}}_{i,k}^- \quad \text{for } i = 1, 2, \cdots, N, \tag{4.30}$$

where the $\boldsymbol{\epsilon}_i$'s are drawn from $\mathbf{V}_k$. The Kalman update step is then applied to each member of the ensemble

$$\tilde{\boldsymbol{x}}_{i,k} := \tilde{\boldsymbol{x}}_{i,k}^- + \boldsymbol{K}_k \left(\boldsymbol{z}_k + \boldsymbol{\epsilon}_i - \boldsymbol{H}_k \tilde{\boldsymbol{x}}_{i,k}^- \right) \quad \text{for } i = 1, 2, \cdots, N. \tag{4.31}$$

4.2.4 Covariance Inflation

The EnKF, just like the original Kalman filter, works to minimize the covariance of the estimated state distribution. However, unlike the Kalman filter, the EnKF does not use any information about the process noise when computing the ensemble covariance. Whereas the pre-measurement covariance of the Kalman filter,

$$\boldsymbol{P}_k^- = \boldsymbol{\Phi}_k \boldsymbol{P}_{k-1} \boldsymbol{\Phi}_k^T + \boldsymbol{W}_k, \tag{4.32}$$

is bounded from below by $\boldsymbol{W}_k$, there is no lower bound to the pre-measurement ensemble covariance. If we assume a non-zero measurement covariance $\boldsymbol{V}_k$, and a ever decreasing ensemble covariance $\boldsymbol{P}_k^-$, then the Kalman gain of the ensemble eventually becomes negligible, after which all measurements are ignored by the EnKF. Methods for handling this covariance collapse are called covariance inflation. In general, covariance inflation modifies the ensemble states after computing the sample mean but before computing the sample covariance. Each ensemble state is updated by

$$\tilde{\boldsymbol{x}}_{i,k}^- \leftarrow \hat{\boldsymbol{x}}_k^- + \beta\left(\tilde{\boldsymbol{x}}_{i,k}^- - \hat{\boldsymbol{x}}_k^-\right) + \boldsymbol{\alpha}_{i,k}, \tag{4.33}$$

where β is the multiplicative inflation factor shared among all ensemble members, and $\boldsymbol{\alpha}_{i,k}$ is the additive inflation factor drawn from a random distribution at each time-step and for each ensemble member [4, 61, 34]. After this update, we recompute the ensemble mean and compute the ensemble covariance. Whitaker and Hamill [61] found that multiplicative inflation tends to be better at countering the effects of sampling errors, while additive inflation tends to be better at accounting for modeling errors. Multiplicative inflation tends to be easier to tune as it only involves adjusting a single value. Adjusting additive inflation, in contrast, requires more understanding about the actual dynamics of the underlying system.

4.2.5 Model Formulation

The model used by Ramesh and Gopalarathnam is a standard vortex blob model, with a Kutta condition applied at the trailing edge, except that the leading edge vorticity flux is governed by the LESP criterion (see Appendix A.2). Like most vortex models, the dimension of the system increases with every time-step due to leading and trailing edge vortex shedding. The steady increase of the state dimension prevents such models from

being used in any real-time applications. This is essentially the same problem that the hybrid vortex sheet/point vortex model was constructed to solve. Unfortunately, while the hybrid model performed well for high angle of attack and pitch-up problems, its use of vortex sheets make it unsuitable for flows at low angles of attack. Instead, we will adapt the underlying impulse-matching circulation transfer procedure to work with vortex blob models.

By using vortex blobs instead of vortex sheets, we lose the natural ordering of the vortex elements that was provided by the sheets. In the hybrid model, the active point vortex consumes its vortex sheet in order, starting from the sheet's wake end. When it cannot absorb any more circulation, it turns into an inactive constant-strength vortex and the tip of the vortex sheet is converted into a new active point vortex. This ordering makes it always clear which vortex element consumes circulation and which one provides it. In this work, we will take the most straightforward approach and simply try out every possible combination of source-target pairs to see which ones incur the least error in predicted force. We then perform the transfer on as many pairs as possible while keeping the accumulated error below a specified threshold, ϵ_F.

The vortex aggregation procedure is simply a modified version of the circulation transfer procedure described in Section 3.2.3. Once we have determined an appropriate value for ϵ_F, we do the following at every time-step:

1. For every possible source-target pair of vortex blobs in the model, use Equation (3.11) to compute the velocity correction required to transfer all of the source's circulation into the target.

2. Compute the (uncorrected) velocities of all vortex blobs and evolve the system forward by one time step.

3. Compute the impulse for each vortex blob.

4. For every possible source-target pair of vortex blobs in the system, first compute the

hypothetical impulse that the target blob would have if it absorbed all the circulation from the source blob and applied the velocity correction computed from step 1. Then, subtract from this the actual impulse of the source and target blobs, computed in step 3. This difference, when divided by time-step size, is defined as the transfer error.

5. Sort the source-target pairs based on the magnitude of their transfer error.

6. Starting from the pair with the lowest error, transfer circulation between as many pairs of vortex blobs as possible, stopping just before the accumulated error exceeds ϵ_F.

Although the procedure listed above contains multiple steps with pairwise interactions that we usually try to avoid, it also works to eliminate the number of vortex particles in the system. In practice, the computational savings of keeping the state dimension small far outweighs the cost of executing this procedure at every time-step.

4.2.6 Applying the EnKF to a Vortex Model

The state of our vortex model consists of the positions and strengths of the vortex blobs, as well as the current estimate of the critical LESP

$$\boldsymbol{x}_{k-1} := \begin{bmatrix} x^1_{k-1} & y^1_{k-1} & \Gamma^1_{k-1} & \cdots & x^n_{k-1} & y^n_{k-1} & \Gamma^n_{k-1} & \text{LESP}^c_{k-1} \end{bmatrix}^T. \tag{4.34}$$

The nonlinear state transition function $\boldsymbol{f}_k$ propagates the state at time step $k-1$ by

1. computing the bound vortex sheet strength on the plate using the vortex blob positions and strengths

2. computing the velocities of the vortex blobs

3. advecting the plate and vortex blobs

4. applying the vortex aggregation algorithm, reducing the strength of any aggregated blobs to zero instead of completely removing the blob

5. releasing a new vortex blob from each edge of the plate with strengths based on the current estimate of the critical LESP.

Note that the dimensions of the state increase by six (three per new vortex blob) after every state propagation step. Once all members of the ensemble have been propagated, we look for any vortex blobs that have zero strength across *all* members of the ensemble (in terms of its position/index in the state vector) and eliminate them from the ensemble states. This particle elimination process, in conjunction with the vortex aggregation algorithm, works to reduce the dimension of the state vector. We then apply covariance inflation to the new ensemble states, before computing the pre-measurement ensemble mean $\hat{\boldsymbol{x}}_k^-$ and ensemble covariance $\boldsymbol{P}_k^-$ with Equations (4.26) and (4.27).

Our measurements consist of M pressure differences along the plate at every time-step k

$$\boldsymbol{z}_k := \begin{bmatrix} \Delta p_k^1 & \cdots & \Delta p_k^M \end{bmatrix}^T. \tag{4.35}$$

Let us denote the pressure distribution predicted by the i-th ensemble member at time-step k as

$$\boldsymbol{m}_{i,k} := \boldsymbol{h}_k\left(\tilde{\boldsymbol{x}}_{i,k}^-\right). \tag{4.36}$$

Then the innovation for each member of the ensemble is given by

$$\boldsymbol{y}_{i,k} = \boldsymbol{z}_k + \boldsymbol{\epsilon}_i - \boldsymbol{m}_{i,k}. \tag{4.37}$$

Since pressure is definitely not a linear function on vortex properties, we need to linearize $\boldsymbol{h}_k$ in order to compute the ensemble Kalman gain. One simple way is to define an

augmented state vector

$$\boldsymbol{X}_{i,k} := \begin{bmatrix} \tilde{\boldsymbol{x}}_{i,k}^{-} \\ \boldsymbol{m}_{i,k} \end{bmatrix} \tag{4.38}$$

which admits the linear measurement function

$$\boldsymbol{H}_k := \begin{bmatrix} \boldsymbol{0}^{(3n+1)\times(3n+1)} & \boldsymbol{I}^{M\times M} \end{bmatrix}. \tag{4.39}$$

Then, denoting the mean predicted pressure distribution as

$$\bar{\boldsymbol{m}}_k := \frac{1}{N}\sum_{i=1}^{N} \boldsymbol{m}_{i,k}, \tag{4.40}$$

the covariance of the predicted pressure distribution as

$$\boldsymbol{M}_k := \frac{1}{N-1}\sum_{i=1}^{N} \left(\boldsymbol{m}_{i,k} - \bar{\boldsymbol{m}}_k\right)\left(\boldsymbol{m}_{i,k} - \bar{\boldsymbol{m}}_k\right)^T \tag{4.41}$$

and the cross-covariance between the state and pressure with

$$\boldsymbol{C}_k := \frac{1}{N-1}\sum_{i=1}^{N} \left(\tilde{\boldsymbol{x}}_{i,k}^{-} - \hat{\boldsymbol{x}}_k\right)\left(\boldsymbol{m}_{i,k} - \bar{\boldsymbol{m}}_k\right)^T, \tag{4.42}$$

we find that the ensemble covariance of the augmented state can be written as

$$\boldsymbol{P}_k^a := \frac{1}{N-1}\sum_{i=1}^{N} \left(\begin{bmatrix} \left(\tilde{\boldsymbol{x}}_{i,k}^{-} - \hat{\boldsymbol{x}}_k\right) \\ \left(\boldsymbol{m}_{i,k} - \bar{\boldsymbol{m}}_k\right) \end{bmatrix} \begin{bmatrix} \left(\tilde{\boldsymbol{x}}_{i,k}^{-} - \hat{\boldsymbol{x}}_k\right)^T \left(\boldsymbol{m}_{i,k} - \bar{\boldsymbol{m}}_k\right)^T \end{bmatrix} \right) \tag{4.43}$$

$$= \begin{bmatrix} \boldsymbol{P}_k^{-} & \boldsymbol{C}_k \\ \boldsymbol{C}_k^T & \boldsymbol{M}_k \end{bmatrix}. \tag{4.44}$$

The Kalman gain of the pressure-augmented system is then

$$\boldsymbol{K}_k^a = \boldsymbol{P}_k^a \boldsymbol{H}_k^T \left(\boldsymbol{V}_k + \boldsymbol{H}_k \boldsymbol{P}_k^a \boldsymbol{H}_k^T\right)^{-1} = \begin{bmatrix} \boldsymbol{C}_k (\boldsymbol{V}_k + \boldsymbol{M}_k)^{-1} \\ \boldsymbol{M}_k (\boldsymbol{V}_k + \boldsymbol{M}_k)^{-1} \end{bmatrix}. \tag{4.45}$$

Since only the first block in the Kalman gain matrix above corresponds to the actual states we are interested in, we can write the EnKF Kalman update step for our system as

$$\tilde{\boldsymbol{x}}_{i,k} = \tilde{\boldsymbol{x}}_{i,k}^- + \boldsymbol{C}_k (\boldsymbol{V}_k + \boldsymbol{M}_k)^{-1} \left(\boldsymbol{z}_k + \boldsymbol{\epsilon}_i - \boldsymbol{h}_k(\tilde{\boldsymbol{x}}_{i,k}^-)\right) \tag{4.46}$$

4.2.7 Results

We demonstrate this method on three test problems with increasing complexity. The first case is impulsive translation of a flat plate at a 20° angle of attack. The second case starts off the same way as the first, then we apply leading edge actuation at 3 convective times. The last case builds on the second case by adding yet another pulse of actuation at 4 convective times. For our measurements, we probe the pressure differences across the plate along $M = 50$ points, with a distribution given by

$$\frac{c}{2} \cos\left(\frac{m\pi}{M+1}\right) \quad \text{for } m = 1, 2, \cdots, M. \tag{4.47}$$

The pressure measurements we use are obtained from high-fidelity CFD results for $\mathrm{Re} = 500$. However, this method should be agnostic to the source of pressure measurements, especially as it is intended to be used for real-time flow control. Ultimately, we would like to replace these numerically computed pressure measurements with experimental data.

We use an ensemble size of $N = 50$ and initialize each ensemble member with a starting value of critical LESP drawn from $\mathcal{N}(0.5,\, 0.2)$. We set the error tolerance of the vortex aggregation procedure to $\epsilon_F = 10^{-3}$. For time-marching, we use the forward-Euler scheme

with a fixed time-step of $\Delta t = 10^{-2} Ut/c$.

No Pulse Actuation

The pulse-free case serves as a baseline for us to confirm our understanding of how pressure, critical LESP and the vortex model interact with each other. Figure 4.6 and Figure 4.7 respectively show the pressure distribution and force predicted by the EnKF-assisted model. In Figure 4.8 we show the ensemble mean of the critical LESP over time. Then in Figure 4.9 we show the number of vortex elements used by the model over time. Note that since we add and remove the same number of vortex particles to every member of the ensemble, the particle count history in Figure 4.9 applies to any member of the ensemble. We show how using covariance inflation affects the variance of the ensemble state in Figures 4.10 to 4.12. Finally, in Figures 4.13 to 4.16, we compare the vorticity distributions predicted by the EnKF using different covariance inflation schemes at different convective times.

The top plot in Figure 4.6 shows the pressure distribution given by CFD. This is the pressure distribution that we are trying to match. Visually, we can immediately see the growth of a LEV, indicated by the expansion of a negative pressure region towards the trailing edge. As the LEV stretches across the whole chord at around three convective times, it starts to entrain opposite-signed vorticity and trigger the growth of a TEV, which shows up as a thin sliver of negative pressure between three and five convective times. At around five convective times, we see a small positive pressure region at the trailing edge, which along with the diminishing TEV pressure signature, suggest the shedding of the TEV. These events are also observed at the corresponding times in the top right plots of Figures 4.13 to 4.16, which show the vorticity contours predicted by the CFD.

The second plot in Figure 4.6 shows the pressure distribution predicted by the EnKF ensemble mean when no covariance inflation is applied. We see a much more aggressive growth of the LEV in terms of both strength and density. We also see evidence of co-rotating vortex blobs in the crisscrossing wave-like structure in the pressure distribution.

Unfortunately, this indicates that the EnKF is not having any corrective effect on the model. This is consistent with our previous discussion of covariance collapse. In Figure 4.12, we see that the ensemble variance of the states drop to negligible values almost immediately after we start running the model. Without any inflation to counter the covariance collapse, the EnKF essentially ignores the CFD pressure data.

The third plot in Figure 4.6 shows the EnKF-predicted pressure distribution when a 5% multiplicative inflation is used. Although we can still visibly observe the pressure signature of co-rotating vortex blobs, we see that the LEV structure is more diffuse compared to the case without inflation. Looking at Figure 4.11, we see that after the initial covariance collapse, the multiplicative inflation is able to slowly increase the variance of the vortex positions and strengths. However, the variance in the critical LESP is so small that it is immune to multiplicative inflation. This means that the EnKF can no longer influence the leading edge vorticity flux. To assimilate the pressure data, the EnKF can only rely on modifying the vortex positions and strengths. As a result, we often observe "teleporting" vortex blobs in videos, though it is difficult to show here through static figures.

The final plot in Figure 4.6 shows the pressure distribution predicted by the EnKF after we apply both multiplicative and additive inflation. After tuning the inflation parameters, we found a suitable set of values:

- 1% multiplicative inflation
- additive perturbation to the vortex positions drawn from $\mathcal{N}\left(0,\, 10^{-5}c\right)$
- additive perturbation to the vortex strengths drawn from $\mathcal{N}\left(0,\, 10^{-3}\frac{1}{\Delta t}\right)$
- additive perturbations to the critical LESP drawn from $\mathcal{N}\left(0,\, 5\times 10^{-5}\right)$.

We can clearly see that the predicted pressure distribution closely matches the CFD pressure distribution. This is further validated in Figure 4.7, where the model-predicted force coefficient was computed using the rate of change of impulse rather than integrating the

surface pressures. While there is some noise in the predicted force, we see that it agrees well with the CFD results.

The covariance inflation parameters were tuned to coerce the EnKF into favoring the modification of the critical LESP over the vortex blob positions and strengths. This stems from our underlying assumption that the key process is still governed by inviscid vortex dynamics, and assimilating pressure data through the EnKF simply provides a closure model to determine vorticity flux. If we look at Figure 4.8, we see that the estimated critical LESP values remain relatively constant in time. Note that this does *not* mean that the leading edge vorticity flux is constant, since the vorticity flux required to maintain a fixed leading edge suction depends on the state of the ambient fluid. This result does seem to reflect the hypothesis from Ramesh and Gopalarathnam that the critical LESP value is mainly dependent on Reynolds number and relatively independent of the wing kinematics.

Comparing the placement of vortex blobs in Figures 4.13 to 4.16, we see that the distributions predicted with both additive and multiplicative inflation are much more representative of the vorticity contours obtained from CFD. From Figure 4.9, we see that even after five convective times, each member of the ensemble is only using about 40 vortex blobs. This tells us that the vortex aggregation procedure is also working correctly as it eliminated almost a thousand vortex particles without any adverse effects. With such a small number of vortex elements, it is surprising that the EnKF-assisted model was able to generate a LEV with such a diffuse pressure signature. Of course, as the EnKF can still make small changes to the vortex state, it may be worth investigating whether the EnKF is introducing some measure of viscosity into the model.

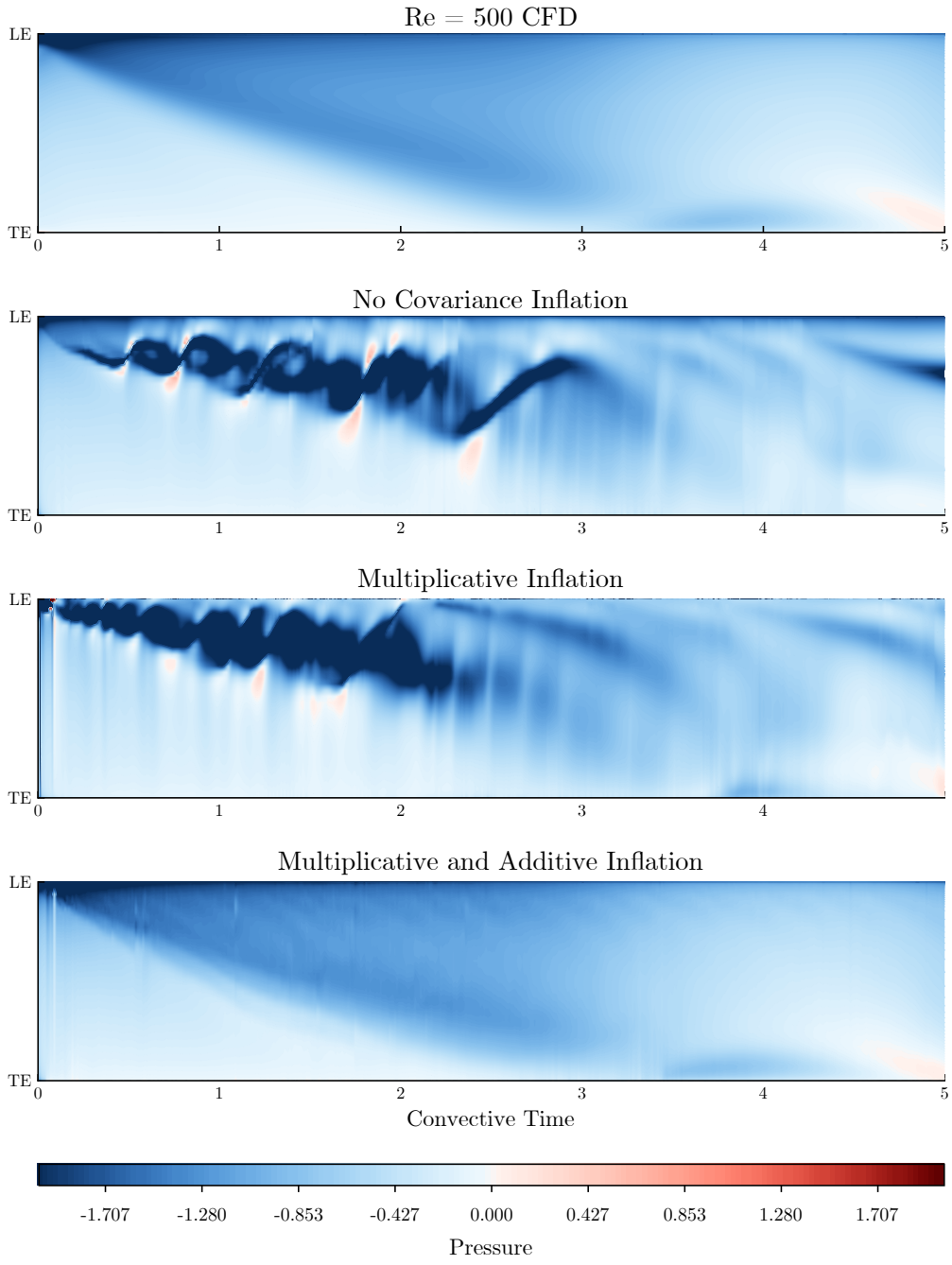

Figure 4.6: Comparison of the pressure coefficient distribution along the plate over time between the CFD results and EnKF predictions with various covariance inflation settings for the pulse-free case.

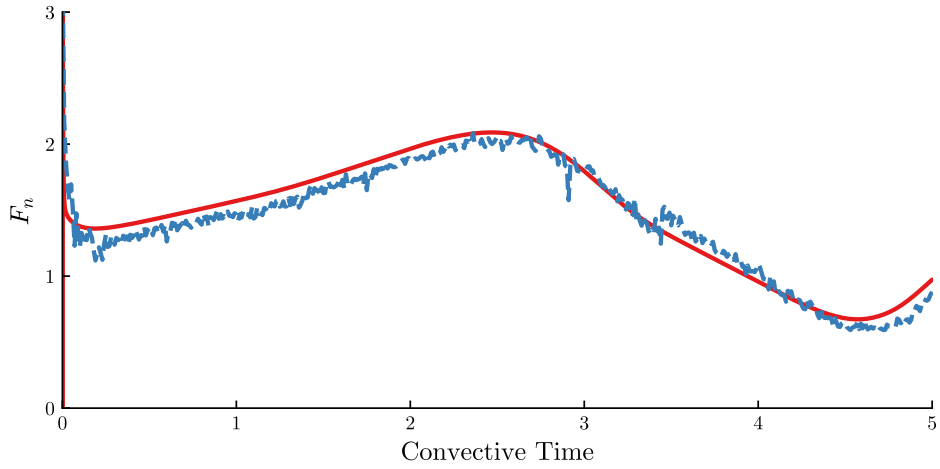

Figure 4.7: Comparison of the predicted normal force between (—) CFD results, and (—) EnKF ensemble mean for the pulse-free case.

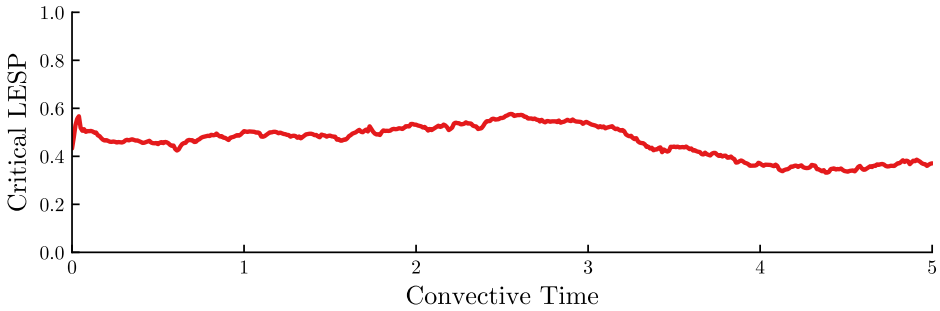

Figure 4.8: Time history of the ensemble mean value of the critical LESP for the pulse-free case

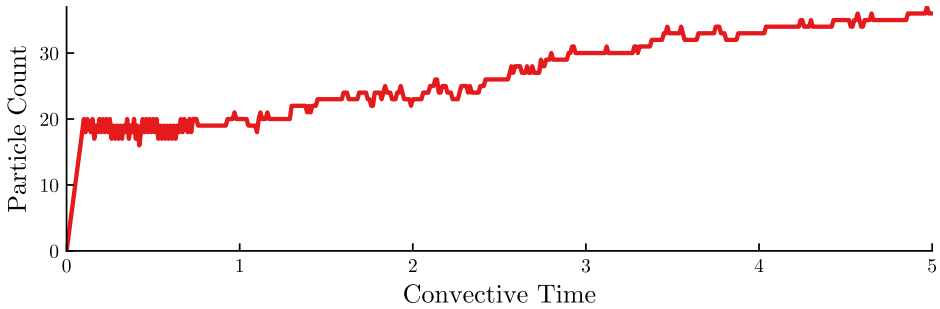

Figure 4.9: Number of vortex blobs used in the model over time when a combined multiplicative and additive covariance inflation is used for the pulse-free case

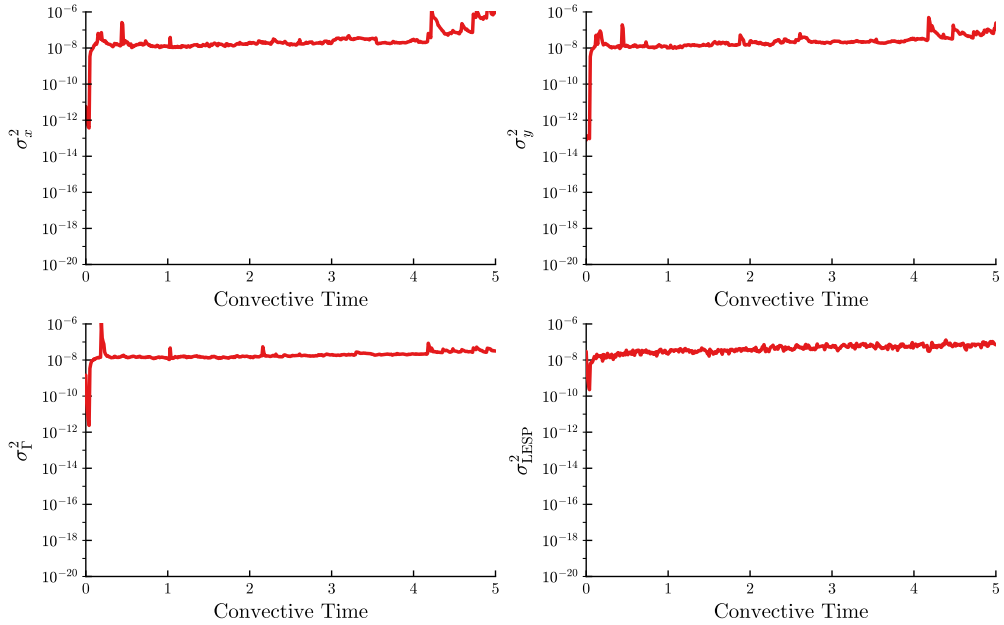

Figure 4.10: Ensemble variances for the pulse-free case with both multiplicative and additive covariance inflation

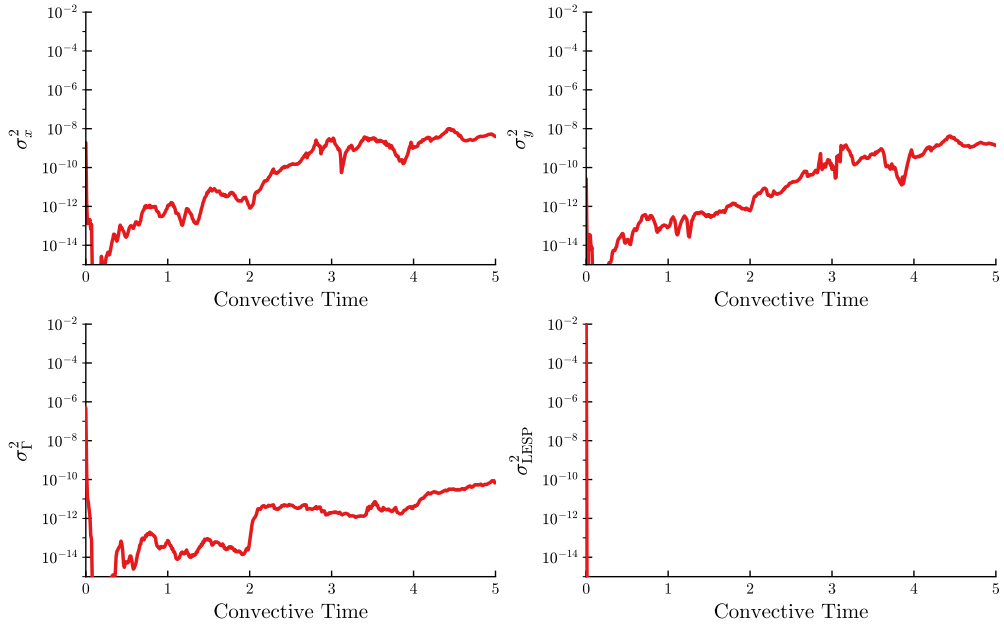

Figure 4.11: Ensemble variances for the pulse-free case with multiplicative covariance inflation

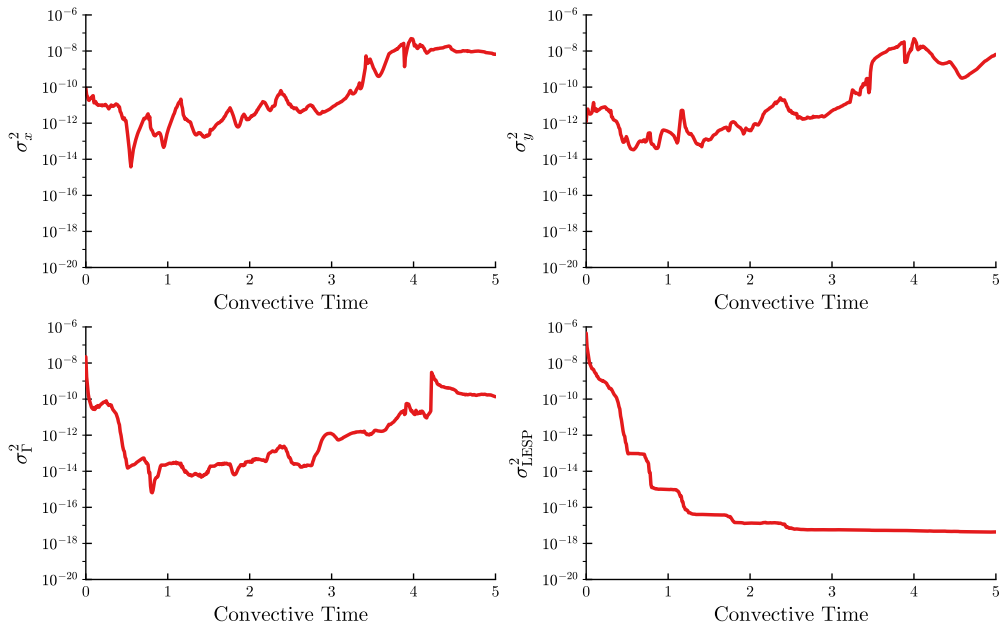

Figure 4.12: Ensemble variances for the pulse-free case without covariance inflation

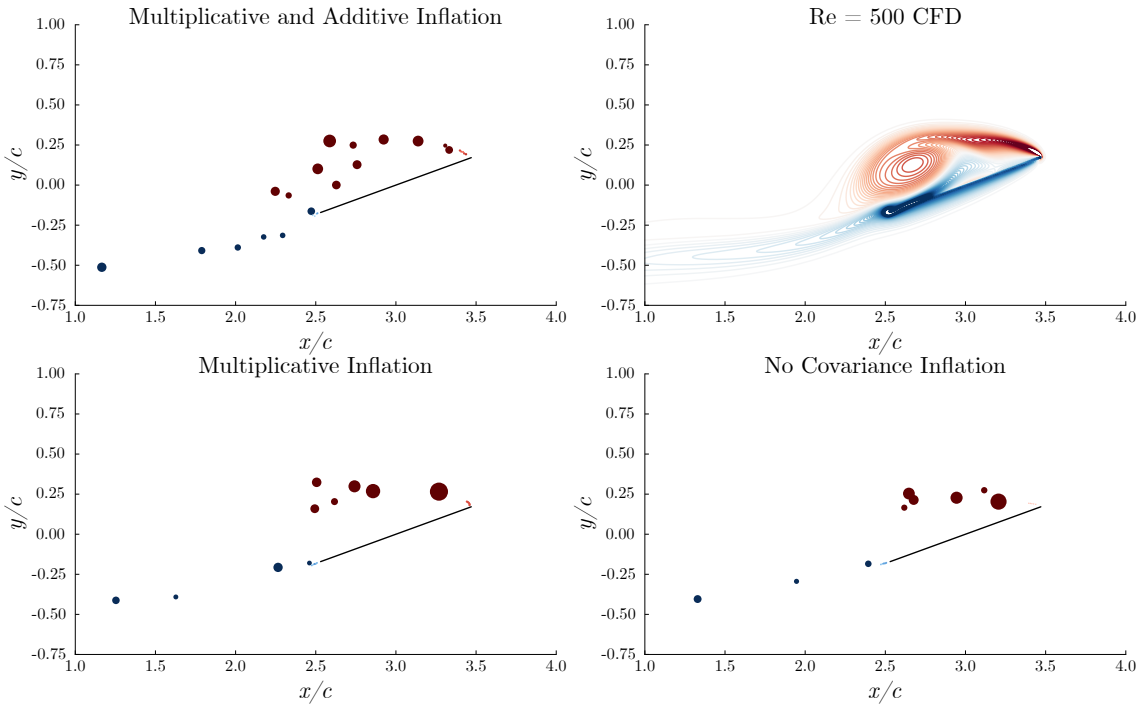

Figure 4.13: Comparison of the vorticity distribution for the pulse-free case at 3 convective times.

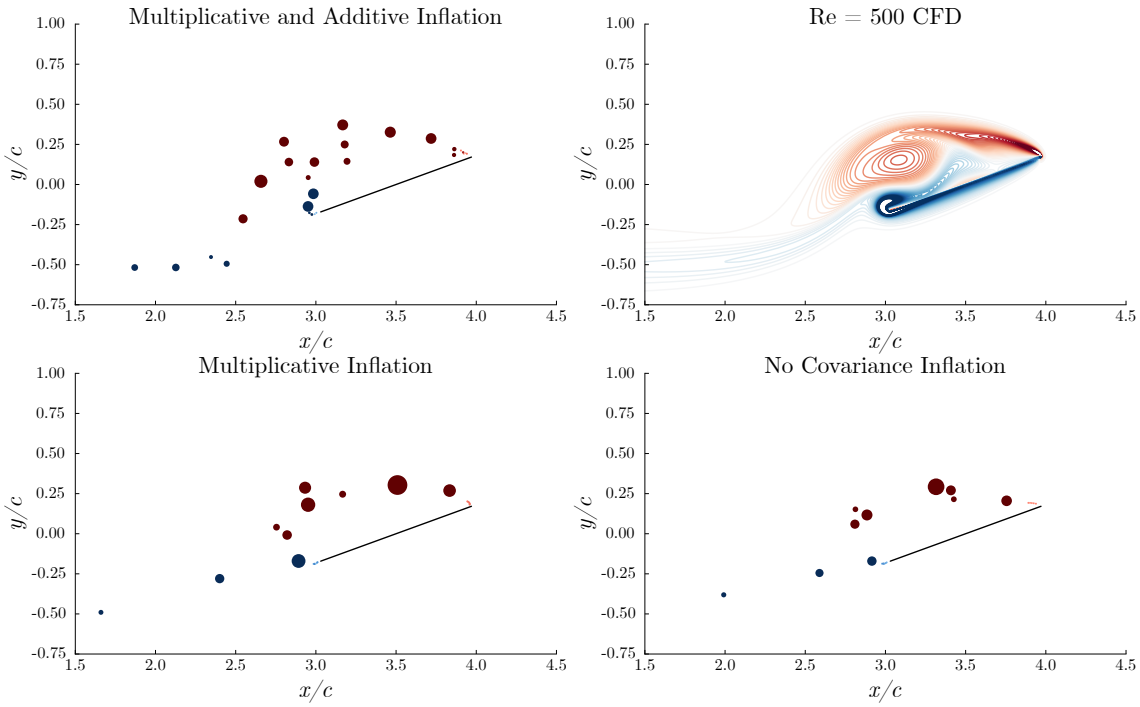

Figure 4.14: Comparison of the vorticity distribution for the pulse-free case at 3.5 convective times.

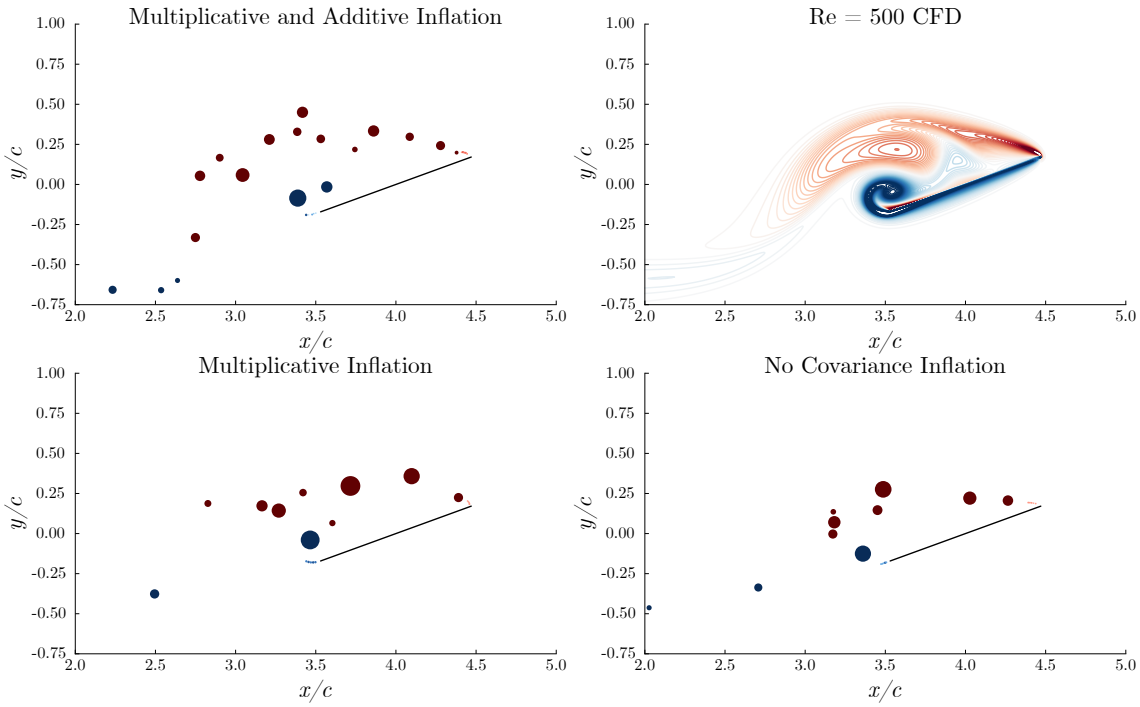

Figure 4.15: Comparison of the vorticity distribution for the pulse-free case at 4 convective times.

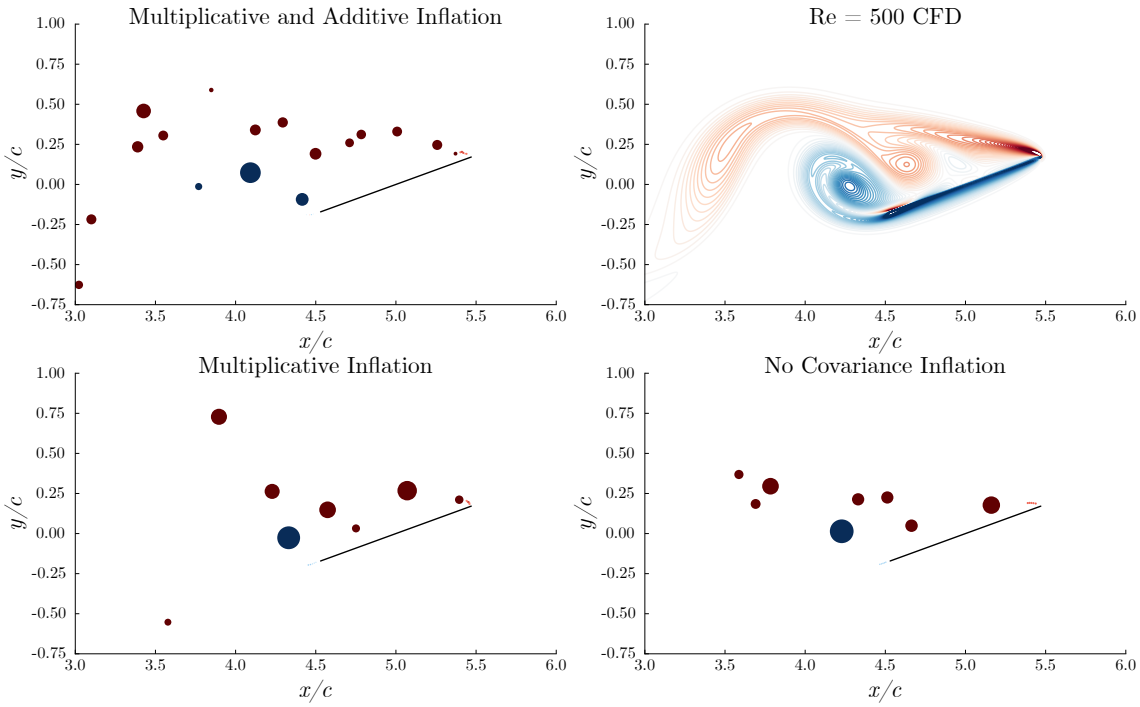

Figure 4.16: Comparison of the vorticity distribution for the pulse-free case at 5 convective times.

Single Pulse Actuation

Now we consider the case where a single pulse is applied at the leading edge around three convective times. As with the pulse-free case, we start by considering the pressure distributions in Figure 4.17. The top plot shows the pressure distribution predicted by high-fidelity CFD. We see that the initial development of the LEV is identical to the pulse-free case. At three convective times, we see the pulse as a band of negative pressure across the chord. Although the pulse itself is short-lived, we see that it triggers the growth of a new LEV. The new LEV is promptly absorbed into the old LEV, essentially returning the state back to the pulse-free case.

The second plot in Figure 4.17 shows the pressure distribution predicted without covariance inflation. As expected, the covariance collapse makes the ensemble blind to the pulse. The appearance of the pulse on the pressure distribution predicted with multiplicative inflation, shown in the third plot of Figure 4.17, indicates that the EnKF is attempting

to assimilate the pressure data. At three convective times, we see that the predicted distribution of vortex blobs in the lower left plot of Figure 4.23 still resembles the CFD vorticity contours on the figure's upper right plot. However, in Figure 4.24, we see that while the CFD vorticity contours show the development of a new LEV, the EnKF with multiplicative inflation increased the strength of a vortex blob close to the trailing edge instead. Although it was able to push the predicted pressure distribution closer to the CFD results, the EnKF's heavy modification of the vortex states created very unnatural dynamics.

The EnKF-predicted pressure distribution that most closely resembles the CFD results came from using both additive and multiplicative inflation, shown in the bottom plot in Figure 4.17. We use the same inflation parameters as the pulse-free case, which gives us a relatively stable set of ensemble variances, as shown in Figure 4.21. Despite the fact that the sample variance in critical LESP is on the order of 10^{-8}, that amount of variation between the ensemble members is still enough that in Figure 4.19, we see the EnKF responding to the measured pressure pulse by temporarily increasing the critical LESP. As the increase in critical LESP tends to reduce vorticity flux, we see that this small pulse in the critical LESP has the effect of severing the leading edge shear layer before developing a new LEV.

Comparing the distribution of vortex blobs in Figures 4.23 to 4.26, we see that the corrections made by the EnKF seem to have the effect of spreading out the vorticity over a larger area. This is especially noticeable when comparing the results between the EnKF results with combined inflation (top left plots), and those without covariance inflation (bottom right plots). Even though the LEV was spread over more vortex blobs, we see in Figure 4.20 that the vortex aggregation process has kept the total number of vortex particles very low.

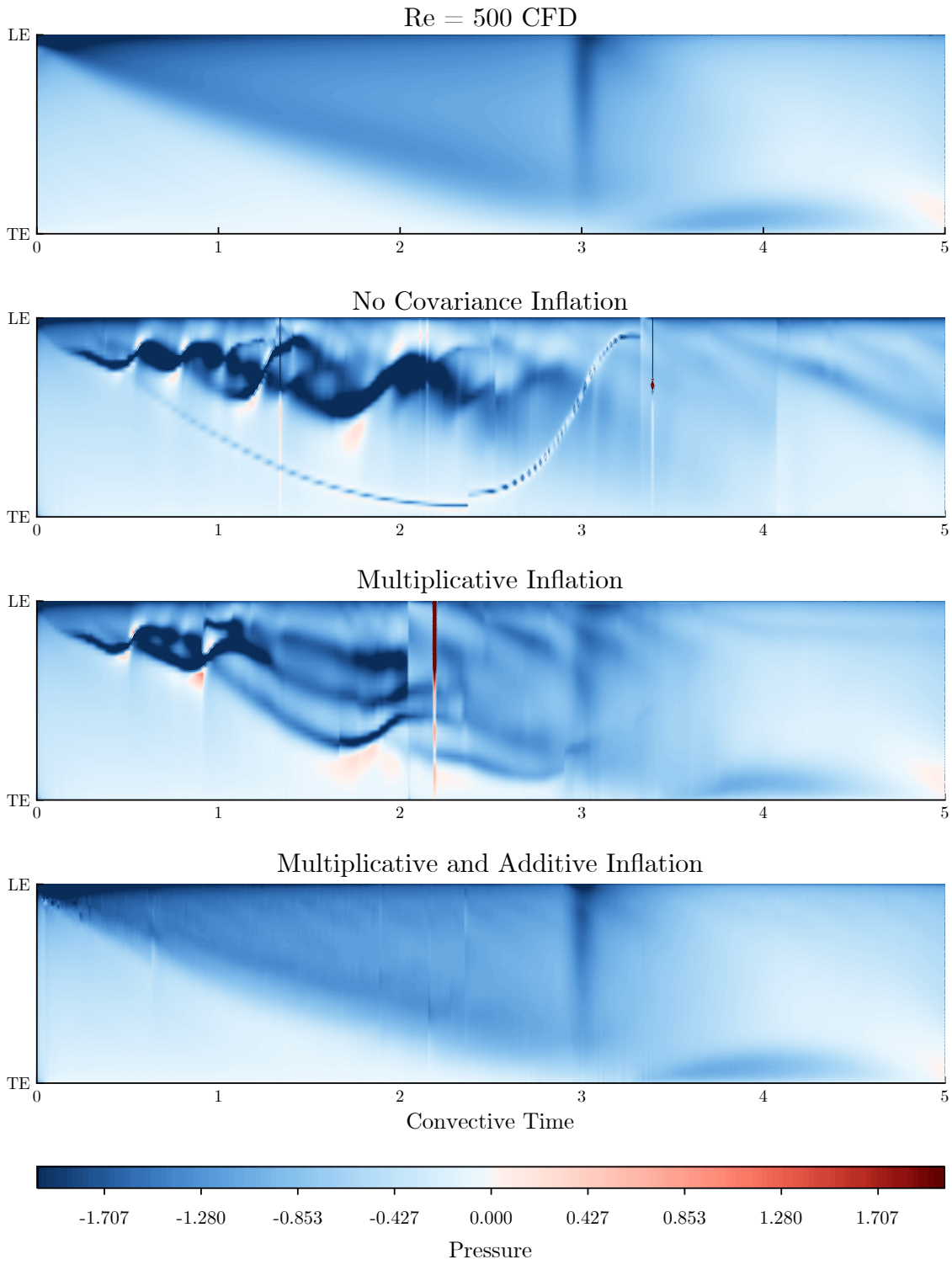

Figure 4.17: Comparison of the pressure coefficient distribution along the plate over time between the CFD results and EnKF predictions with various covariance inflation settings for the single pulse case

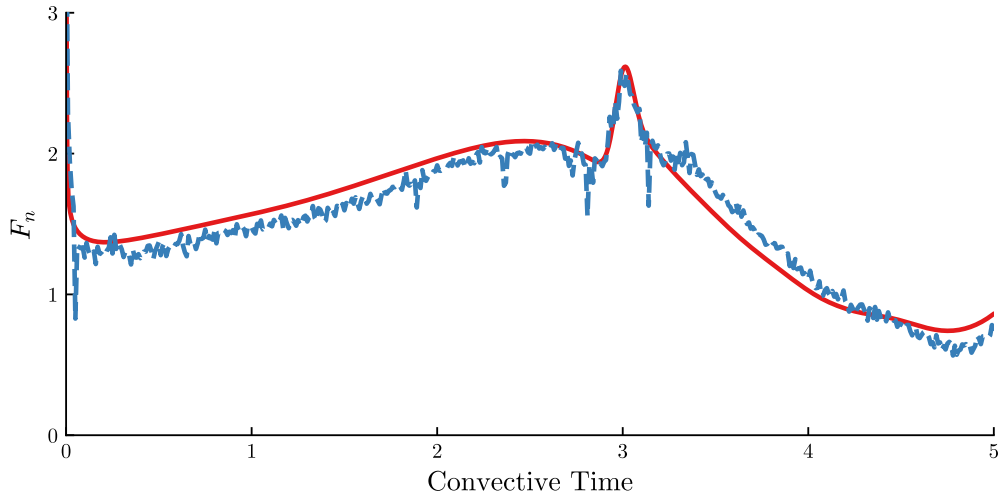

Figure 4.18: Comparison of the predicted normal force between (—) CFD results, and (—) EnKF ensemble mean for the single pulse case.

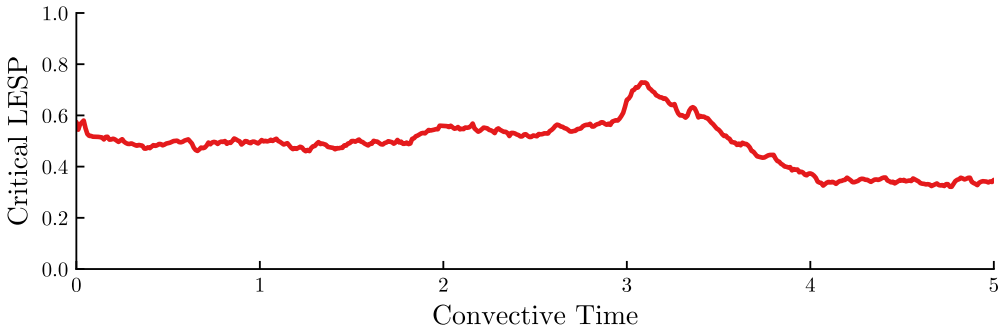

Figure 4.19: Time history of the ensemble mean value of the critical LESP for the single pulse case

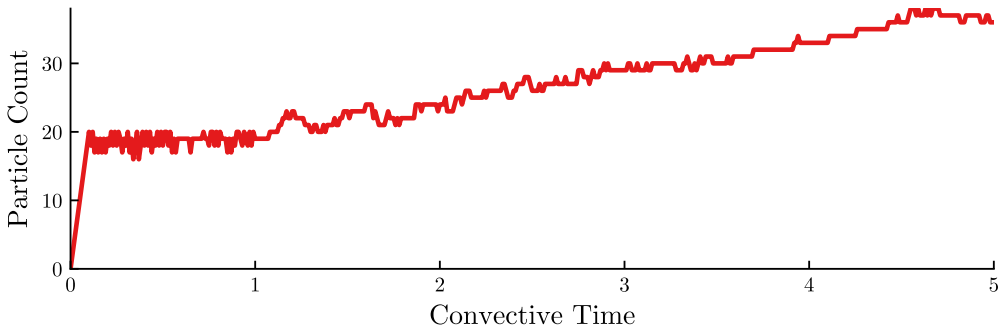

Figure 4.20: Number of vortex blobs used in the model over time when a combined multiplicative and additive covariance inflation is used for the single pulse case

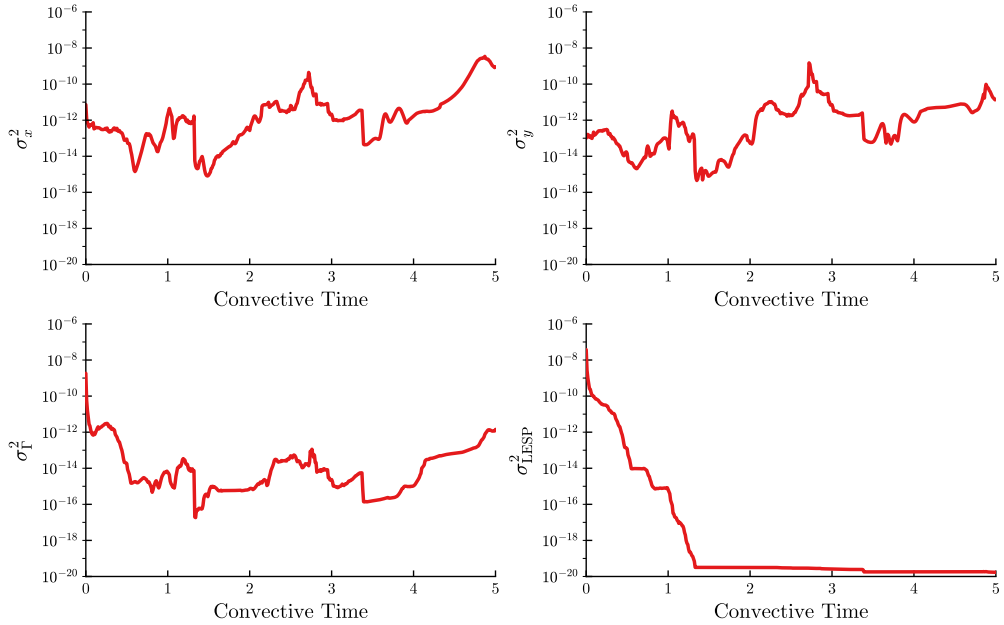

Figure 4.22: Ensemble variances for the single pulse case without covariance inflation

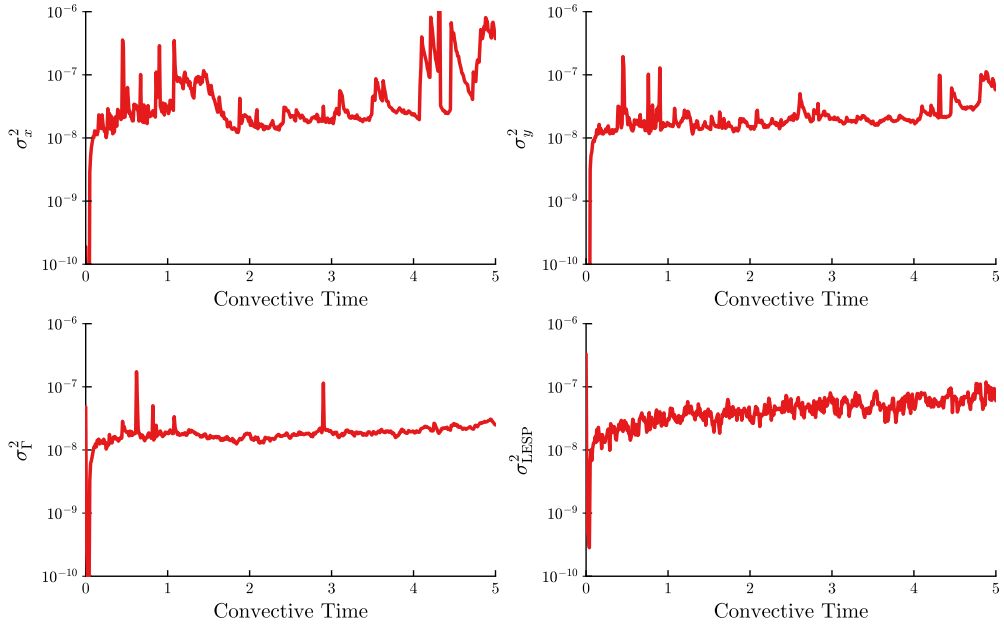

Figure 4.21: Ensemble variances for the single pulse case with both multiplicative and additive covariance inflation

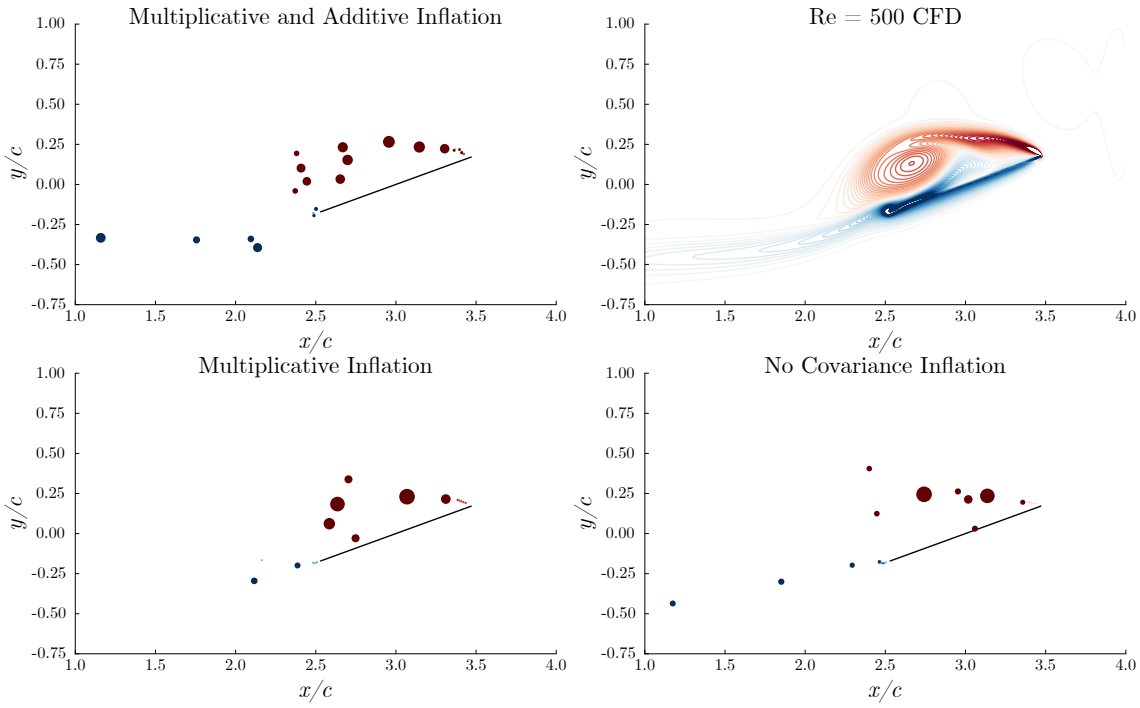

Figure 4.23: Comparison of the vorticity distribution for the single pulse case at 3 convective times.

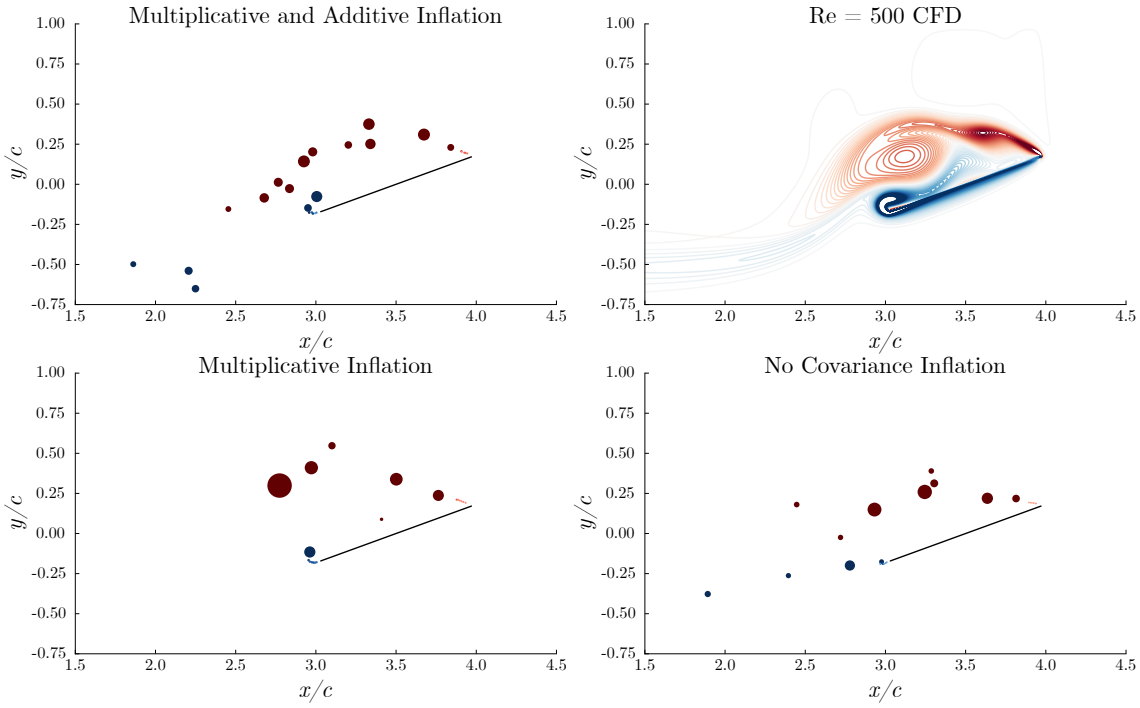

Figure 4.24: Comparison of the vorticity distribution for the single pulse case at 3.5 convective times.

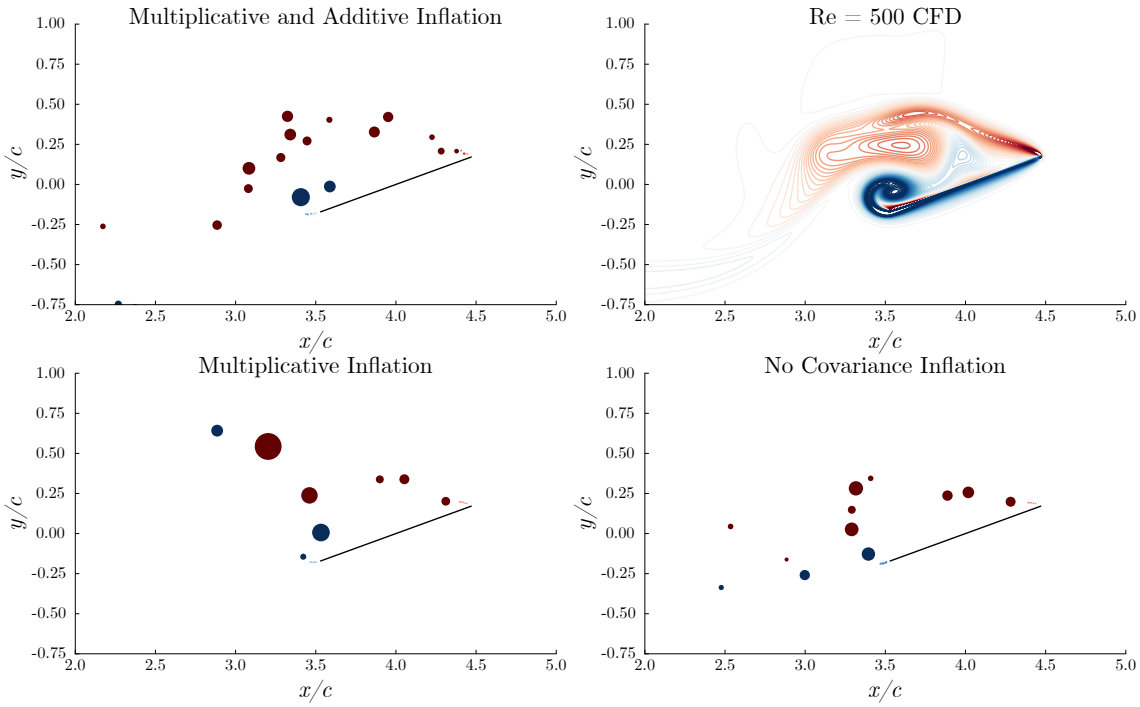

Figure 4.25: Comparison of the vorticity distribution for the single pulse case at 4 convective times.

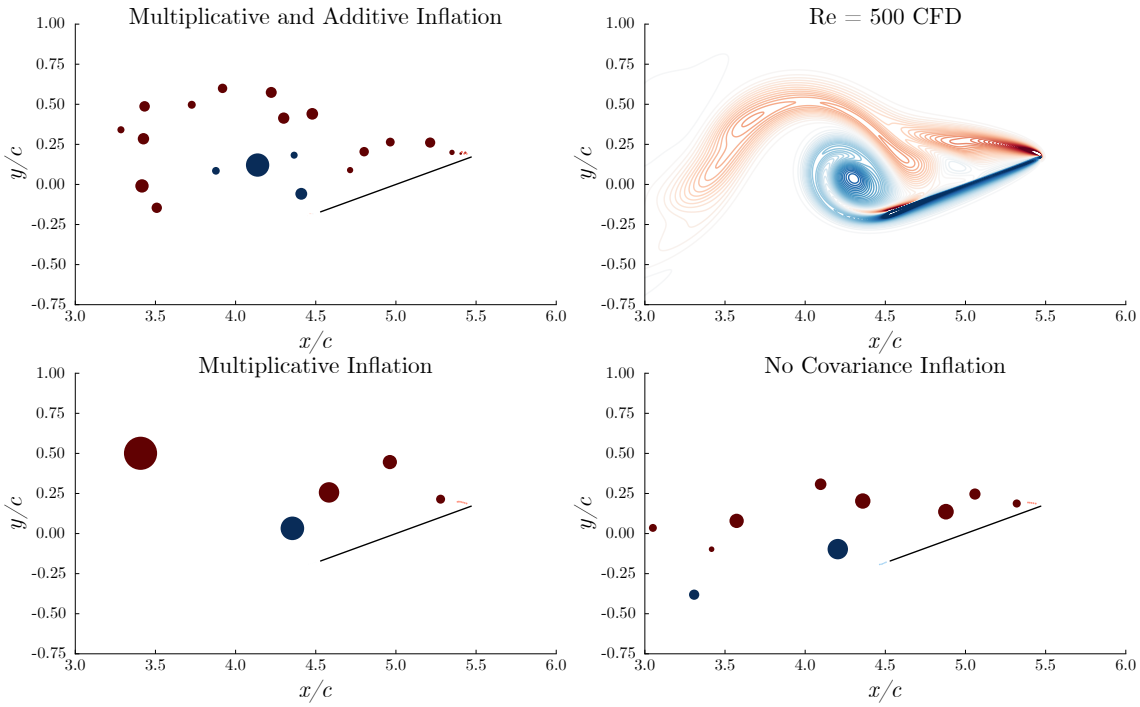

Figure 4.26: Comparison of the vorticity distribution for the single pulse case at 5 convective times.

Double Pulse Actuation

Finally, we look at the case with two pulse actuations, one at three convective times and one at four convective times. Since we also use the same covariance inflation parameters as the two previous cases, the results up to the second pulse are essentially the same as the results for the single pulse case, so we will just discuss the differences. From the pressure distribution in Figure 4.27, force comparison in Figure 4.28, and critical LESP history in Figure 4.29, we see that the EnKF with a combined inflation scheme had no problems capturing the second pulse.

From the pressure distribution predicted by CFD, we see that whereas the first pulse created a new LEV that was absorbed by the old LEV, the second pulse occurred after the old LEV had been lifted off by the TEV. In this particular case, the second pulse was initiated just as a new, replacement LEV was developing. We see from Figure 4.35, both in the CFD vorticity contours (top right) and in the vortex blob distribution predicted by the EnKF with combined inflation (top left), that any new vortex structure created by the second pulse was merged into the newly developing LEV.

At 3.5 convective times, the second pulse has not been applied yet, so we expect the same distributions of vorticity between the single pulse case and the two pulses case. Interstingly, if we compare the vortex blob distributions in Figure 4.33 and those listed in Figure 4.24, we see that the distributions predicted with multiplicative covariance inflation look very different across the two cases. In contrast, the vortex blob distributions predicted by the combined inflation scheme agree well. This reinforces the idea that without careful tuning of the additive inflation or some means of localizing the Kalman gain matrix [23], the EnKF and the nonlinear system dynamics can work together to amplify spurious correlations and prevent the ensemble from actually converging.

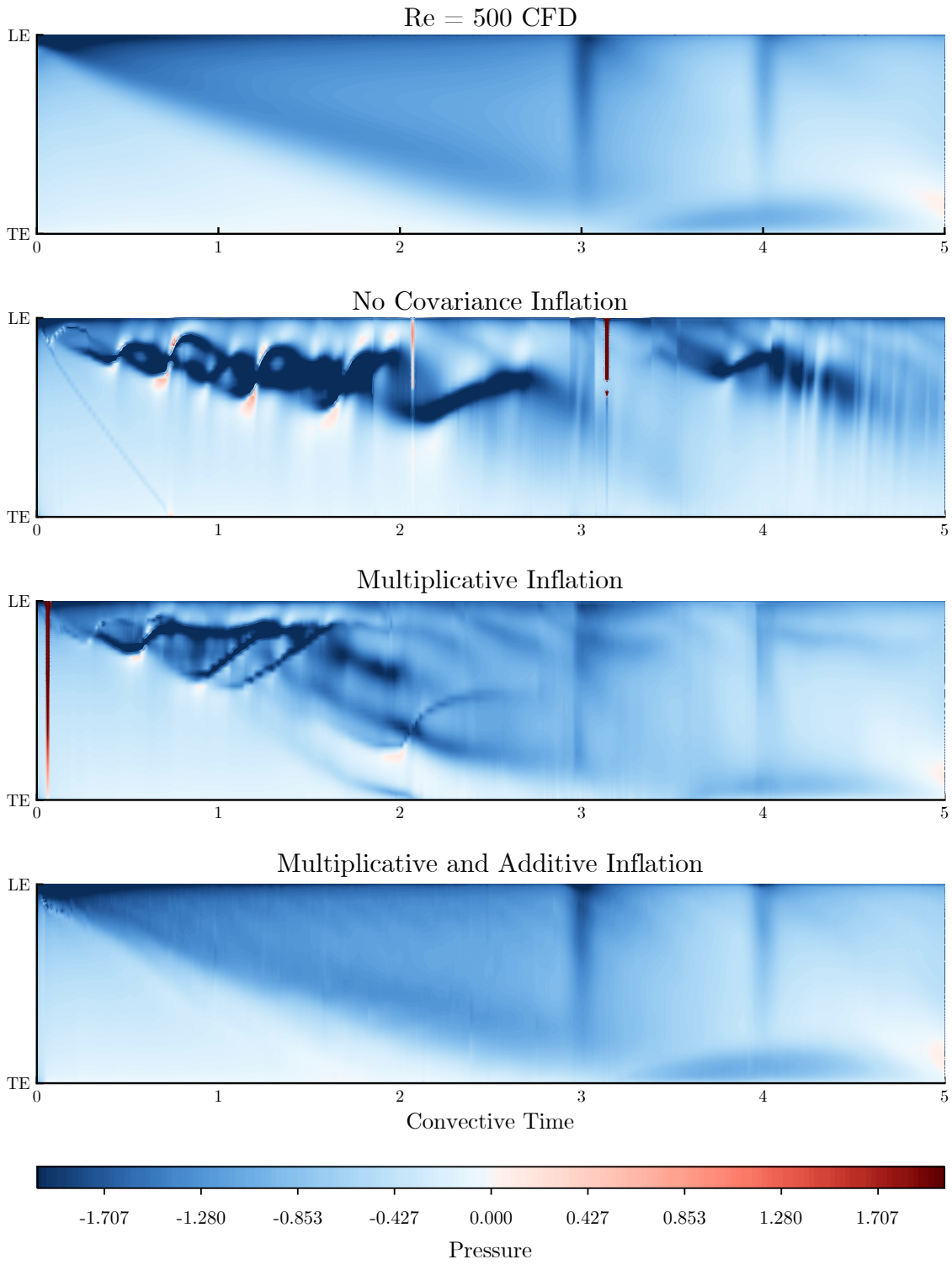

Figure 4.27: Comparison of the pressure coefficient distribution along the plate over time between the CFD results and EnKF predictions with various covariance inflation settings for the two pulses case

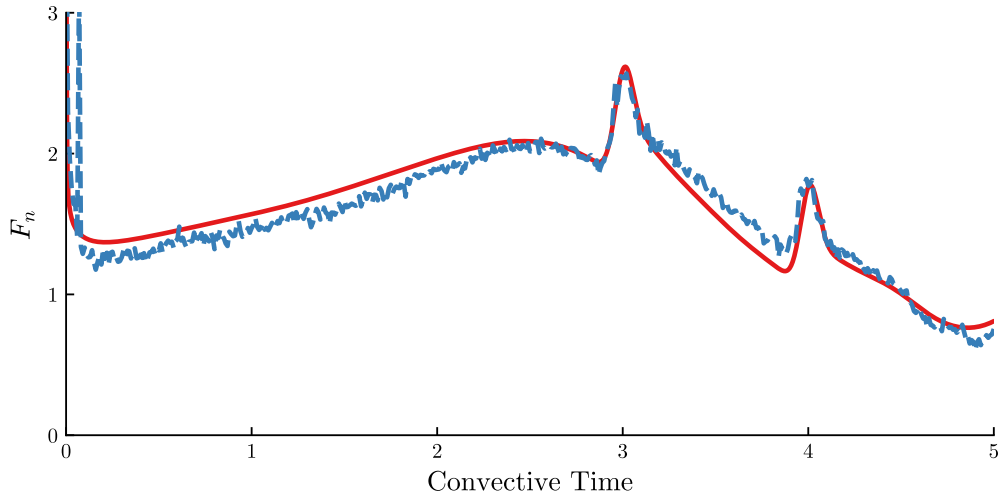

Figure 4.28: Comparison of the predicted normal force between (—) CFD results, and (—) EnKF ensemble mean for the two pulses case.

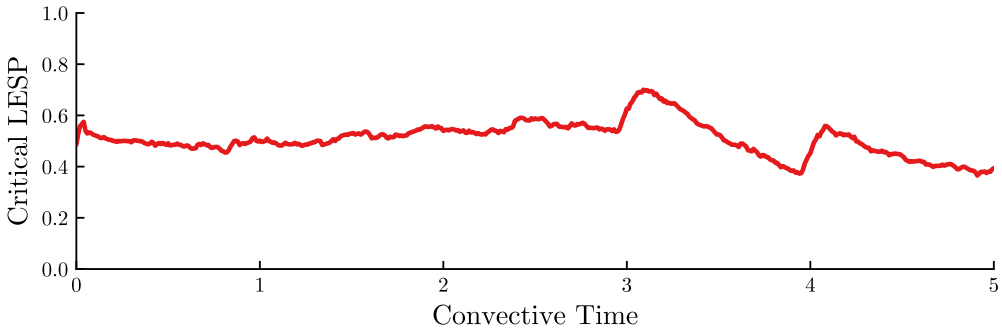

Figure 4.29: Time history of the ensemble mean value of the critical LESP for the two pulses case

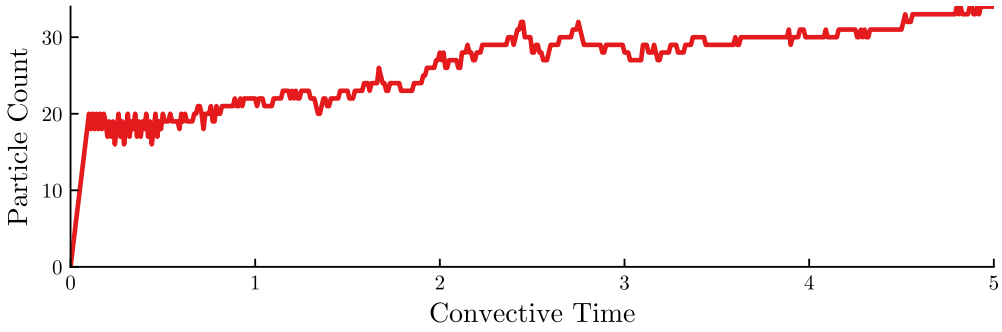

Figure 4.30: Number of vortex blobs used in the model over time when a combined multiplicative and additive covariance inflation is used for the two pulses case

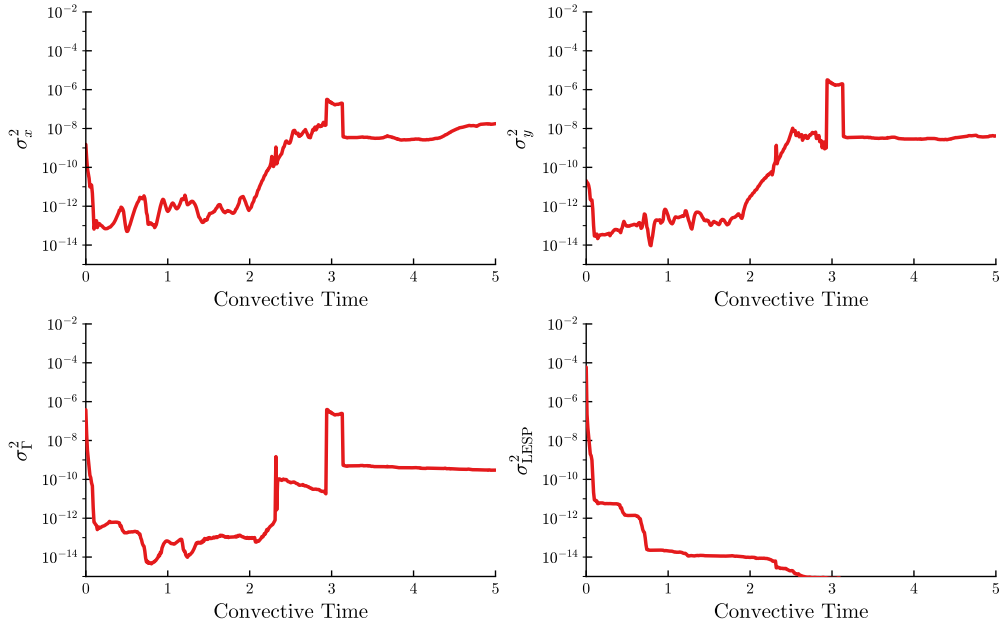

Figure 4.32: Ensemble variances for the two pulses case without covariance inflation

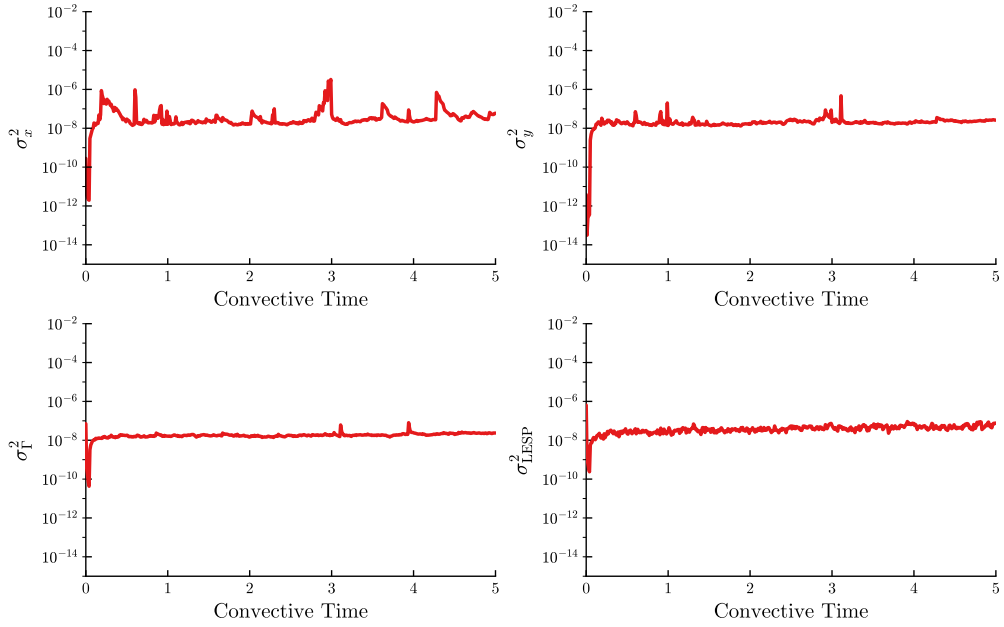

Figure 4.31: Ensemble variances for the two pulses case with both multiplicative and additive covariance inflation

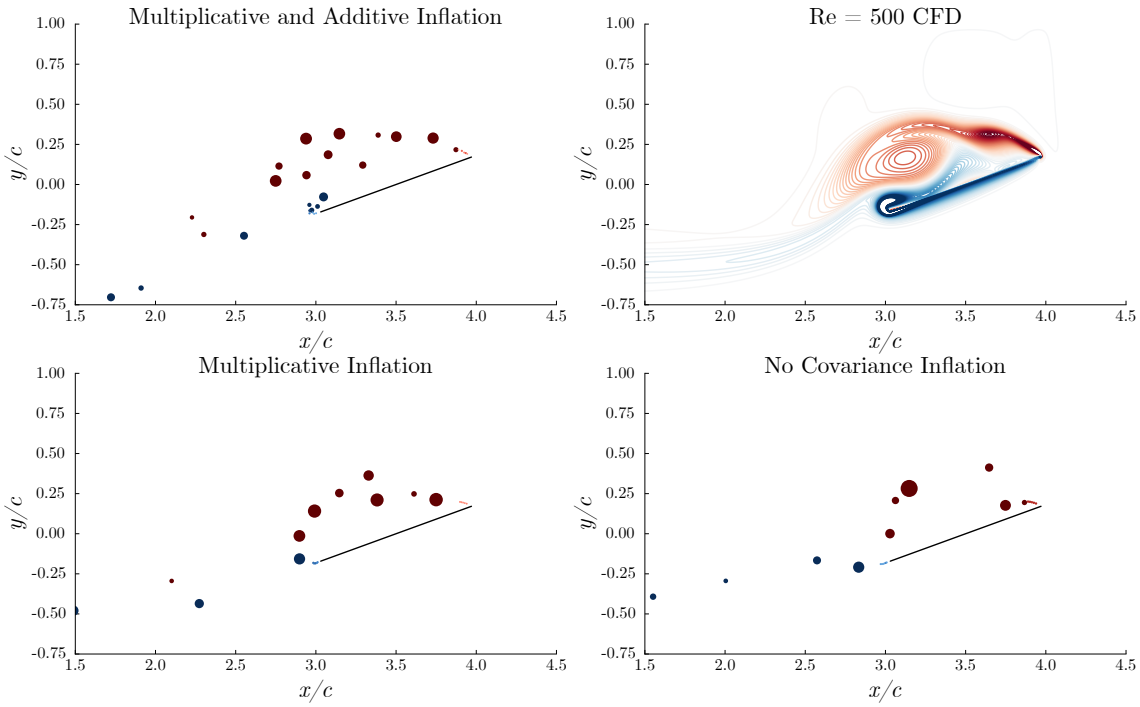

Figure 4.33: Comparison of the vorticity distribution for the two pulses case at 3.5 convective times.

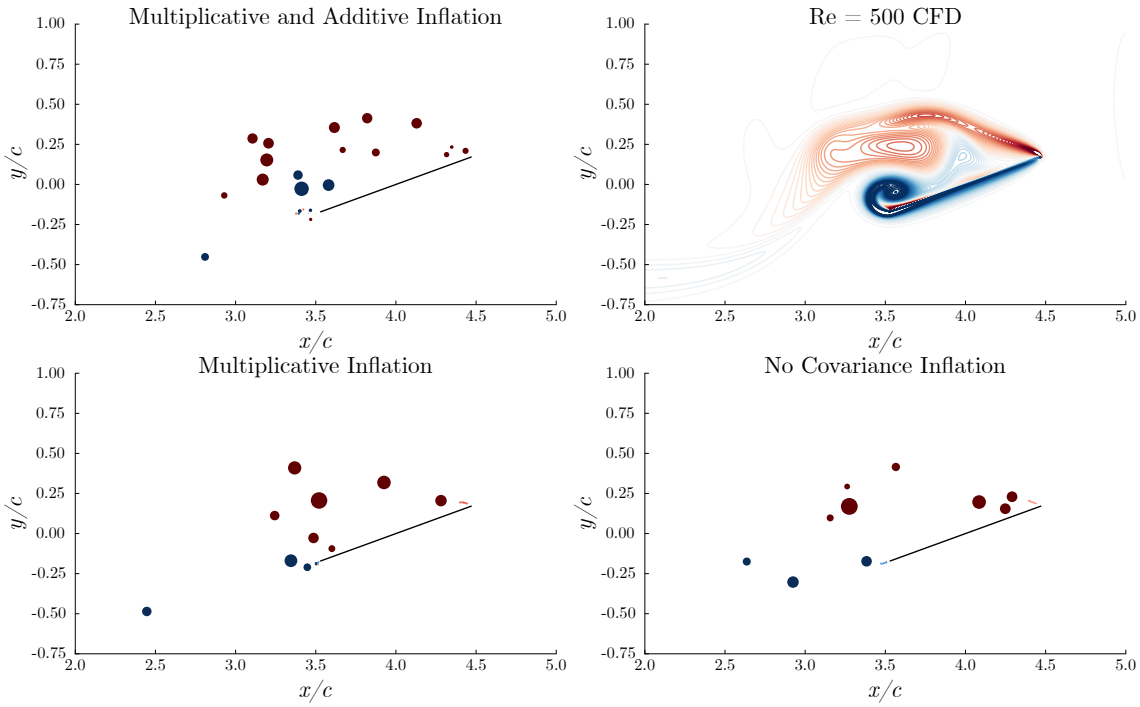

Figure 4.34: Comparison of the vorticity distribution for the two pulses case at 4 convective times.

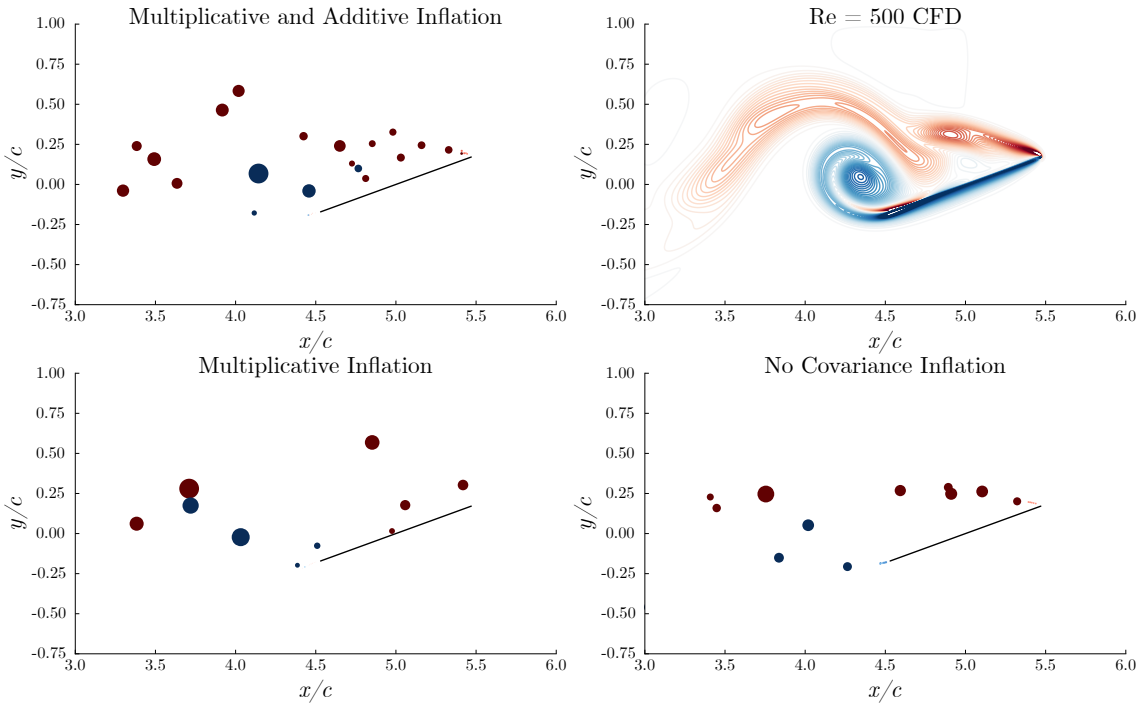

Figure 4.35: Comparison of the vorticity distribution for the two pulses case at 5 convective times.

Chapter 5

Conclusion

Vortex models in aerodynamics typically have to pick between dynamical richness and speed. In this work, we explored two solutions that allows us to achieve both. In Chapter 3, we introduced a hybrid vortex sheet/point vortex model that was able to keep its dimensions small by transferring circulation from the computationally expensive sheets into the point vortices. By using an impulse-matching circulation transfer procedure, we can ensure that the transfer process does not alter the force response of the model too significantly. We demonstrated the model on test cases with impulsive translation and rapid pitch-up motions, and saw that the predicted early time forces agreed reasonably well with results from high-fidelity simulations. Although the predicted bluff-body shedding frequency did not match the CFD results, it is important that the model was even able to run for that many convective times. The ability to control the relative vorticity distribution between the vortex sheets and point vortices makes the hybrid model flexible. As we have noted, the hybrid model can emulate most existing inviscid vortex models with the appropriate choice of error tolerance and minimum vortex release interval. Moreover, the hybrid model presented in this work is only one of the possible applications of the circulation transfer procedure, as the underlying impulse-matching principle is agnostic to the choice of vortex elements.

In Chapter 4, we developed a low-order vortex blob model that used the EnKF to assimilate surface pressure data. We showed that, with the appropriate tuning of the covariance inflation parameters, the vortex blob model was able to predict a vorticity distribution that

closely resembles that from CFD results. Once we tuned the model for a single pressure distribution, that of the pulse-free case, we saw that the same covariance inflation parameters were able to capture the effect of leading edge actuation. This demonstrates the possibility of using real-time data as part of the closure model for a leading edge shedding criterion.

5.1 Future Directions

Using vortex aggregation in conjunction with the EnKF has some unexpected results. We found that increasing the ensemble size improved our results only up to a point. With a larger ensemble, we increase the probability that at least one member of the ensemble will *not* decide to aggregate a vortex blob that the rest of the ensemble decided to aggregate. Since the current procedure requires unanimous consensus on which particles to eliminate, a larger ensemble size reduces the effectiveness of the aggregation process. With more vortex blobs in the system, we also have increased noise. It may be worth investigating an alternative aggregation procedure that does not couple all the ensemble members together. One possible resolution is to try the unscented Kalman filter (UKF) instead of the EnKF. During the initial investigation into data assimilation, we did not have the vortex aggregation procedure in place. That set up an expectation for a very high-dimensional system, which pushed us away from using the UKF. Now that we know the aggregation process can keep the number of our states small, it should be reconsidered as a candidate. Since the UKF resamples from a mean state at every time-step, it should be possible to apply the aggregation to only the mean state.

The UKF might also open up the possibility of applying data assimilation to the hybrid model. Unlike the vortex blob model, where particles are only introduced through vortex shedding, the number vortex particles changes every time we apply filtering along the vortex sheet. Even without filtering, we would still have to apply adaptive point insertion

in order to keep the sheet smooth. That type of variation makes the hybrid model more difficult to use in a persistent ensemble. In the UKF, however, it may be possible to apply filtering only to the mean state.

Another important aspect of the EnKF-based model to consider is the placement of the pressure sensors. The current placement, based on a Chebyshev grid, is simply an artifact of how the flat plate is implemented numerically. One possible direction is to reimplement the EnKF algorithm using *representers*, which measures how each measurement affects the model state [16]. A more comprehensive study of the model's observability properties would be invaluable.

Appendix A

The Infinitely Thin, Flat Plate

In this appendix, we derive some useful properties and tools for working with an infinitely thin plate in an inviscid fluid. Although some of these results are well known (see any introduction to thin-airfoil theory, for example), the notation and some intermediate results introduced in this chapter will be used heavily to derive more interesting aspects of this thesis.

Let the flat plate be characterized by its chord length c, angle of attack α, and centroid $\boldsymbol{x}_c$. Its kinematics can then be completely prescribed by its centroid velocity $\boldsymbol{u}_c$ and its angular velocity $\dot{\alpha}$. We denote the unit vectors tangent and normal to the plate with $\hat{\boldsymbol{\tau}}$ and $\hat{\boldsymbol{n}}$, respectively. $\hat{\boldsymbol{\tau}}$ points from the trailing edge to the leading edge, and $\hat{\boldsymbol{n}}$ points from the lower surface to the upper surface. We then define a transformation from inertial coordinates to plate-centered coordinates

$$l(\boldsymbol{\xi}) = \hat{\boldsymbol{\tau}} \cdot (\boldsymbol{\xi} - \boldsymbol{x}_0)\,, \tag{A.1}$$

its inverse

$$\boldsymbol{x}_p(\lambda) = l^{-1}(\lambda) = \boldsymbol{x}_0 + \lambda\hat{\boldsymbol{\tau}}, \tag{A.2}$$

as well as a normalized variant (plate edges map to ± 1)

$$s(\boldsymbol{\xi}) = \frac{2}{c} l(\boldsymbol{\xi}). \tag{A.3}$$

A.1 Bound Vortex Sheet Strength

In this section, we derive the strength distribution of the bound vortex sheet used to maintain the no-flow-through condition on the flat plate. We start with the equation for the velocity induced by a vortex sheet (from Equation (2.15)):

$$\boldsymbol{u}_{\text{vs}}(\boldsymbol{\xi}) = \frac{1}{2\pi}\int_{\mathcal{C}} \gamma_{\text{vs}}(\lambda)\,\hat{\boldsymbol{k}} \times \frac{\boldsymbol{\xi} - \boldsymbol{x}_{\text{vs}}(\lambda)}{\left|\boldsymbol{\xi} - \boldsymbol{x}_{\text{vs}}(\lambda)\right|^2}\,\mathrm{d}\lambda,$$

where $\mathcal{C}$ is the contour occupied by the sheet, γ_{vs} is the local sheet strength, and $\boldsymbol{x}_{\text{vs}}$ converts arc length coordinates to inertial coordinates. For the bound vortex sheet, the equation above becomes

$$\boldsymbol{u}_{p}(\boldsymbol{\xi}) = \frac{1}{2\pi}\int_{-c/2}^{c/2} \gamma_{p}(\lambda)\,\hat{\boldsymbol{k}} \times \frac{\boldsymbol{\xi} - \boldsymbol{x}_{p}(\lambda)}{\left|\boldsymbol{\xi} - \boldsymbol{x}_{p}(\lambda)\right|^2}\,\mathrm{d}\lambda.$$

When the evaluation point $\boldsymbol{\xi}$ is *on* the plate, we have

$$\boldsymbol{u}_{p}(\boldsymbol{\xi}) = \hat{\boldsymbol{n}}\frac{1}{2\pi}\fint_{-c/2}^{c/2} \frac{\gamma_{p}(\lambda)}{l(\boldsymbol{\xi}) - \lambda}\,\mathrm{d}\lambda \mp \hat{\boldsymbol{\tau}}\frac{(\gamma_p \circ l)\,(\boldsymbol{\xi})}{2}, \tag{A.4}$$

where the integral is a Cauchy principal value integral and the sign in front of the second term depends on the direction that $\boldsymbol{\xi}$ is approached from ($-$ when the approach is against $\hat{\boldsymbol{n}}$ and $+$ when the approach aligns with $\hat{\boldsymbol{n}}$).

Suppose we can partition the ambient vorticity into N_v vortex elements. We denote the circulation contained in the i-th element as Γ_i. Since velocities induced by disjoint regions of vorticity can simply be added together, we express the velocity induced by all ambient vorticity at a point $\boldsymbol{\xi}$ as the sum

$$\sum_{i=1}^{N_v} \boldsymbol{u}_A^i(\boldsymbol{\xi}), \tag{A.5}$$

where $\boldsymbol{u}_A^i$ denotes the velocity field induced by the i-th vortex element. The total velocity

at any point in the fluid is then given by

$$\boldsymbol{u}(\boldsymbol{\xi}) = \boldsymbol{u}_p(\boldsymbol{\xi}) + \sum_{i=1}^{N_v} \boldsymbol{u}_A^i(\boldsymbol{\xi}). \tag{A.6}$$

Now let us denote $\boldsymbol{u}_B(\boldsymbol{\xi})$ as the velocity of the plate at some location $\boldsymbol{\xi}$. In order to enforce the no-flow-through condition, we must have, for any $\boldsymbol{\xi}$ on the plate,

$$\hat{\boldsymbol{n}} \cdot \boldsymbol{u}(\boldsymbol{\xi}) = \hat{\boldsymbol{n}} \cdot \left[\sum_{i=1}^{N_v} \boldsymbol{u}_A^i(\boldsymbol{\xi}) + \boldsymbol{u}_p(\boldsymbol{\xi}) \right] = \hat{\boldsymbol{n}} \cdot \boldsymbol{u}_B(\boldsymbol{\xi}) \tag{A.7}$$

and after substituting in Equation (A.4), we have

$$\frac{1}{2\pi} \fint_{-c/2}^{c/2} \frac{\gamma_p(\lambda)}{l(\boldsymbol{\xi}) - \lambda} \, \mathrm{d}\lambda = \hat{\boldsymbol{n}} \cdot \left[\boldsymbol{u}_B(\boldsymbol{\xi}) - \sum_{i=1}^{N_v} \boldsymbol{u}_A^i(\boldsymbol{\xi}) \right],$$

which forms an integral equation for γ_p. To make this equation easier to solve, we apply a change of variables

$$\frac{1}{2\pi} \fint_{-1}^{1} \frac{\left(\gamma_p \circ \frac{c}{2}\right)(\lambda)}{\sigma - \lambda} \, \mathrm{d}\lambda = \hat{\boldsymbol{n}} \left[\left(\boldsymbol{u}_B \circ s^{-1} \right)(\sigma) - \sum_{i=1}^{N_v} \left(\boldsymbol{u}_A^i \circ s^{-1} \right)(\sigma) \right],$$

which can then be solved using the conservation of total vorticity and the inversion formula found in Muskhelishvili to obtain:

$$\left(\gamma_p \circ \frac{c}{2}\right)(\sigma) = \frac{2}{\pi\sqrt{1-\sigma^2}} \left(\fint_{-1}^{1} \frac{\sqrt{1-\lambda^2}}{\lambda - \sigma} \hat{\boldsymbol{n}} \left[\left(\boldsymbol{u}_B \circ s^{-1} \right)(\sigma) - \sum_{i=1}^{N_v} \left(\boldsymbol{u}_A^i \circ s^{-1} \right)(\sigma) \right] \mathrm{d}\lambda + \frac{\Gamma_A}{c} \right),$$

where

$$\Gamma_A = \sum_{i=1}^{N_v} \Gamma_i \tag{A.8}$$

is the total circulation contained in ambient fluid. If we write $\boldsymbol{u}_B$ in terms of the plate kinematics

$$\hat{\boldsymbol{n}} \cdot (\boldsymbol{u}_B \circ s^{-1})(\sigma) = (\hat{\boldsymbol{n}} \cdot \boldsymbol{u}_c) + \frac{c}{2} \dot{\alpha} \sigma$$

and expand each $\boldsymbol{u}_A^i$ as a Chebyshev series

$$(\boldsymbol{u}_A^i \circ s^{-1})(\sigma) = \sum_{n=0}^{\infty} \left(A_n^i \hat{\boldsymbol{n}} + B_n^i \hat{\boldsymbol{\tau}}\right) T_n(\sigma), \tag{A.9}$$

then the bound vortex sheet strength can be expressed as

$$\gamma_p = \gamma_b + \sum_{i=1}^{N_v} \gamma_i, \tag{A.10}$$

where γ_b corresponds to the bound vortex sheet generated in response to body motion, given by

$$\gamma_B\left(\sigma\frac{c}{2}\right) = \frac{-2\left(\hat{\boldsymbol{n}} \cdot \boldsymbol{u}_c\right)\sigma - \frac{c}{2}\dot{\alpha}}{\sqrt{1-\sigma^2}} + \sqrt{1-\sigma^2}\frac{c}{2}\dot{\alpha} \tag{A.11}$$

and γ_i corresponds to the bound vortex sheet generated in response to the velocity induced by the i-th vortex element

$$\gamma_i\left(\sigma\frac{c}{2}\right) = \frac{2A_0^i\sigma + A_1^i - \frac{2\Gamma_i}{\pi c}}{\sqrt{1-\sigma^2}} - \sqrt{1-\sigma^2}\sum_{n=1}^{\infty} A_n^i U_{n-1}(\sigma). \tag{A.12}$$

The bound vortex sheets given by γ_i serve the same role as image vortices in the circle-plane formulation of a flat plate. For later derivations where interpreting the bound vortex sheets as a single entity is more useful, we define

$$A_n := \sum_{i=1}^{N_v} A_n^i \tag{A.13}$$

and

$$B_n := \sum_{i=1}^{N_v} B_n^i. \tag{A.14}$$

A.2 The Leading Edge Suction Parameter

In general, the velocities at the edges of the infinitely thin plate are infinite. This infinite velocity leads to an infinite negative pressure, which when integrated across the vanishingly thin edge, gives a finite suction force. From Garrick, we know that this force has the form

$$F_e = \pi \rho S^2 \tag{A.15}$$

where

$$S := \frac{1}{\sqrt{2}} \lim_{\sigma \to \pm 1} \gamma \left(\sigma \frac{c}{2} \right) \sqrt{1 - \sigma}, \tag{A.16}$$

with $\sigma = 1$ at the leading edge and $\sigma = -1$ at the trailing edge. Substituting Equations (A.11) and (A.12) into the limit above, we find that

$$S = \pm 2A_0 + A_1 - \frac{2\Gamma_A}{\pi c}. \tag{A.17}$$

Ramesh and Gopalarathnam defined the non-dimensional form of this suction parameter with

$$\text{SP}_\pm := \frac{S}{\sqrt{c}U} = \pm \frac{2A_0 + A_1 - \frac{2\Gamma_A}{\pi c}}{\sqrt{c}U}, \tag{A.18}$$

where U is the freestream velocity. Following the observations that real airfoils can support a critical level of leading edge suction before the flow separates, Ramesh and Gopalarathnam introduced a new vortex shedding criterion where vorticity is only released if the suction parameters exceed a threshold value. In this work, we will enforce the Kutta condition by using a critical trailing edge suction parameter (TESP_c) of zero, and relax the Kutta condition at the leading edge by allowing the critical leading edge suction parameter (LESP_c) to be nonzero.

A.3 Impulse of the Bound Vortex Sheets

The impulse of the bound vortex sheet is defined by the equation

$$\oint \gamma_p(\lambda) \left(\boldsymbol{x}_p(\lambda) \times \hat{\boldsymbol{k}} \right) \mathrm{d}\lambda.$$

If we substitute the bound vortex sheet strength found in Equations (A.10) to (A.12) into the expression above, then in our plate-centered coordinates, we find that the impulse of the bound vortex sheet generated by body motion is

$$\oint \gamma_B(\lambda) \left(\boldsymbol{x}_p \times \hat{\boldsymbol{k}} \right) \mathrm{d}\lambda = -\hat{\boldsymbol{n}}\pi \left(\frac{c}{2} \right)^2 (\hat{\boldsymbol{n}} \cdot \boldsymbol{u}_c) \,, \tag{A.19}$$

and the impulse of the sheet associated with the i-th vortex element is

$$\oint \gamma_i(\lambda) \left(\boldsymbol{x}_p \times \hat{\boldsymbol{k}} \right) \mathrm{d}\lambda = -(\boldsymbol{x}_0 \times \hat{\boldsymbol{k}})\Gamma_i + \hat{\boldsymbol{n}}\pi \left(\frac{c}{2} \right)^2 \left(A_0^i - \frac{A_2^i}{2} \right). \tag{A.20}$$

Suppose the i-th vortex element is a point vortex with circulation Γ_i and located at $\boldsymbol{x}_i$. We can expressed its position in the normalized, plate-centered coordinates as

$$\tilde{x} := \frac{2}{c} (\boldsymbol{x}_i \cdot \hat{\boldsymbol{\tau}})$$

and

$$\tilde{y} := \frac{2}{c} (\boldsymbol{x}_i \cdot \hat{\boldsymbol{n}}) \,.$$

The normal component of the velocity that it induces along the plate can then be expressed

as

$$\begin{aligned}\hat{\boldsymbol{n}} \cdot (\boldsymbol{u}_i \circ s^{-1})(\sigma) &= \hat{\boldsymbol{n}} \cdot \frac{\Gamma_i}{c\pi}\hat{\boldsymbol{k}} \times \frac{(\sigma - \tilde{x})\hat{\boldsymbol{\tau}} - \tilde{y}}{|(\sigma - \tilde{x})\hat{\boldsymbol{\tau}} - \tilde{y}|^2} \\ &= \frac{\Gamma_i}{c\pi}\left[\hat{\boldsymbol{n}}\frac{\sigma - \tilde{x}}{(\sigma - \tilde{x})^2 + \tilde{y}^2} - \hat{\boldsymbol{\tau}}\frac{\tilde{y}}{(\sigma - \tilde{x})^2 + \tilde{y}^2}\right].\end{aligned}$$

Using the orthogonality properties of the Chebyshev polynomials of the first kind, we find that the Chebyshev coefficients in Equation (A.20) are given by

$$A_0^i - \frac{A_2^i}{2} = \frac{2\Gamma_i}{\pi^2 c}\int_{-1}^{1} \frac{\sqrt{1-\sigma^2}}{(\sigma - \tilde{x})^2 + \tilde{y}^2}(\sigma - \tilde{x})\,\mathrm{d}\sigma.$$

If we define $\tilde{z} := \tilde{x} + \mathrm{i}\tilde{y}$, then applying contour integration to the integral above gives us

$$A_0^i - \frac{A_2^i}{2} = \frac{2\Gamma_i}{\pi c}\mathrm{Re}\left\{\tilde{z} - \sqrt{\tilde{z}-1}\sqrt{\tilde{z}+1}\right\}. \tag{A.21}$$

The impulse of the i-th point vortex in the system take the form

$$\begin{aligned}\int_i \boldsymbol{x} \times \boldsymbol{\omega}\,\mathrm{d}A &= \Gamma_i \boldsymbol{x}_i \times \hat{\boldsymbol{k}} \\ &= \Gamma\left[\boldsymbol{x}_0 + \frac{c}{2}\left(\tilde{x}_i\hat{\boldsymbol{n}} - \tilde{y}_i\hat{\boldsymbol{\tau}}\right)\right]\end{aligned} \tag{A.22}$$

Combining Equations (A.22), (A.20), and (A.21), we find that the impulse of a point vortex and its associated bound vortex sheet is given by

$$\boldsymbol{p}_i = \frac{c}{2}\Gamma_i\left[\hat{\boldsymbol{\tau}}\mathrm{Im}\left\{\tilde{z}\right\} - \hat{\boldsymbol{n}}\mathrm{Re}\left\{\sqrt{\tilde{z}-1}\sqrt{\tilde{z}+1}\right\}\right]. \tag{A.23}$$

This is equivalent to the impulse of the vortex and its circle-plane image.

A.4 Pressure Distribution

The pressure difference across a the flat bound vortex sheet is given by

$$[p]^{+}_{-}(\boldsymbol{\xi}) = \rho\left(\gamma_p \circ l\right)(\boldsymbol{\xi})\left[\frac{1}{2}\left(\boldsymbol{u}^{+}(\boldsymbol{\xi}) + \boldsymbol{u}^{-}(\boldsymbol{\xi})\right) - \boldsymbol{u}_c\right]\cdot\hat{\boldsymbol{\tau}} + \rho\frac{\mathrm{d}\Gamma}{\mathrm{d}t}, \tag{A.24}$$

where the superscripts on $\boldsymbol{u}$ denote the direction that $\boldsymbol{\xi}$ is approached from ($+$ when the approaching against $\hat{\boldsymbol{n}}$, and $-$ when approaching along $\hat{\boldsymbol{n}}$). We can find γ_p through Equations (A.10) to (A.12), and $\boldsymbol{u}_c$ is prescribed, so we only need the surface velocities and the rate of change of circulation.

Starting with the surface velocities, we have from Equations (A.4) and (A.9) that

$$\boldsymbol{u}^{\pm}(\boldsymbol{\xi}) = \sum_{n=0}^{\infty}\left(A_n\hat{\boldsymbol{n}} + B_n\hat{\boldsymbol{\tau}}\right)\left(T_n \circ s\right)(\boldsymbol{\xi}) + \hat{\boldsymbol{n}}\frac{1}{2\pi}\fint_{-c/2}^{c/2}\frac{\gamma_p(\lambda)}{l(\boldsymbol{\xi}) - \lambda}\,\mathrm{d}\lambda \mp \hat{\boldsymbol{\tau}}\frac{\left(\gamma_p \circ l\right)(\boldsymbol{\xi})}{2}.$$

This gives us

$$\frac{1}{2}\left[\boldsymbol{u}^{+}(\boldsymbol{\xi}) + \boldsymbol{u}^{-}(\boldsymbol{\xi})\right]\cdot\hat{\boldsymbol{\tau}} = \sum_{i=1}^{\infty} B_n\left(T_n \circ s\right)(\boldsymbol{\xi}). \tag{A.25}$$

The circulation contained between the trailing edge of the plate to some arc length coordinate σ is defined as

$$\Gamma(\sigma) = \int_{-c/2}^{l}\gamma_p(\lambda)\,\mathrm{d}\lambda. \tag{A.26}$$

Substituting in the expression for γ_p and integrating, we find

$$\begin{aligned}\left(\Gamma \circ \frac{c}{2}\right)(\sigma) = \Gamma_A\left(\frac{\cos^{-1}\sigma}{\pi} - 1\right) - \frac{c\sqrt{1-\sigma^2}}{2}\Bigg[2\left(A_0 - \hat{\boldsymbol{n}}\cdot\boldsymbol{u}_c\right) + \left(A_1 - \frac{\dot{\alpha}c}{2}\right)\sigma \\ + \sum_{n=2}^{\infty} A_n\left(\frac{U_n(\sigma)}{n+1} - \frac{U_{n-2}(\sigma)}{n-1}\right)\Bigg].\end{aligned} \tag{A.27}$$

Then taking the time derivative of expression above, we obtain

$$\left(\frac{\mathrm{d}\Gamma}{\mathrm{d}t}\circ\frac{c}{2}\right)(\sigma)=\frac{\mathrm{d}\Gamma_A}{\mathrm{d}t}\left(\frac{\cos^{-1}\sigma}{\pi}-1\right)-\frac{c\sqrt{1-\sigma^2}}{2}\left[2\left(\frac{\mathrm{d}A_0}{\mathrm{d}t}+\dot{\alpha}\hat{\boldsymbol{\tau}}\cdot\frac{\mathrm{d}\boldsymbol{u}_c}{\mathrm{d}t}\right)+\left(\frac{\mathrm{d}A_1}{\mathrm{d}t}-\frac{\ddot{\alpha}c}{2}\right)\sigma+\sum_{n=2}^{\infty}\frac{\mathrm{d}A_n}{\mathrm{d}t}\left(\frac{U_n(\sigma)}{n+1}-\frac{U_{n-2}(\sigma)}{n-1}\right)\right]. \tag{A.28}$$

We can find the time derivative of the Chebyshev coefficients by first noting that the the acceleration induced on the plate's surface by ambient vorticity can be expanded into the following Chebyshev series

$$\frac{\mathrm{d}\boldsymbol{u}_A}{\mathrm{d}t}\circ s^{-1}(\sigma)=\sum_{n=0}^{\infty}\left[\left(\frac{\mathrm{d}A_n}{\mathrm{d}t}+\dot{\alpha}B_n\right)\hat{\boldsymbol{n}}-\left(\dot{\alpha}A_n-\frac{\mathrm{d}B_n}{\mathrm{d}t}\right)\hat{\boldsymbol{\tau}}\right]T_n(\sigma). \tag{A.29}$$

Then, we can determine the pressure difference by substituting Equations (A.9), (A.25), (A.28) and (A.29) into Equation (A.24).

Appendix B

Impulse-Matching Velocity Correction

In this appendix, we will derive the velocity correction on a target point vortex that eliminates spurious force that it produces as it siphons circulation from a source point vortex. To streamline the derivation, we will use the complex form of Equation (A.23), which gives the impulse of a point vortex and its associated bound vortex sheet (or its image vortex in the circle plane)

$$p(\tilde{z}, \Gamma) = \mathrm{e}^{\mathrm{i}\alpha} \frac{c}{2} \Gamma \hat{p}(\tilde{z}) \tag{B.1}$$

where we have defined the unit total impulse as

$$\hat{p}(\tilde{z}) := \mathrm{Im}\left\{\tilde{z}\right\} - \mathrm{iRe}\left\{\sqrt{\tilde{z}-1}\sqrt{\tilde{z}+1}\right\}. \tag{B.2}$$

The time derivative of impulse is then given by

$$\frac{\mathrm{d}p}{\mathrm{d}t}(\tilde{z}, \Gamma) = \mathrm{i}\dot{\alpha} + \mathrm{e}^{\mathrm{i}\alpha} \frac{c}{2} \left(\dot{\Gamma} \hat{p}(\tilde{z}, \Gamma) + \Gamma \frac{\mathrm{d}\hat{p}}{\mathrm{d}t}(\tilde{z}) \right) \tag{B.3}$$

where

$$\frac{\mathrm{d}\hat{p}}{\mathrm{d}t}(\tilde{z}, \Gamma) = -\mathrm{i}\left[\dot{\tilde{z}} + \mathrm{Re}\left\{ \left(\frac{\tilde{z}}{\sqrt{\tilde{z}-1}\sqrt{\tilde{z}+1}} - 1 \right) \right\} \dot{\tilde{z}} \right]. \tag{B.4}$$

As before, we will use the subscripts s and t to refer to the point vortices we are transferring circulation from and to, respectively. The rate of change of impulse due to these two point

vortices, including the effect of circulation transfer, is

$$\frac{\mathrm{d}p_s}{\mathrm{d}t} + \frac{\mathrm{d}p_t}{\mathrm{d}t} = \mathrm{i}\dot{\alpha}(p_s + p_t) + \mathrm{e}^{\mathrm{i}\alpha}\frac{c}{2}\left[\dot{\Gamma}(\hat{p}_t - \hat{p}_s) + \Gamma_s\frac{\mathrm{d}\hat{p}_s}{\mathrm{d}t} + \Gamma_t\left(\frac{\mathrm{d}\hat{p}_t}{\mathrm{d}t} + \frac{\mathrm{d}\Delta\hat{p}_t}{\mathrm{d}t}\right)\right], \tag{B.5}$$

where $\mathrm{d}\Delta\hat{p}_t/\,\mathrm{d}t$ comes from applying a velocity correction to the target point vortex. For the velocity correction to cancel out the effect of moving circulation, we must have

$$\frac{\mathrm{d}\Delta p_t}{\mathrm{d}t} = \frac{\dot{\Gamma}}{\Gamma_t}(\hat{p}_s - \hat{p}_t). \tag{B.6}$$

If we define

$$\beta := \frac{\tilde{z}_t}{\sqrt{\tilde{z}_t - 1}\sqrt{\tilde{z}_t + 1}}, \tag{B.7}$$

then we can combine Equations (B.4) and (B.6) to get

$$\Delta\dot{\tilde{z}}_t(\beta + 1) + \Delta\dot{\tilde{z}}_t^\star(\beta^\star - 1) = 2\mathrm{i}\frac{\dot{\Gamma}}{\Gamma_t}(\hat{p}_s - \hat{p}_t). \tag{B.8}$$

We can substitute the equation above into its conjugate

$$\Delta\dot{\tilde{z}}_t^\star(\beta^\star + 1) + \Delta\dot{\tilde{z}}_t(\beta - 1) = -2\mathrm{i}\frac{\dot{\Gamma}}{\Gamma_t}(\hat{p}_s^\star - \hat{p}_t^\star) \tag{B.9}$$

to obtain the velocity correction to the target point vortex

$$\Delta\dot{z}_t = \frac{\mathrm{e}^{\mathrm{i}\alpha}c}{2}\Delta\dot{\tilde{z}}_t = \frac{\mathrm{i}\mathrm{e}^{\mathrm{i}\alpha}c}{2}\frac{\dot{\Gamma}}{\Gamma_t}\left(\frac{(\hat{p}_s - \hat{p}_t)(\beta^\star + 1) - (\hat{p}_s^\star - \hat{p}_t^\star)(\beta^\star - 1)}{\beta + \beta^\star}\right) \tag{B.10}$$

Bibliography

[1] Sunil Ahuja and Clarence W. Rowley. "Feedback control of unstable steady states of flow past a flat plate using reduced-order estimators". In: *Journal of Fluid Mechanics* 645 (2010), pp. 447–478. DOI: 10.1017/S0022112009992655. arXiv: 0902.1207.

[2] Silas Alben and Michael J Shelley. "Flapping states of a flag in an inviscid fluid: bistability and the transition to chaos". In: *Physical review letters* 100.7 (2008), p. 074301.

[3] Michael Amitay and Ari Glezer. "Flow transients induced on a 2D airfoil by pulse-modulated actuation". In: *Experiments in Fluids* 40.2 (2006), pp. 329–331.

[4] Jeffrey L. Anderson and Stephen L. Anderson. "A Monte Carlo Implementation of the Nonlinear Filtering Problem to Produce Ensemble Assimilations and Forecasts". In: *Monthly Weather Review* 127.12 (1999), pp. 2741–2758. DOI: 10.1175/1520-0493(1999)127<2741:AMCIOT>2.0.CO;2.

[5] Salman A. Ansari, Rafal Zbikowski, and Kevin Knowles. "Non-linear unsteady aerodynamic model for insect-like flapping wings in the hover. Part 2: implementation and validation". In: *Proc. Inst. Mech. Eng. Part G J. Aerosp. Eng.* 220 (2006), pp. 169–186. DOI: 10.1243/09544100JAERO50.

[6] Nadine Aubry et al. "The dynamics of coherent structures in the wall region of a turbulent boundary layer". In: *Journal of Fluid Mechanics* 192.-1 (1988), p. 115. DOI: 10.1017/S0022112088001818.

[7] C. E. Brown and W. H. Michael. "Effect of Leading-Edge Separation on the Lift of a Delta Wing". In: *J. Aeronaut. Sci.* 21.10 (1954), pp. 690–694. DOI: 10.2514/8.3180.

[8] Gerrit Burgers, Peter Jan van Leeuwen, and Geir Evensen. "Analysis Scheme in the Ensemble Kalman Filter". In: *Monthly Weather Review* 126.6 (1998), pp. 1719–1724. DOI: 10.1175/1520-0493(1998)126<1719:ASITEK>2.0.CO;2.

[9] Alexandre Joel Chorin. "Hairpin removal in vortex interactions". In: *J. Comput. Phys.* 91.1 (1990), pp. 1–21. DOI: 10.1016/0021-9991(90)90001-H.

[10] Luca Cortelezzi. "A Theoretical and Computational Study on Active Wake Control". PhD thesis. California Institute of Technology, 1993.

[11] Georges-Henri Cottet and Petros D. Koumoutsakos. *Vortex Methods: Theory and Practice*. Cambridge university press, 2000.

[12] Michael H. Dickinson and Karl Götz. "Unsteady aerodynamic performance of model wings at low reynolds numbers". In: *J. Exp. Biol.* 174 (1993), pp. 45–64. DOI: 10.1242/jeb.00739.

[13] Cristina I. Draghicescu and Mircea Draghicescu. "A Fast Algorithm for Vortex Blob Interactions". In: *J. Comput. Phys.* 116.1 (1995), pp. 69–78. DOI: 10.1006/jcph.1995.1006.

[14] Jeff D. Eldredge. "A Reconciliation of Viscous and Inviscid Approaches to Computing Locomotion of Deforming Bodies". In: *Exp. Mech.* 50.9 (July 2009), pp. 1349–1353. DOI: 10.1007/s11340-009-9275-0.

[15] C.P. Ellington. "The aerodynamics of hovering insect flight. IV. Aeorodynamic mechanisms". In: *Philosophical Transactions of the Royal Society of London B: Biological Sciences* (1984), pp. 79–113.

[16] Geir Evensen. *Data assimilation: the ensemble Kalman filter*. Springer Science & Business Media, 2009.

[17] Geir Evensen. "Sequential data assimilation with a nonlinear quasi-geostrophic model using Monte Carlo methods to forecast error statistics". In: 99.C5 (1994), p. 10143. DOI: 10.1029/94JC00572.

[18] I. E. Garrick. *Propulsion of a flapping and oscillating airfoil*. Tech. rep. 1936.

[19] Isadore Edward Garrick. "On some reciprocal relations in the theory of nonstationary flows". In: (1938).

[20] Leslie Greengard and V Rokhlin. "A fast algorithm for particle simulations". In: *J. Comput. Phys.* 73.2 (1987), pp. 325–348. DOI: 10.1016/0021-9991(87)90140-9.

[21] Ole H. Hald and Vincenza Mauceri Del Prete. "Convergence of Vortex Methods for Euler's Equations". In: *Math. Comput.* 32.143 (1978), pp. 791–809.

[22] Maziar S. Hemati, Jeff D. Eldredge, and Jason L. Speyer. "Improving vortex models via optimal control theory". In: *J. Fluids Struct.* 49 (2014), pp. 91–111. DOI: 10.1016/j.jfluidstructs.2014.04.004.

[23] P. L. Houtekamer et al. "A Sequential Ensemble Kalman Filter for Atmospheric Data Assimilation". In: *Monthly Weather Review* 129.1 (2001), pp. 123–137. DOI: 10.1175/1520-0493(2001)129<0123:ASEKFF>2.0.CO;2.

[24] M. Ilak et al. "Model Reduction of the Nonlinear Complex GinzburgLandau Equation". In: *SIAM Journal on Applied Dynamical Systems* 9.4 (2010), pp. 1284–1302. DOI: 10.1137/100787350.

[25] M. Jensen. "Biology and Physics of Locust Flight. III. The Aerodynamics of Locust Flight". In: *Philosophical Transactions of the Royal Society B: Biological Sciences* 239.667 (1956), pp. 511–552. DOI: 10.1098/rstb.1956.0009.

[26] Marvin A. Jones. "The separated flow of an inviscid fluid around a moving flat plate". In: *J. Fluid Mech.* 496 (Dec. 2003), pp. 405–441. DOI: 10.1017/S0022112003006645.

[27] Theodor von Kármán and William R. Sears. "Airfoil Theory for Non-Uniform Motion". In: *J. Aeronaut. Sci.* 5.10 (1938), pp. 379–390. DOI: 10.2514/8.674.

[28] Joseph Katz. "A discrete vortex method for the non-steady separated flow over an airfoil". In: *J. Fluid Mech.* 102 (1981), pp. 315–328. DOI: 10.1017/S0022112081002668.

[29] Wesley Kerstens et al. “Closed-Loop Control of Lift for Longitudinal Gust Suppression at Low Reynolds Numbers”. In: *AIAA J.* 49.8 (2011), pp. 1721–1728. DOI: 10.2514/1.J050954.

[30] Robert Krasny. “A study of singularity formation in a vortex sheet by the point-vortex approximation”. In: *J. Fluid Mech.* 167 (1986), p. 65. DOI: 10.1017/S0022112086002732.

[31] Robert Krasny. “Computation of vortex sheet roll-up in the Trefftz plane”. In: *J. Fluid Mech.* 184 (1987), pp. 123–155. DOI: 10.1017/S0022112087002830.

[32] D. Küchemann. “Report on the I.U.T.A.M. symposium on concentrated vortex motions in fluids”. In: *Journal of Fluid Mechanics* 21.01 (1965), p. 1. DOI: 10.1017/S0022112065000010.

[33] L. Kuznetsov, K. Ide, and C. K. R. T. Jones. “A Method for Assimilation of Lagrangian Data”. In: *Monthly Weather Review* 131.10 (2003), pp. 2247–2260. DOI: 10.1175/1520-0493(2003)131<2247:AMFAOL>2.0.CO;2.

[34] Peter Jan van Leeuwen. “Comment on Data Assimilation Using an Ensemble Kalman Filter Technique”. In: *Monthly Weather Review* 127.6 (2010), pp. 1374–1377. DOI: 10.1175/1520-0493(1999)127<1374:CODAUA>2.0.CO;2.

[35] A Leonard. “Vortex methods for flow simulation”. In: *Journal of Computational Physics* 37.3 (1980), pp. 289–335.

[36] Michael James Lighthill. “Introduction: Boundary layer theory”. In: *Laminar Bound. layers*. Ed. by Louis Rosenhead. Oxford University Press, 1963, pp. 46–113.

[37] John Leask Lumley. “The structure of inhomogeneous turbulent flows”. In: *Atmospheric turbulence and radio wave propagation* (1967).

[38] Zhanhua Ma, Sunil Ahuja, and Clarence W Rowley. “Reduced-order models for control of fluids using the eigensystem realization algorithm”. In: *Theoretical and Computational Fluid Dynamics* 25.1 (2011), pp. 233–247.

[39] Andrew J Majda and Andrea L Bertozzi. *Vorticity and incompressible flow*. Vol. 27. Cambridge University Press, 2002.

[40] Peter S. Maybeck. *Stochastic Models: Estimating, and Control*. Vol. 1. New York: Academic Press, 1979.

[41] Sébastien Michelin and Stefan G. Llewellyn Smith. "An unsteady point vortex method for coupled fluidsolid problems". In: *Theor. Comput. Fluid Dyn.* 2.127–153 (May 2009), p. 23. DOI: 10.1007/s00162-009-0096-7.

[42] D.W. Moore. "The spontaneous appearance of a singularity in the shape of an evolving vortex sheet". In: *Proceedings of the Royal Society of London A: Mathematical, Physical and Engineering Sciences* 365.1720 (1979), pp. 105–119. DOI: 10.1098/rspa.1979.0009. eprint: http://rspa.royalsocietypublishing.org/content/365/1720/105.full.pdf. URL: http://rspa.royalsocietypublishing.org/content/365/1720/105.

[43] N.I. Muskhelishvili. *Singular Integral Equations, Boundary Problems of Function Theory and Their Application to Mathematical Physics*. Corrected reprint of the Noordhoff translation (1953) of the Russian original of 1946. Dover Publications, 2013. ISBN: 9780486145068.

[44] Monika Nitsche, Mark a Taylor, and Robert Krasny. "Comparison of regularizations of vortex sheet motion". In: *Comput. Fluid Solid Mech.* (2003), pp. 1–4.

[45] C. W. Pitt Ford and H Babinsky. "Lift and the leading-edge vortex". In: *J. Fluid Mech.* 720 (2013), pp. 280–313. DOI: 10.1017/jfm.2013.28.

[46] D. I. Pullin. "The large-scale structure of unsteady self-similar rolled-up vortex sheets". In: *Journal of Fluid Mechanics* 88.03 (1978), p. 401. DOI: 10.1017/S0022112078002189.

[47] Kiran Ramesh and Ashok Gopalarathnam. "Theoretical Modeling of Leading Edge Vortices Using the Leading Edge Suction Parameter". In: *AIAA Appl. Aerodyn. Conf.* (June 2012), pp. 1–16. DOI: 10.2514/6.2012-3027.

[48] Louis F. Rossi. "Merging computational elements in vortex simulations". In: *SIAM J. Sci. Comput.* 18.4 (1997), pp. 1014–1027. DOI: 10.1137/S1064827595285287.

[49] C. W. Rowley. "Model Reduction For Fluids, Using Balanced Proper Orthogonal Decomposition". In: *International Journal of Bifurcation and Chaos* 15.03 (2005), pp. 997–1013. DOI: 10.1142/S0218127405012429. eprint: http://www.worldscientific.com/doi/pdf/10.1142/S0218127405012429. URL: http://www.worldscientific.com/doi/abs/10.1142/S0218127405012429.

[50] Turgut Sarpkaya. "An inviscid model of two-dimensional vortex shedding for transient and asymptotically steady separated flow over an inclined plate". In: *J. Fluid Mech.* 68 (1975), p. 109. DOI: 10.1017/S0022112075000717.

[51] Ratnesh K. Shukla and Jeff D. Eldredge. "An inviscid model for vortex shedding from a deforming body". In: *Theoretical and Computational Fluid Dynamics* 21.5 (July 2007), pp. 343–368. DOI: 10.1007/s00162-007-0053-2.

[52] Jason L Speyer and Walter H Chung. *Stochastic processes, estimation, and control*. SIAM, 2008.

[53] Kunihiko Taira and Tim Colonius. "The immersed boundary method: A projection approach". In: *Journal of Computational Physics* 225.2 (Aug. 2007), pp. 2118–2137. DOI: 10.1016/j.jcp.2007.03.005.

[54] Kunihiko Taira et al. "Modal analysis of fluid flows: An overview". In: *arXiv preprint arXiv:1702.01453* (2017).

[55] Kunihiko Taira et al. "Unsteadiness in Flow over a Flat Plate at Angle-of-Attack at Low Reynolds Numbers". In: *45th AIAA Aerosp. Sci. Meet. Exhib.* (2007), pp. 1–16. DOI: 10.2514/6.2007-710.

[56] Andrew Tchieu and Anthony Leonard. "A discrete-vortex model for the arbitrary motion of a thin airfoil with fluidic control". In: *J. Fluids Struct.* 27.5-6 (July 2011), pp. 680–693. DOI: 10.1016/j.jfluidstructs.2011.02.008.

[57] Theodore Theodorsen. *General Theory of Aerodynamic Instability and the Mechanism of Flutter*. Tech. rep. NACA, Dec. 1979.

[58] Herbert Wagner. "Über die Entstehung des dynamischen Auftriebes von Tragflügeln". In: *ZAMM-Journal Appl. Math. Mech. für Angew. Math. und Mech.* 5.1 (1925), pp. 17–35. DOI: 10.1002/zamm.19250050103.

[59] Chengjie Wang and Jeff D. Eldredge. "Low-order phenomenological modeling of leading-edge vortex formation". In: *Theor. Comput. Fluid Dyn.* (Aug. 2012). DOI: 10.1007/s00162-012-0279-5.

[60] Torkel Weis-Fogh. "Quick Estimates of Flight Fitness in Hovering Animals, Including Novel Mechanisms for Lift Production". In: *J. Exp. Biol.* 59.1 (1973), pp. 169–230.

[61] Jeffrey S. Whitaker and Thomas M. Hamill. "Evaluating Methods to Account for System Errors in Ensemble Data Assimilation". In: *Monthly Weather Review* 140.9 (2012), pp. 3078–3089. DOI: 10.1175/MWR-D-11-00276.1.

[62] David R. Williams et al. "Lift Response of a Stalled Wing to Pulsatile Disturbances". In: *AIAA J.* 47.12 (2009), pp. 3031–3037. DOI: 10.2514/1.45407.

[63] James C Wu. "Theory for Aerodynamic Force and Moment in Viscous Flows". In: *AIAA J.* 19.4 (1981), pp. 432–441. DOI: 10.2514/3.50966.

[64] X. Xia and K. Mohseni. "Lift evaluation of a two-dimensional pitching flat plate". In: *Physics of Fluids* 25.9 (2013). DOI: 10.1063/1.4819878.